Fermilab FERMILAB-THESIS-2002-24

Lifetime Measurement of the Charmed Strange Baryon Ξ_c^+

by

Juan E. Ramírez

B.S., Pontificia Universidad Católica del Perú, 1994

M.S., University of Puerto Rico, 1997

A thesis submitted to the

Faculty of the Graduate School of the

University of Colorado

in partial fulfillment of the requirements for the degree

Doctor of Philosophy

Department of Physics

2002

This thesis entitled:

Lifetime Measurement of the Charmed Strange Baryon Ξ_c^+

written by Juan E. Ramírez

has been approved for the Department of Physics

John P. Cumalat

Patricia Rankin

Date

The final copy of this thesis has been examined by the signatories, and we find that both the content and the form meet acceptable presentation standards of scholarly work in the above mentioned discipline.

Ramírez, Juan Eduardo (Ph.D., Physics)

Lifetime Measurement of the Charmed Strange Baryon Ξ_c^+

Thesis directed by Professor John P. Cumalat

A precise determination of the lifetime of the charm-strange baryon Ξ_c^+ is presented. The data for this analysis were collected by FOCUS, Fermilab Experiment E831. FOCUS is a high statistics charm photoproduction experiment which accumulated data during the 1996–1997 Fermilab Fixed Target run. The Ξ_c^+ lifetime result is obtained using 300 $\Xi_c^+ \to \Xi^-\pi^+\pi^+$ decays, 130 $\Xi_c^+ \to \Sigma^+ K^-\pi^+$ decays, 45 $\Xi_c^+ \to pK^-\pi^+$ decays, and 58 $\Xi_c^+ \to \Lambda^0 K^-\pi^+\pi^+$ decays. The lifetime is measured to be $0.439 \pm 0.022 \pm 0.011$ ps. The result is a significant improvement on the current world average.

We also report a measurement of the Ξ_c^0 lifetime using 79 $\Xi_c^0 \to \Xi^-\pi^+$ decays. We obtain a preliminary measurement of the Ξ_c^0 lifetime to be 0.118 ± 0.014 ps. This measurement is in agreement with previous measurements. Systematic uncertainties will be reported after adding more decay modes.

For God

Acknowledgments

Been part of the FOCUS collaboration was a unique experience for me. To meet a group of people working together to run an impressive apparatus is a unforgettable sensation. This experiment was my first encounter with real science, where the quest of knowledge is through the direct observation as oppose to textbooks studies. For this my deepest acknowledgment and gratitude is to each person who helped this experiment to be a reality and contributed to make FOCUS a successful experiment.

I am grateful to Harry Cheung, Doris Kim, Alberto Reis, Daniele Pedrini, Gianluigi Boca, Kevin Stenson, and Eric Vaandering for their comments and suggestions during the review of my analysis, which turn into a paper submitted for publication. Special thanks goes for Brian O'Reilly, who help me through his careful reading, and listening to improve the draft making the reading easy to follow.

Thanks to Eric Vaandering for writing all the settings and templates for the thesis and the defense. This save me a lot of time. Also I would like to thank John Cumalat, Brian O'Reilly, Lorenzo Agostino and Ilaria Segoni for their support and friendship during the preparation of my defense.

Thanks to my parents Juan and Elisa and my three brothers David, Javier, and Ricardo for support me since the beginning of my studies, even if it did not make sense for them why study a career without a "future". They did big sacrifice in support me to finish my college. Thanks to my wife Liz and my daughter Jennifer for their company, support and love during those years as a CU student.

To meet my advisor John Cumalat was a gift that I did not expected receive. Find a talented person is difficult, but find him and be his apprentice is equivalent to win the big prize of a lottery. Not only as a physicist but as a human being he is a great person. With many interesting ideas coming out from his mind would be impossible to try all of them, so he also give me the freedom to choose and learn to discriminate and develop and intuitive way of think.

Contents

List of Tables

List of Figures

Chapter 1

Introduction

The lifetime measurement of the charm-strange baryon Ξ_c^+ is presented in this thesis. We measure the lifetime using the decay channels $\Xi_c^+ \to \Xi^-\pi^+\pi^+$, $\Xi_c^+ \to \Sigma^+K^-\pi^+$, $\Xi_c^+ \to pK^-\pi^+$, and $\Xi_c^+ \to \Lambda^0K^-\pi^+\pi^+$.

The analysis performed in this thesis is based on data obtained from the experiment E831/FOCUS,[1] a high energy photoproduction experiment. The data was collected at the Wideband Hall of Fermi National Laboratory (Fermilab) between August 1996-August 1997. FOCUS is an upgraded version of Fermilab experiment E687 which recorded interactions of high energy photons (with a mean energy of 180 GeV) in a segmented Be0 target to produce charmed particles. More that a million charmed particles have been reconstructed using the decays $D^0 \to K^-\pi^+$, $D^+ \to K^-\pi^+\pi^+$, $D^0 \to K^-\pi^+\pi^+\pi^-$.

This chapter is an overview of the Standard Model of elementary particle physics. In Chapter 2 the Fermilab Tevatron accelerator complex and the production of high energy photons for use by the FOCUS experiment is described. Chapter 3 describes the FOCUS experimental apparatus in detail. The individual detector elements are covered, with special emphasis on those most important to the analyses presented in this thesis. Chapter 4 presents a summary of the reconstruction algorithms used by the experiment and describes the processing of the data used in this analysis, starting from the raw data. In Chapter 5 the methods used for selecting Ξ_c^+ candidates are presented. All the cuts used in the analysis are described. Chapter 6 describes the details of the Ξ_c^+ measurement and the technique employed to obtain the measurement. Finally, Chapter 7 summarizes physics results and compares them with measurements from other experiments and with theoretical expectations.

[1] Photoproduction Of Charm with an Upgraded Spectrometer

1.1 The Standard Model

The "Standard Model" of particle physics is the description and organization of fundamental particles and their interactions. This model reflects our understanding of the universe based on experimental results. As a consequence the Standard Model requires a large number of input parameters, and does not unify all the observed forces. Thus, we believe it must be incomplete.

The Standard Model separates all of the known elementary particles into two classes: fermions (matter particles) and gauge bosons (force carrying particles). The fermions are further divided into two categories, quarks and leptons. At the present there is no experimental evidence that either quarks or leptons are built of still smaller particles.

1.1.1 Quarks

Quarks were initially proposed as a mathematical concept in 1964 by Gell-Mann [1] and Zweig [2], to explain what was quickly becoming a "particle zoo." By combining the quarks in various ways, one could form all the "hadrons" known at the time.

Today, it is well known that everyday matter is made by atoms which contain particles called protons, neutrons, and electrons. Protons and neutrons belong to a class of particles known as "hadrons," which are not fundamental particles, but are comprised of quarks. Hadrons are further sub-divided into "baryons" and "mesons." Particles such as protons and neutrons are "baryons" and are composed of three quarks; "mesons" are made of a quark-antiquark pair, like pions (π) and kaons (K). Also baryons obey Fermi statistics because they have half integer spin and mesons obey Bose statistics because they have integer spin.

To explain this quark grouping, quantum chromodynamics postulates the existence of a new charge-like quantum number called *color*. Each quark carries one of the three colors (red, blue, or green) while each anti-quark carries one of the three anti-colors. Hadrons are bound together by gluons which mediate the strong force. Composite states are required to be "color neutral;" baryons must have one quark of each color while mesons must have two anti-colored quarks.

At present, we know that quarks are real objects. They exist in six flavors (type of quarks) called $up(u)$, $down(d)$, $strange(s)$, $charm(c)$, $bottom(b)$, and $top(t)$. The properties of the quarks are summarized in Table 1.1. The quarks are grouped into three families or generations, each family is a doublet of two quarks with fractional charge (in units of electron charge), $+\frac{2}{3}$ and $-\frac{1}{3}$.

Table 1.1: Properties of the quarks [4].

Quark	Mass (MeV/c^2)	Charge (e)	Generation
d	3–9	$-\frac{1}{3}$	First
u	1.5–5	$+\frac{2}{3}$	
s	60–170	$-\frac{1}{3}$	Second
c	1100–1400	$+\frac{2}{3}$	
b	4100–4400	$-\frac{1}{3}$	Third
t	$173.8 \pm 5.2 \times 10^3$	$+\frac{2}{3}$	

1.1.2 Leptons

The leptons are also organized in three generations or families. Each lepton family contains a charged massive lepton and a neutral, nearly massless[2] neutrino. The charged leptons are named electron (e), muon (μ), and tau (τ); each with its correspondent neutrino.

Table 1.2: Properties of the three families of leptons [4].

Lepton	Mass	Generation
e	0.5110 MeV/c^2	First
ν_e	$<$ 15 eV/c^2	
μ	105.66 MeV/c^2	Second
ν_μ	$<$ 0.17 MeV/c^2	
τ	1777.1 MeV/c^2	Third
ν_τ	$<$ 18.2 MeV/c^2	

The generations of quarks and leptons can be combined to represent the generations of matter, each matter generation is composed by two doublets; the quarks and leptons doublets as shown below.

$$\begin{pmatrix} u \\ d \end{pmatrix} \quad \begin{pmatrix} c \\ s \end{pmatrix} \quad \begin{pmatrix} t \\ b \end{pmatrix}$$
$$\begin{pmatrix} \nu_e \\ e \end{pmatrix} \quad \begin{pmatrix} \nu_\mu \\ \mu \end{pmatrix} \quad \begin{pmatrix} \nu_\tau \\ \tau \end{pmatrix} \tag{1.1}$$

where the particles in each row differ only in mass.

[2]Recent results [5] suggest that neutrinos, in a method similar to that described below for quarks, change flavor. This suggests that some neutrinos may have masses, however small.

1.1.3 Fundamental mediating bosons

There are four fundamental interactions. *Gravity*, *electromagnetism*, the *strong* force, and the *weak* force. Gravity and electromagnetism have been known for a long time, Weak and Color interactions were discovered in the 20th century in the study of nuclear interactions.

The Standard Model requires that each fundamental interaction be mediated by "gauge bosons". The electromagnetic interaction is mediated by the photon (γ). The weak interaction is mediated by massive $W^{\pm}$ and Z^0 bosons and is responsible for all flavor changing decays. The strong interaction is mediated by massless gluons (g). Gravity is mediated by the postulated, but unobserved *graviton*. The Standard Model does not include a description of gravity (at the energy and distance scales of today's particle physics experiments, gravity is very weak). The properties of the gauge bosons are summarized in Table 1.3.

Table 1.3: Properties of the gauge bosons [6]. The properties of the graviton are only postulates.

Boson(s)	Force	Mass (GeV/c^2)	Spin
γ	Electromagnetic	0	1
$W^{\pm}(Z^0)$	Weak	80.4(91.2)	1
g	Strong	0	1
graviton	Gravity	0	2

1.1.4 Weak decays

The quark mass states that we observe are not eigenstates of the weak interaction. By convention the "down-type" (d, s, b) quarks are chosen to be the mixed states. When a transition occur from an "up-type" quark (u, c, t) to a "down-type" quark, via the emission of a W, any "down-type" quark is permitted if kinematically possible. In the case of charm decay only two families are kinematically possible.

For the simple case of the first two generations, the transitions between quark types are described by the transformation postulated by Cabibbo [7]:

$$\begin{pmatrix} d' \\ s' \end{pmatrix} = \begin{pmatrix} \cos\theta_c & \sin\theta_c \\ -\sin\theta_c & \cos\theta_c \end{pmatrix} \begin{pmatrix} d \\ s \end{pmatrix} . \tag{1.2}$$

The parameter θ_c is called the Cabibbo angle and has been experimentally measured to be approximately 0.23 radians. The d and s mass states are viewed as a rotation of the weak eigenstates d' and s'. As a consequence the transitions $c \to s$ and $u \to d$ are proportional to $\cos^2\theta_c$ ("Cabibbo favored") while the transitions $c \to d$ and $s \to u$ are proportional to $\sin^2\theta_c$ ("Cabibbo suppressed"). The value of $\sin^2\theta_c/\cos^2\theta_c$ is approximately $\frac{1}{20}$. The mixing has been expanded to include all three generations of quarks into what is known as CKM matrix.

1.2 Charmed Hadrons

1.2.1 Charm discovery

As explained before, quarks were introduced in the mid-sixties, originally with only three quark flavors (u, d, and s), later Bjorken and Glashow [8] suggested the existence of a fourth (charm) quark. Ten years later (November 1974) two experiments [9, 10] simultaneously announced the discovery of the J/ψ as a narrow resonance with a mass of about 3.1 GeV/c^2. The J/ψ was interpreted as a bound state of a charm and anti-charm ($c\overline{c}$) pair. Subsequently "open charm" particles, such as D^0, D^+ (mesons), and Λ_c^+ [11–13], were experimentally discovered confirming the charm hypothesis, although other experiments [14, 15] had seen indications of so called "open charm" several years before the discovery of the J/ψ.

The discovery in 1977 of Υ [16], a $b\overline{b}$ resonance was the first indication of the third generation of quarks. The discovery of the top quark [17] took until 1995 due to its extremely heavy mass.

The discovery of charm, led to a new era of investigations in heavy-flavor physics. In particular the properties of the charm particles have been investigated in a variety of e^+e^-, $p\bar{p}$ and fixed target experiments as we will see below.

1.2.2 Charmed Baryons

In Figure 1.1 we show a graphical representation of all SU(4) baryons. The singly charmed baryons are on the second level of these multiplets. Since the SU(4) flavor symmetry is badly broken by a mass difference of greater than 1 GeV/c^2 the diagrams in Figure 1.1 are the simplest way to visualize the combinations of charmed baryons that might exist. All of the singly charmed baryons on the second level of Figure 1.1b (shown in Figure 1.2) have been observed. Table 1.4 summarizes the properties of the $L = 0$ singly charmed baryons. In addition, several $L = 1$ Λ_c^+ and Ξ_c excited states have been observed: the $\Lambda_{c1}^{*+}(2593)$, the $\Lambda_{c1}^{*+}(2625)$, and the $\Xi_{c1}(2720)$ [18, 19].

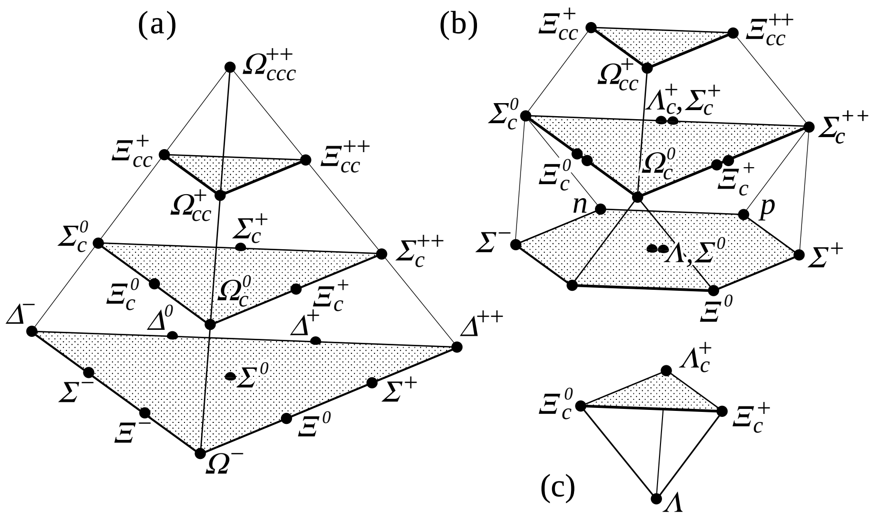

Figure 1.1: SU(4) baryon multiplets which show all the SU(4) baryons present in a four-quark system. (a) The 20-plet with a SU(3) decuplet on the base. (Δ type) (b) The 20-plet with a SU(3) octet on the base (nucleon type). (c) The $\bar{4}$-plet (fully antisymmetric). Extending these diagrams to SU(5) for the baryons containing a b quark would require a 4-dimensional drawing. (Figure from Reference 4.)

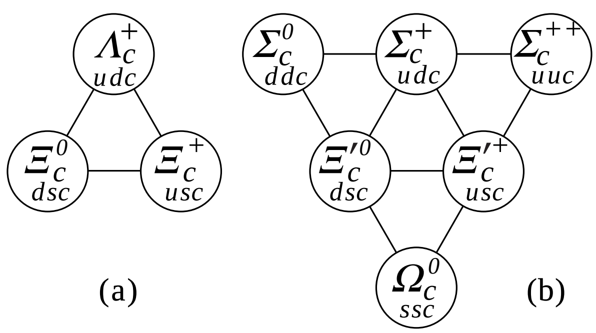

Figure 1.2: SU(3) multiplets on singly charmed baryons of the 20-plet nucleon type, from figure Figure 1.1b. (Figure from Reference 4.)

Table 1.4: Properties of the $L = 0$ charmed baryons [4]. The $I(J^P)$ values of many of these states have not been experimentally measured; in these cases we give the predicted values. The subscript serves to indicate whether the light quark wave function is anti-symmetric (a) or symmetric (s). Baryons with $J = \frac{1}{2}$ belong to the SU(4) multiplet shown in Figure 1.1b while those with $J = \frac{3}{2}$ belong to the multiplet shown in Figure 1.1a.

Baryon	Quark content	Mass (MeV/c^2)	$I(J^P)$
Λ_c^+	$c(ud)_a$	2284.9 ± 0.6	$0(\frac{1}{2}^+)$
Σ_c^0	cdd	2452.9 ± 0.6	$1(\frac{1}{2}^+)$
Σ_c^+	$c(ud)_s$	2453.6 ± 0.9	$1(\frac{1}{2}^+)$
Σ_c^{++}	cuu	2452.8 ± 0.6	$1(\frac{1}{2}^+)$
Σ_c^{*0}	cdd	2517.5 ± 1.4	$1(\frac{3}{2}^+)$
Σ_c^{*+}	cud	2515.9 ± 2.4	$1(\frac{3}{2}^+)$
Σ_c^{*++}	cuu	2519.4 ± 1.5	$1(\frac{3}{2}^+)$
Ξ_c^0	$c(sd)_a$	2471.8 ± 1.4	$\frac{1}{2}(\frac{1}{2}^+)$
Ξ_c^+	$c(su)_a$	2466.3 ± 1.4	$\frac{1}{2}(\frac{1}{2}^+)$
$\Xi_c^{\prime 0}$	$c(sd)_s$	2578.8 ± 3.2	$\frac{1}{2}(\frac{1}{2}^+)$
$\Xi_c^{\prime +}$	$c(su)_s$	2574.1 ± 3.3	$\frac{1}{2}(\frac{1}{2}^+)$
Ξ_c^{*0}	csd	2644.5 ± 1.8	$\frac{1}{2}(\frac{3}{2}^+)$
Ξ_c^{*+}	csu	2647.4 ± 2.0	$\frac{1}{2}(\frac{3}{2}^+)$
Ω_c^0	css	2704.0 ± 4.0	$0(\frac{1}{2}^+)$
$\Omega_c^{\prime 0}$	css	unobserved	$0(\frac{3}{2}^+)$

No doubly or triply charmed baryons have been observed. All of the ground baryons state are expected to decay weakly.

1.2.3 Lifetime of Charmed Hadrons

Singly charmed particles decay via the weak interaction. In a zero order approximation, the lifetime of a particle containing a heavy flavor quark might be estimated with the "spectator model". In this process, it is assumed that while the heavy quark decays to a lighter quarks, the remaining constituents of a hadron (like u, d or s) are spectators and do not participate in the process. Also the decay rate of the heavy quark increases very quickly with its mass ($\Gamma \propto m_Q^5$). In this model, the heavy particle decays by radiating a W, as shown in Figure 1.3. From this model a rough estimate of the quark charm lifetime (scaling from muon decay) is given by

$$\tau_C \simeq \tau_\mu \frac{1}{5}(\frac{m_\mu}{m_C})^5 \sim \ 0.8 \text{ ps}, \qquad (1.3)$$

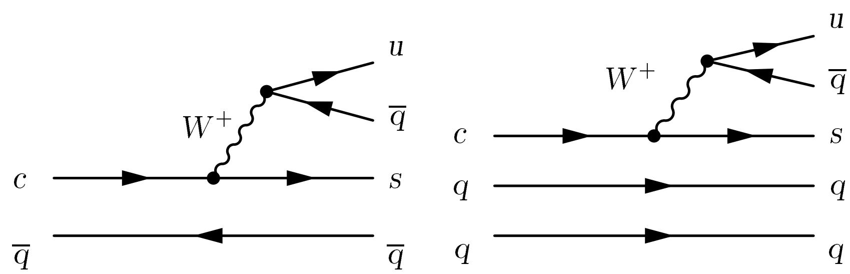

(a) Heavy Meson decay. (b) Heavy Baryons decay.

Figure 1.3: Feynman diagram for the External Decay of a Charmed Hadron, to visualize a the Spectator process.

where m_μ is the mass of the muon, and m_C is the mass of the charm quark. The factor of 1/5 accounts for the two leptons (electron and muon) and three quark colors into which charm quark can decay. This result is consistent with the average of the experimental lifetime of D^+ and D^0 which is about 0.73 ps. Although the spectator model gives a reasonable estimate for the order of magnitude of charmed hadron lifetimes, it is not able to predict the large lifetime differences seen experimentally between different weakly decaying bound states. The longest (D^+) and the shortest (Ω_c^0) lifetimes differ by a factor of about 15. In order to explain these differences, additional effects must be considered.

From recent FOCUS experimental results the ratio of the D^+ lifetime to the D^0 lifetime is 2.538 ± 0.023 [20]. If one combines this result with the branching ratio of semi-leptonic decays [4] we find the D^+ and D^0 semi-leptonic decays widths are nearly equal.

$$\frac{\Gamma(D^0 \to e^+X)}{\Gamma(D^+ \to e^+X)} = \frac{\mathrm{BR}(D^0 \to e^+X)}{\mathrm{BR}(D^+ \to e^+X)} \times \frac{\tau(D^+)}{\tau(D^0)} = 1.00 \pm 0.12 \tag{1.4}$$

This last result imply that any differences in lifetimes are due to hadronic decays.

At the end of 1979 several mechanisms were studied which could contribute to the differences in lifetimes. To explain the unexpected D^+/D^0 lifetime difference two sources were found to be important [21], "Weak annihilation" (WA)[3] and "Pauli Interference" (PI).

[3] The distinction between W exchange in the t channel with weak annihilation in the s channel is an artificial classification because the two operations are mixed under QCD renormalization, although D_s^+/D^0 lifetime differences may reveal some difference between these two diagrams. Both cases will be referred to as WA.

The WA rate (See Figure 1.4) is present in Cabibbo favored (CF) decays of the D^0 mesons, cannot contribute to CF D^+ decays. However the WA rate is doubly suppressed relative to spectator rate. It is helicity suppressed by a factor $(m_s/m_c)^2$ and 'wave function overlap' suppressed by a factor $(f_D/m_c)^2$. Because WA alone cannot account for the D^+/D^0 lifetime difference a second effect (which initially was disregarded) became apparent.

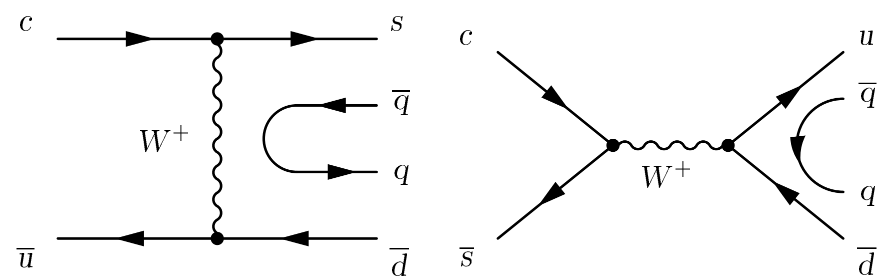

(a) W Exchange. (b) Annihilation.

Figure 1.4: These diagrams compose the non-spectator Weak Annihilation contributions to the charm mesons lifetime. Both are helicity and wave function suppressed.

The PI effect is present in Cabibbo favored D^+ decays but not in D^0. PI causes the D^+ to decay more slowly, because of destructive interference coming from the exchange of two identical antiquarks, the $\overline{d}$ valence antiquark with the $\overline{d}$ from the c decay ($c \to s\overline{d}u$). This interference can be visualized as the interference between the external and internal spectator diagrams shown in Figure 1.5. Both diagrams give the same final state, but the internal spectator decay is color suppressed.

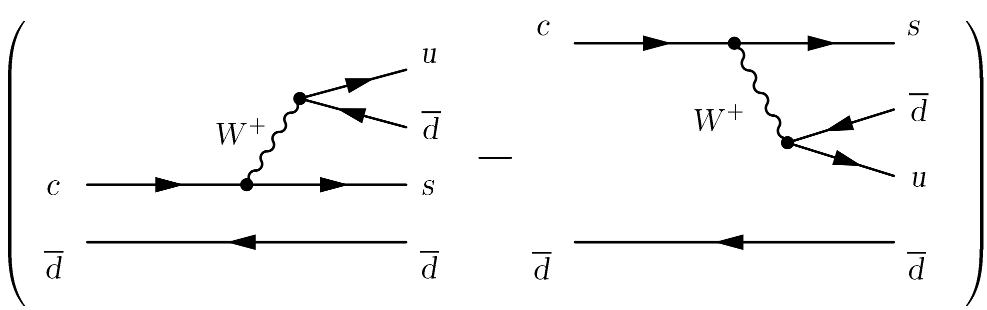

Figure 1.5: The interference of these two diagrams (external and internal spectator) represent the PI in the D^+ decay.

Similarly for charmed baryons three processes were identified, "W Scattering" (WS) which is similar to WA, and PI (constructive and destructive). In baryons, unlike mesons, these mechanisms are neither color nor helicity suppressed. The interference is computed to be constructive when the quark from charm quark decay matches a spectator quark (The exchange of s quarks in Figure 1.6(b)). The interference is computed to be destructive when a quark coming from the decay of the virtual W matches a spectator quark (The exchange of u in Figure 1.6(b)). These contributions are shown in Figure 1.6

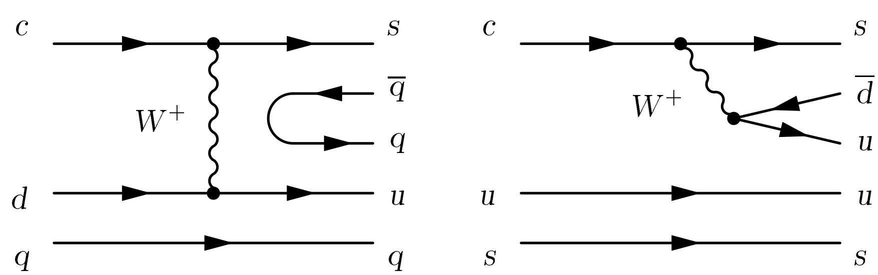

(a) W Scattering. (b) Internal Spectator.

Figure 1.6: Feynman diagrams which contribute to charm lifetimes. These diagram compose the non-spectator contributions, and depend on the initial quark content.

In baryons, the dominant amplitudes to Cabibbo favored hadronic decays are the external spectator (Figure 1.3(b)), the internal spectator (Figure 1.6(b)) and the W scattering (Figure 1.6(a)). The rate of the spectator process is given by the sum of the rates of the external and internal spectators. The interference terms of the amplitudes are better approximated as two terms, the interference due to the u quark which is computed to be destructive and the interference of the s which is computed to be constructive. In mesons the interference term is due to the $\overline{d}$ quark and it is computed to be destructive.

The contributions to the Cabibbo favored hadronic decays for various charmed hadrons are given below:

$$\begin{aligned}
\Gamma_{NL}(D^+) &= \Gamma_{\text{spc}} - \Gamma^-_{\text{int}} \\
\Gamma_{NL}(D^0) &= \Gamma_{\text{spc}} + \Gamma_{\text{WA}} \\
\Gamma_{NL}(D^+_s) &= \Gamma_{\text{spc}} + \Gamma_{\text{WA}} \\
\Gamma_{NL}(\Lambda^+_c) &= \Gamma_{\text{spc}} - \Gamma^-_{\text{int}} + \Gamma_{\text{WS}} \\
\Gamma_{NL}(\Xi^+_c) &= \Gamma_{\text{spc}} - \Gamma^-_{\text{int}} + \Gamma^+_{\text{int}} \\
\Gamma_{NL}(\Xi^0_c) &= \Gamma_{\text{spc}} + \Gamma^+_{\text{int}} + \Gamma_{\text{WS}} \\
\Gamma_{NL}(\Omega^0_c) &= \Gamma_{\text{spc}} + \tfrac{10}{3}\Gamma^+_{\text{int}}
\end{aligned} \qquad (1.5)$$

where Γ_{spc} is the contribution due to the spectator decay process, Γ_{WS} (Γ_{WA}) is the contribution of W Scattering (Weak annihilation in mesons) and $\Gamma^{+}_{\text{int}}(\Gamma^{-}_{\text{int}})$ is the contribution due to constructive (destructive) interference. The interference term for the Ω_c^0 is enhanced due to the presence of three final state s quarks which interfere with each other [22], compared to the Ξ_c^+ or Ξ_c^0. The numerical factor $\frac{10}{3}$ is due to the spin wave function.

In the nineties, all the phenomenological insights were put together in a robust form know as *Heavy Quark Expansion* (HQE) theory (See Reference 23 and references therein). In this theory non-perturbative corrections are put together in a systematic expansion in inverse powers of the heavy quark mass $(1/m_C)^n$, through a technique named *Operator Product Expansion* (OPE). So the weak decay is expressed as:

$$\Gamma(H_C \to f) = \frac{G_F^2 m_C^5}{192\pi^3} |V|^2 \frac{1}{2M_{H_C}} \times \left[\sum_{D=3}^{\infty} c_D^f \frac{\langle H_C | O_D | H_C \rangle}{m_C^{D-3}} \right] \tag{1.6}$$

Where H_C is the heavy hadron, f is some final state, G_F is the Fermi coupling constant, V is the CKM matrix element present in the decay, M_{H_C} is the mass of hadron containing the heavy quark, D is the dimension of the operator O_D, c_D^f are the coefficients of the series.

The HQE is analogous to a fictitious nuclear β decay, where the energy released is much larger than the typical binding energy. Corrections to the simple spectator model which take into account interference between electrons in the shell with the decay electron would be proportional to inverse powers of the energy released.

The theory is based on:

i) a systematic expansion of amplitudes in the inverse mass of the heavy quark (m_C^{-1}).

ii) estimates of matrix elements of local operators (appearing in the expansion) over the hadronic states H_C.

The first condition (i) takes into account the quark-gluon dynamics at short distances and is based on fundamental QCD. The second condition (ii) about the hadronic matrix elements reflects the hadron structure at long distance, and is "limited" because some relevant matrices are not controlled theoretically.

HQE successfully predicts qualitatively the lifetime hierarchy in the charm particles:

$$D^+ > D_s^+ \sim D^0 \geq \Xi_c^+ > \Lambda_c^+ > \Xi_c^0 \sim \Omega_c^0 \tag{1.7}$$

While in mesons the semi-leptonic rates are close, in baryons they are expected to be different. The reason for this difference lies in the PI in semi-leptonic decays where the s quark from $c \to sl^+\nu$ interferes constructively with the spectator s quark. This effect will increase the semi-leptonic rate of the Ξ_c^+, Ξ_c^0, and Ω_c^0 relative to Λ_c^+. This contribution is given by

$$\tilde{\Gamma}_{SL} = \frac{G_F^2 m_C^2}{12\pi}(4\sqrt{\kappa} - 1)|\psi(0)|^2. \tag{1.8}$$

where $|\psi(0)|$ is the wave function at the origin and κ is a correction arising from renormalization. Another contribution to the semi-leptonic decay rates is the spin-colorfield interaction, which only contributes in the case of the Ω_c^0. Because the Λ_c^+, Ξ_c^+, and Ξ_c^0 belong to the anti-triplet shown in Figure 1.2a, the light valence quarks have net spin zero (light cloud), the Ω_c^0 belongs to the sextet of charmed baryons (Figure 1.2b) where the light cloud has spin 1. This contribution is denoted by $\Gamma_{SL}^G(H_C)$ and is non zero only for Ω_c^0.

The enhanced role of PI in semi-leptonic decays necessitates the inclusion of operators corresponding to the previously mentioned effects. Guberina et al [24] updated the predictions of lifetimes and semi-leptonic rates for baryons including semi-leptonic PI effects. The calculations include the Cabibbo suppressed contributions because semi-leptonic PI effects are expected to be very large. The total semi-leptonic rate is given by

$$\Gamma_{SL}(H_C) = \Gamma_{SL}^{spc}(H_C) + \Gamma_{SL}^{G}(H_C) + \Gamma_{SL}^{PI}(H_C) \tag{1.9}$$

where $\Gamma_{SL}(H_C)$ is the spectator contribution with corrections $O(m_C^-2)$ included due to kinematic energy and spin-colorfield interactions. $\Gamma_{SL}^{PI}(H_C)$ for each charmed baryon is

$$\begin{aligned} \Gamma_{SL}^{PI}(\Lambda_c^+) &= \sin^2\theta_c \; \tilde{\Gamma}_{SL} \\ \Gamma_{SL}^{PI}(\Xi_c^+) &= \xi\cos^2\theta_c \; \tilde{\Gamma}_{SL} \\ \Gamma_{SL}^{PI}(\Xi_c^0) &= (\xi\cos^2\theta_c + \sin^2\theta_c) \; \tilde{\Gamma}_{SL} \\ \Gamma_{SL}^{PI}(\Omega_c^0) &= \frac{10}{3}\xi\cos^2\theta_c \; \tilde{\Gamma}_{SL} \end{aligned} \tag{1.10}$$

here θ_c is the Cabibbo angle, ξ is a fitting parameter to account for the ratio of the matrix elements of the operators $(\overline{c}_L\gamma_\mu s_L)(\overline{s}_L\gamma^\mu c_L)$ and $(\overline{c}_L\gamma_\mu q_L)(\overline{q}_L\gamma^\mu c_L)$,where q is a u or d quark.

Similarly, the non-leptonic contributions are calculated by replacing the lepton pair from the virtual W by a quark pair. The non-leptonic contributions are renormalized to take into account the color combinations. As a result the coefficients in the expansion change their values and are expressed in terms of the QCD corrected Wilson coefficients $c_\pm$. As in the semi-leptonic case the spectator contributions include $O(m_C^{-2})$ corrections, with the proper renormalization. The dominant non-spectator contributions in the case of non-leptonic decays, are expressed as:

$$
\begin{aligned}
\Gamma_{WS} &= \frac{G_F^2 m_C^2}{2\pi}[c_-^2 + \frac{2}{3}(1-\sqrt{\kappa})(c_+^2 - c_-^2)]|\psi(0)|^2 \\
\Gamma_{int}^- &= \frac{G_F^2 m_C^2}{2\pi}[\frac{1}{2}c_+(2c_- - c_+) + \frac{1}{6}(1-\sqrt{\kappa})(5c_+^2 + c_-^2 - 6c_+c_-)]|\psi(0)|^2 \\
\Gamma_{int}^+ &= \frac{G_F^2 m_C^2}{2\pi}[\frac{1}{2}c_+(2c_- + c_+) - \frac{1}{6}(1-\sqrt{\kappa})(5c_+^2 + c_-^2 + 6c_+c_-)]|\psi(0)|^2
\end{aligned} \tag{1.11}
$$

The total non-leptonic contribution, including Cabibbo suppressed corrections, is given by

$$
\begin{aligned}
\Gamma_{NL}(\Lambda_c^+) &= \Gamma_{NL}^{spc}(\Lambda_c^+) + \cos^2\theta_c\ \Gamma_{WS} - \Gamma_{int}^- + \sin^2\theta_c\ \Gamma_{int}^+ \\
\Gamma_{NL}(\Xi_c^+) &= \Gamma_{NL}^{spc}(\Xi_c^+) + \xi\sin^2\theta_c\ \Gamma_{WS} - \Gamma_{int}^- + \xi\cos^2\theta_c\ \Gamma_{int}^+ \\
\Gamma_{NL}(\Xi_c^0) &= \Gamma_{NL}^{spc}(\Xi_c^0) + (\cos^2\theta_c + \xi\sin^2\theta_c)\Gamma_{WS} + (\cos^2\theta_c + \xi\sin^2\theta_c)\Gamma_{int}^+ \\
\Gamma_{NL}(\Omega_c^0) &= \Gamma_{NL}^{spc}(\Omega_c^0) + \Gamma_{NL}^G + \xi\sin^2\theta_c\frac{10}{3}\Gamma_{WS} + \xi\cos^2\theta_c\frac{10}{3}\Gamma_{int}^+
\end{aligned} \tag{1.12}
$$

The different contributions included in these calculations do not significantly alter the overall picture of charm lifetimes and semi-leptonic rates. They do give a quantitative prediction which can be compared with experimental results. Guberina predicts a Ξ_c^+ lifetime that is somewhat smaller than present experimental results [4] but agrees within the experimental uncertainties. This thesis presents the most precise lifetime measurement of the Ξ_c^+ to date, and provides an important test of theoretical predictions, and of the validity of HQE in the charm sector.

1.3 Photoproduction of Charmed particles

The charm quark can be produced by several types of processes. Some of these processes are high energy e^+e^- annihilation (e^+e^- colliders like CESR at Cornell), hadron-hadron collisions like E791 at Fermilab or photon-hadron collisions like E831/FOCUS at Fermilab. The e^+e^- interaction is the cleanest way to produce charmed particles, but the absolute production rates are limited due to cross section and luminosity. Hadron-hadron collisions produce large rates of charm particles but also tend to produce large numbers of non-charm particles leading to large backgrounds. The photon-hadron collisions (photoproduction) have a large production rate compared to e^+e^- and are cleaner compared to hadro-production. Charm hadrons constitute about 1% of all hadrons produced at FOCUS.

Photoproduction of charmed particles is interpreted in the context of the perturbative QCD model called *Photon Gluon Fusion* [25] in which a $c\overline{c}$ pair is produced from the

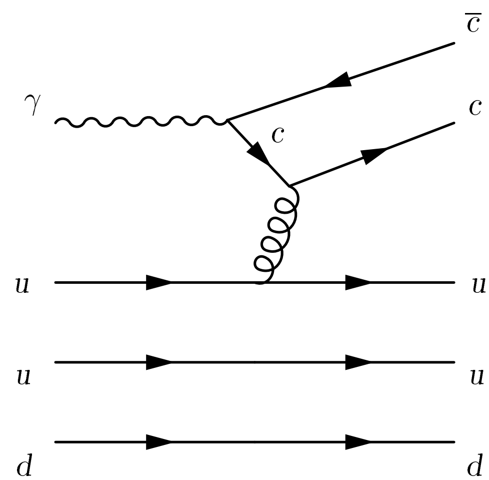

Figure 1.7: Diagram of the photon-gluon fusion process producing a $c\overline{c}$ pair.

interaction of a photon with a gluon coming from the target nucleon. A diagram for this process is shown in Figure 1.7.

Virtually all the photon energy is transferred to the $c\overline{c}$ pair and the charmed particles are boosted forward. The large boost makes it possible to separate the production and decay vertices of charm particles allowing for their direct observation. The data used in the analysis of this thesis comes from the experiment E831/FOCUS, a photoproduction experiment in the Fermilab fixed target program.

Chapter 2

The FOCUS Beamline

In order to produce charmed particles, high energy photons must first be created. This is a multi-step process. The first section of this chapter describes the proton acceleration process at Fermilab. The second section describes the method used by FOCUS to obtain high energy photons from protons. The final section describes the method used to measure the energy of these photons.

2.1 The 800 GeV Proton Beam

A beam of 800 GeV of protons is obtained at Fermilab (Fermi National Accelerator Laboratory) in five stages, starting from a hydrogen gas source.

Stage 1: The pre-accelerator Cockcroft-Walton is a device in which ordinary hydrogen gas is ionized negatively (H^-) and accelerated electrostatically through a single voltage gap to an energy of 0.75 MeV.

Stage 2: The negative hydrogen ions enter into a LINear ACcelerator (LINAC) which is a series of alternating high field and field free regions. The array of alternating fields is designed to accelerate the ions over a distance of 150 meters, reaching an energy of 400MeV. After exiting the LINAC, the ions pass through a thin carbon foil which removes the electrons, leaving only the positive charged protons.

Stage 3: The protons are accelerated in the Booster, which is a rapid cycling synchrotron. The Booster is about 152 meters (500 feet) in diameter. Protons travel

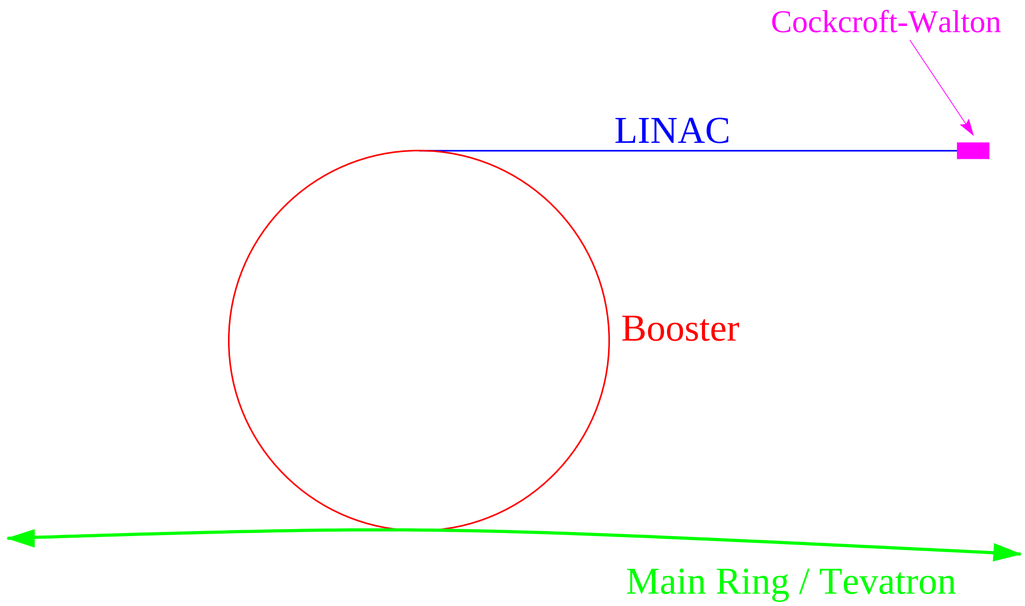

Figure 2.1: Schematic diagram of the arrangement of the Cockcroft-Walton, LINAC, and Booster.

around the Booster about ∼20000 times before they reach an energy of 8000 MeV (8 GeV). The first 3 stages are shown in Figure 2.1. Each time around the ring, the protons are given a boost with a rf field.

Stage 4: The protons are injected into the Main Ring, which is a synchrotron one kilometer in radius, and which is constructed using normal steel dipole magnets. The protons are accelerated to 150 GeV before being injected into the Tevatron.

Stage 5: The Tevatron is also a synchrotron which accelerates protons to 800 GeV and occupies the same tunnel as the Main Ring. The Tevatron uses liquid helium cooled, superconducting dipole magnets to contain the proton beam. The Tevatron accelerates protons to a final energy of 800 GeV. A simplified view of the Tevatron, the Main Ring, and the Fixed Target beamlines is shown in Figure 2.2.

The process of accelerating protons takes about 40 seconds, after which the beam is slowly extracted from the Tevatron to the fixed target beamlines, in a process which takes roughly 20 seconds. The extracted protons are directed to the "switchyard" where the beam is split and sent to three major areas designated as "Proton," "Neutrino," and "Meson." The beams in each of these areas are split again into many less intense beamlines, as shown in Figure 2.2. The E831/FOCUS Experiment is located at the end of the Proton experimental area.

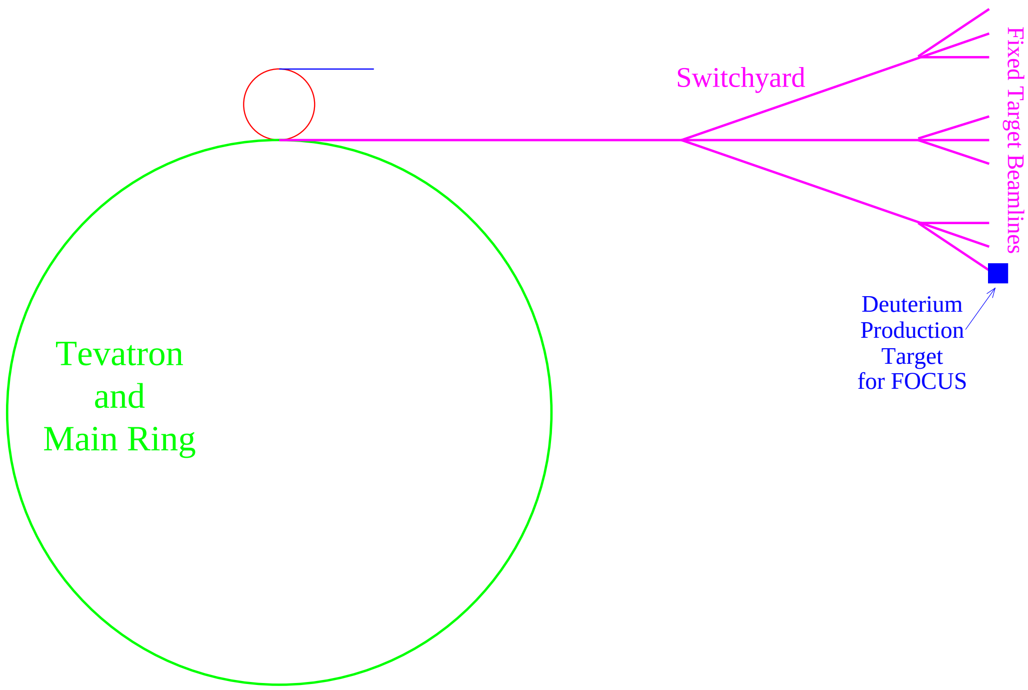

Figure 2.2: Schematic diagram of the arrangement of the Main Ring, the Tevatron, and the Switchyard.

2.2 The Wideband Photon Beamline

The goal of obtaining a clean high energy photon beam is accomplished as follows. The proton is directed onto a liquid deuterium target where a many particles are produced by hadronic interactions. Deuterium is used because it maximizes the ratio of the hadronic interaction length to the radiation length which scales as A/Z^2. The objective is the production of neutral pions which immediately decay ($\tau \sim 10^{-16}$ s) into a pair of photons.

Charged particles are removed from the beam with sweeping magnets. At this point the photon beam is still contaminated with other neutral particles such as neutrons, K^0_L's and Λ^0's. The photons and other neutral particles impinge on a lead foil (the "converter") where the e^+e^- electron-positron pairs are created.

The converter is ∼50% of a radiation length. The thickness is chosen so that photons convert to e^+e^- pairs, but it is unlikely that the contaminants (neutrons, K^0_L's and Λ^0's) will interact hadronically. The $e^\pm$ are then collected by beam transports which are composed of an array of dipole and quadrupole magnets. The $e^\pm$ are bent around a "neutral dump". To achieve an intense beam of high energy photons, it is necessary to collect electrons and positrons passing around the dump over a large range of angles and momenta. The optics of the Wide Band Beam are designed to collect electrons and positrons with a range of ±15% around a central momentum which for most of the FOCUS running was set to 300 GeV.

The e^+ and e^- are transported around the dump in separate beamlines, but are later reunited as shown in Figure 2.3. The two beams are recombined into a single beam by the momentum recombining dipoles. The combined beam is focused to the experimental target and is passed through a thin lead foil (the “radiator”) to produce photons by bremsstrahlung. The radiator is a sheet of lead 20% of a radiation length thick. The expected hadronic background in the photon beam is $\sim 10^{-5}$ per photon.

2.3 The Photon Beam Tagging System

The purpose of the tagging system is to determine the energy of the interacting photon on a event by event basis. The incident electron/positron momentum is measured by the electron beam tagging silicon detectors. After the electron/positron strikes the radiator to produce photons, they are momentum analyzed in the Radiated Electron Shower Hodoscope (RESH) or Positron Shower Hodoscope (POSH) detector. Electrons/positrons are identified by the ratio of their energy to momentum (E/p) in the RESH/POSH hodoscope. To take into account bremsstrahlung radiation of multiple photons not all of which interact in the experimental target, we use the Beam Gamma Monitor (BGM) calorimeter to measure the zero degree energy. The energy of the interacting photon, is given by

$$E_\gamma = E_i - E_f - E_{\text{non}} \tag{2.1}$$

where E_γ is the energy of the interacting photon, E_i is the energy of the incident electron/positron, E_f is the energy of the electron/positron after it strikes the radiator and E_{non} is the energy of non-interacting photons in the BGM. A brief description of the detectors used to measure this quantities is given below.

2.3.1 Electron beam tagging system

The electron beam tagging (or “tagging”) system consists of five planes of silicon strip detectors, two detector upstream of the momentum recombination dipoles, one positioned in a gap between the two upstream dipoles and two downstream the dipoles. Each detector has 256 strips of 300 μm thickness. The active area of each plane is 7.7 cm wide by 5.7 cm high. The tagging system only measures the position in the bend (horizontal) view. The momentum resolution of the tagging system is about 2% ($\sigma_E = 0.02E_e$). A detailed description can be found in Reference 26.

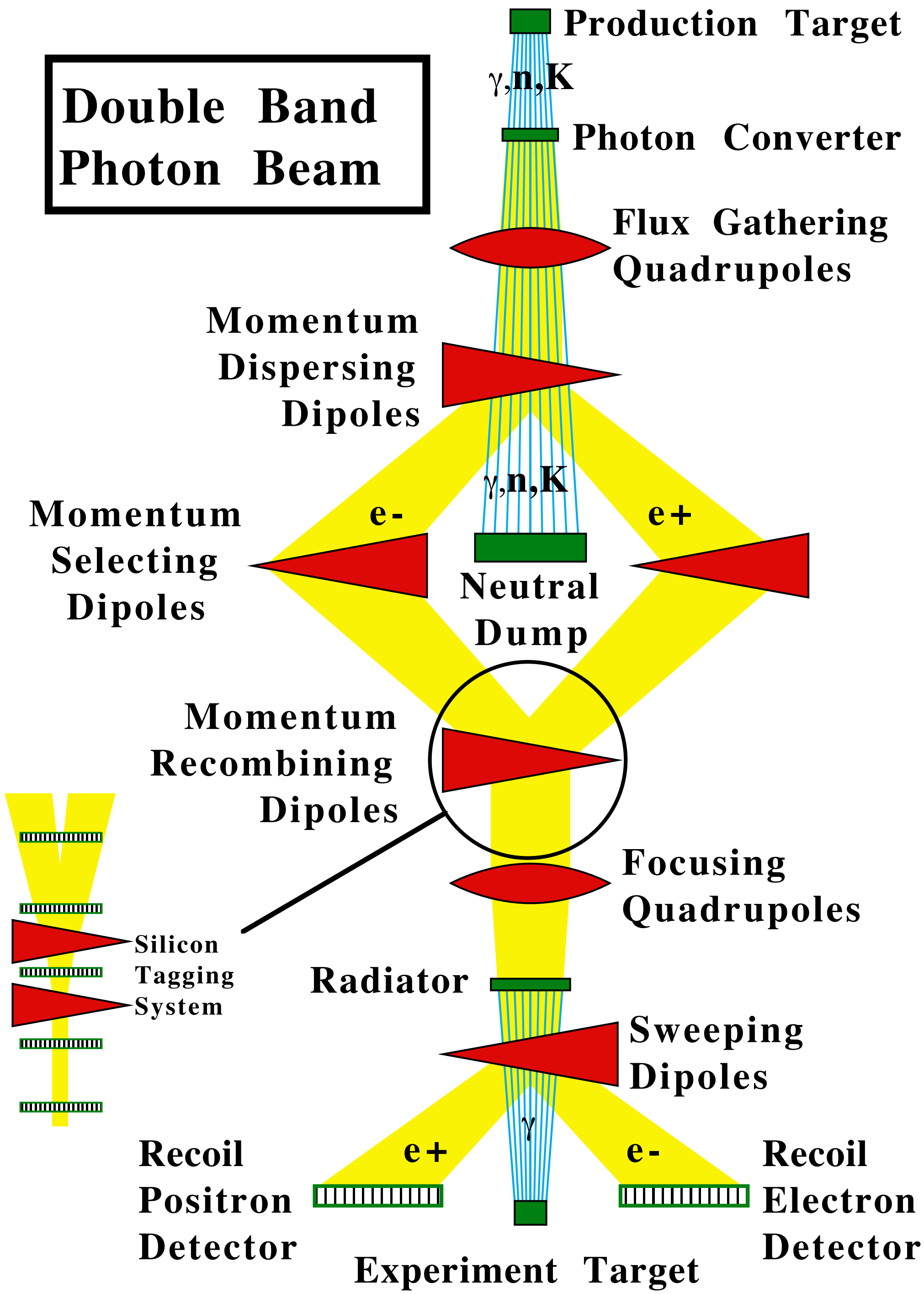

Figure 2.3: A schematic view of the major elements of the Wide Band photon beamline. The inset shows the tagging system of the electrons.

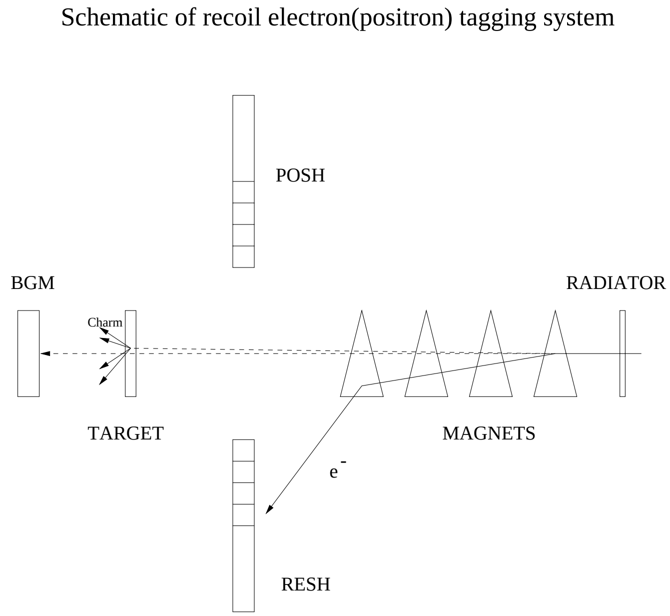

Figure 2.4: Schematic view of the RESH, POSH, and BGM calorimetry system. Electrons/Positrons are deflected into the RESH and POSH. RESH0 and POSH0 are the counters closest to the beam. Noninteracting photons impact the BGM.

2.3.2 RESH and POSH calorimeters

The electron/positron is swept away with dipole magnets after it strikes the radiator. The calorimeters have 13 counters each, labeled 0-12. The counters RESH0 and POSH0 were designed to detect electrons/positrons which do not radiate. Both counters use lead and SiO_2 chosen for its high degree of radiation hardness. RESH1-12 and POSH1-12 use alternating layers of lead and lucite. RESH and POSH are sampling calorimeters with the array of counters as shown in Figure 2.4. By resolving which counter of the RESH or POSH the recoil particle strikes, we know the bend angle of the electron/positron and thus its energy. The energies that the counters sample are listed in Table 2.1.

2.3.3 Beam Gamma Monitor calorimeter

The BGM is a forward electromagnetic calorimeter positioned near the point where e^+e^- produced in the target are focused by the spectrometer magnets (Section 3.4). The BGM transverse area is a square of 9" by 9" and is composed of 24 alternating layers of lead and SiO_2.

Table 2.1: Nominal energies for RESH & POSH counters with a 300 GeV incident electron beam. The central values of the recoil energies measured by each RESH & POSH counter are listed below.

Counter #	Energy (GeV)	
	RESH	POSH
0	251.7	252.3
1	153.7	152.1
2	117.2	116.2
3	94.7	94.1
4	79.5	79.0
5	68.4	68.1
6	60.1	59.8
7	53.6	53.4
8	48.3	48.2
9	41.6	39.5
10	32.3	30.0
11	41.7	41.7
12	14.9	14.9

The RESH, POSH, and BGM each have a total depth of 24 radiation lengths and are composed of radiation hard material.

Chapter 3

The FOCUS Spectrometer

The FOCUS spectrometer is a forward spectrometer with two dipole magnets of opposite polarity and excellent particle identification. Charged particle tracking is accomplished by a system of silicon strip detectors and multiwire proportional chambers which are interleaved with the magnets to provide good momentum determination. Particle identification is obtained by three Čerenkov counters and by two muon detectors. Other particle detectors include two electromagnetic calorimeters and a hadronic calorimeter.

A schematic representation of the FOCUS spectrometer is shown in Figure 3.1. The terms “upstream” and “downstream” will be used to describe the relative position of the detectors in the spectrometer taking as a reference the beam direction. The spectrometer is divided into two portions called “inner” and “outer”. The inner portion subtends angles less than 30 mrad and uses the whole range of spectrometer. The outer portion subtends angles greater than 30 mrad and less than about 150 mrad and consists of the portion of the spectrometer up to the second magnet.

The FOCUS spectrometer is an upgraded version of the FNAL-E687 spectrometer which is described in Reference 27. The structure of the spectrometer is the same, but many detectors were replaced and upgraded. Changes made to the spectrometer are described in Reference 28.

In the following sections, the individual detectors are described.

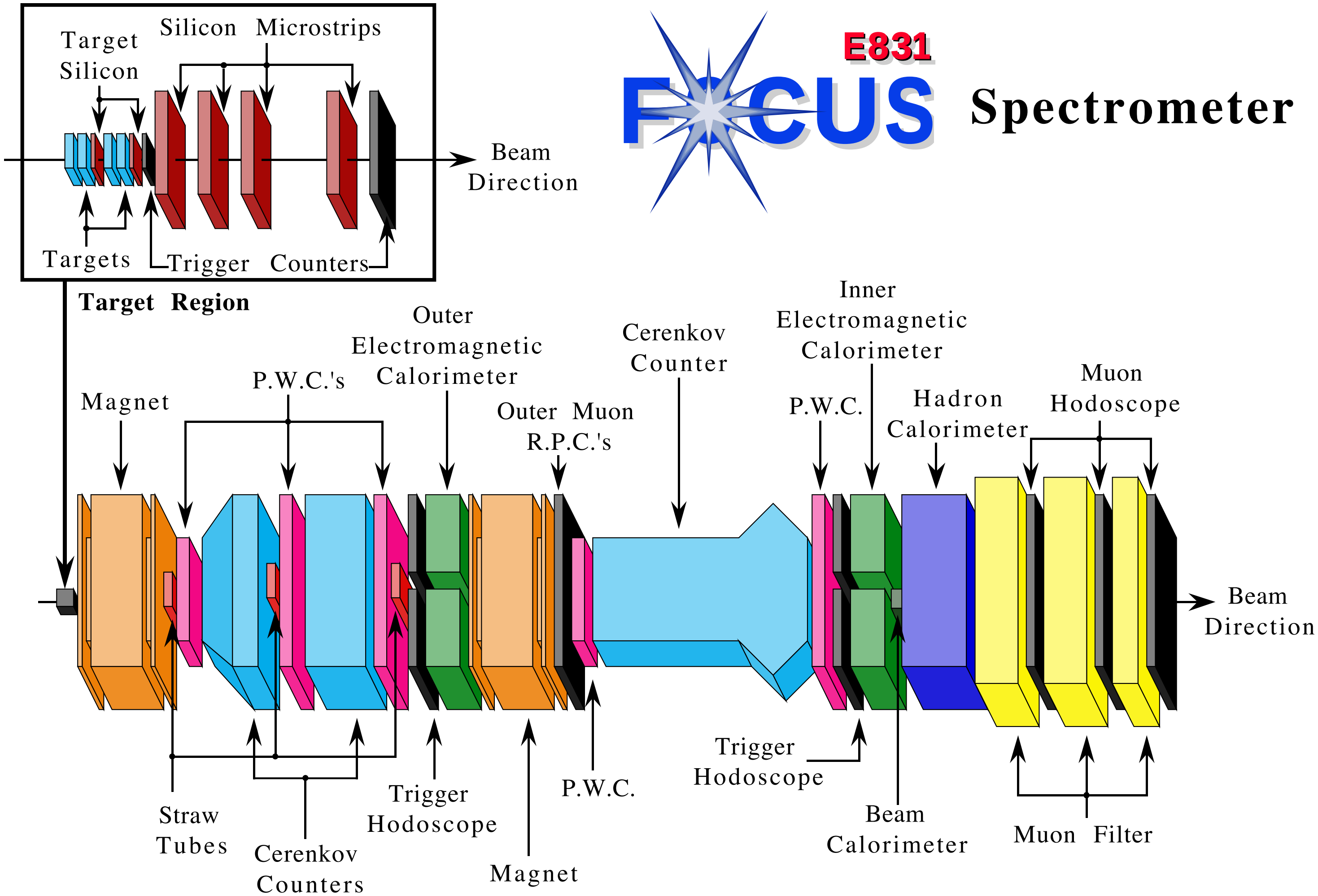

Figure 3.1: An overview of the elements of the FOCUS spectrometer. The inset shows an expanded view of the target region which is also shown in Figure 3.2.

3.1 Target Configuration

Based on the experience of E687 in which the charm signal was improved by requiring secondary decay vertices to be outside of the target material [29], FOCUS used for most of the running (about 2/3) a segmented beryllium oxide (BeO) target with embedded silicon strip detectors. The segmentation allows a larger number of "out of target" decays. The multiple interaction processes that occur within the target is reduced with this configuration. The multiple interaction processes causes "fake" detached vertices as the major source of background, being hard to model. The out of target reconstructed vertices have their source of background in other charm decays which are easier to model.

Taking into account that electromagnetic interactions scale with Z^2, where Z is the atomic number, and that the hadronic interaction interactions scale as $A^{2/3}$ where A is the atomic mass, the target material chosen was BeO. The idea is to minimize as much as possible the pair creation, so one chooses a material with low Z material. At the same time we want to maximize the hadronic interaction requiring high A and a high density material. The higher density allows for the use of thin target segments which serves to increase the number of "out of target" decays.

The last target configuration used in FOCUS is shown in Figure 3.2 and in the inset of Figure 3.1. It consists of four square target segments, 25.4 x 25.4 mm^2 with a thickness of 6.75 mm. Downstream of the first two targets and upstream the last two targets is the first station of the target silicon strip detector (TSSD). The second station of the TSSD is located downstream the four target segments. Other configurations used in early runs are a single beryllium target, segmented beryllium targets and segmented BeO targets.

3.2 Silicon Microstrip Tracking

The silicon microstrip detectors are composed of individual strips which collect the charge freed when charged particles transverse the silicon and ionize the material in the form of electrons and holes. The collected charge is amplified and digitized at the end of the strips. The strips width varies from 25 μm to 100 μm, which allows for excellent spatial localization.

FOCUS uses two silicon microstrip systems. The first is embedded between the target segments and the second is located downstream the targets. A schematic diagram of the target is presented in Figure 3.2.

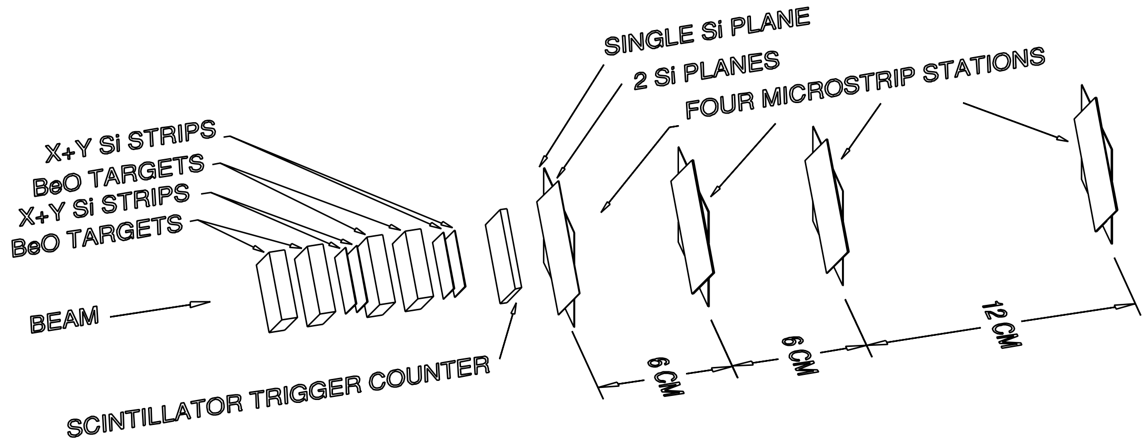

Figure 3.2: Diagram of the target region. Shown are the BeO targets, the embedded silicon microstrip (TSSD) planes, the downstream silicon microstrip (SSD) planes, and a trigger counter separating both silicon systems. The beam enters from the left.

3.2.1 The embedded stations or TSSD

This system is not used directly in the track reconstruction, but is used to extend tracks to the production and secondary vertices and to increase the vertex resolution by reducing the lever arm due to multiple Coulomb scattering. As previously described, the TSSD is embedded in the target region and contains two stations. Each station has two views oriented at $\pm 45°$ to the horizontal. Each view has 1024 strips with each strip having a width of 25 μm and a length of 5 cm. The total active area is 50×25 mm^2 per plane. The thickness of each station is about 300 μm. The readout is done using ADCs (Analog to Digital Converters) [30].

The TSSD was installed for the 1997 running period, and was available for about 2/3 of the data collected by FOCUS.

3.2.2 Downstream stations or silicon strip detector

The Silicon Strip Detector (SSD) is located about 5 cm downstream of the last target segment. The SSD consists of four stations of detectors as shown in Figure 3.2. Each station has 3 views oriented at $-135°$, $-45°$, and $-90°$ with respect to the horizontal, from most upstream to most downstream; with a total of 12 silicon planes. The planes are separated by 5 mm.

The spacing of the strips in each plane are divided in two regions; the inner region and the outer region. The spacing of the inner strips is half the spacing of the outer region, with a total of 688 strips per plane. For the most upstream station the spacing of the strips are 25 μm in the inner region and 50 μm in the outer region. The strip spacing for remaining stations are 50 μm in the inner region and 100 μm in the outer region.

The properties of the SSD stations are summarized in Table 3.1 and are described in greater detail in Reference 31.

Table 3.1: The properties of the SSD planes. Station 1 is the most upstream station (closest to the target).

Station	Active Area		Strip Pitch
	Total	High Res.	
1	2.5×3.5 cm^2	1.0×3.5 cm^2	25 μm, 50 μm
2	5.0×5.0 cm^2	2.0×5.0 cm^2	50 μm, 100 μm
3	5.0×5.0 cm^2	2.0×5.0 cm^2	50 μm, 100 μm
4	5.0×5.0 cm^2	2.0×5.0 cm^2	50 μm, 100 μm

3.3 Multiwire Proportional Chambers

A multiwire proportional chamber (MWPC) is a device constructed with alternating planes of high voltage wires and ground wires. The planes are separated on the order of millimeters with the typical high voltage on the order of kilovolt. The MWPC is filled with a gas which ionizes when a charged particle passes through the gas in the chamber. The ions are then accelerated towards the wires by the electric field, ionizing more of the gas, beginning a cascade process of charge which is deposited on the ground wires. The cascade process can be amplified by reducing the diameter of ground wires because this increases the field gradient near the wire resulting in an increase of chamber efficiency.

The MWPCs used in FOCUS consist of five stations; labeled from upstream to downstream P0, P1, P2, P3, and P4 as shown in Figure 3.1. The first three stations are located between the two analyzing magnets, the remaining two stations are located downstream of the second magnet. This configuration allows for two independent measurements of momentum for charged particles which are tracked throughout the entire spectrometer. For charged particles which are outside of the second magnet aperture the momentum information is provided by the bend angle of the first magnet.

Each station has four views Y, U, V, and X in order upstream to downstream. The X view is a plane with wires running vertically to measure the horizontal position. The Y view wires run horizontally to measure the vertical position, and the U and V views are inclined at $\pm 11.3°$ from the Y view. The U and V views are used to resolve ambiguities and to provide a better momentum resolution. The gas used to operate

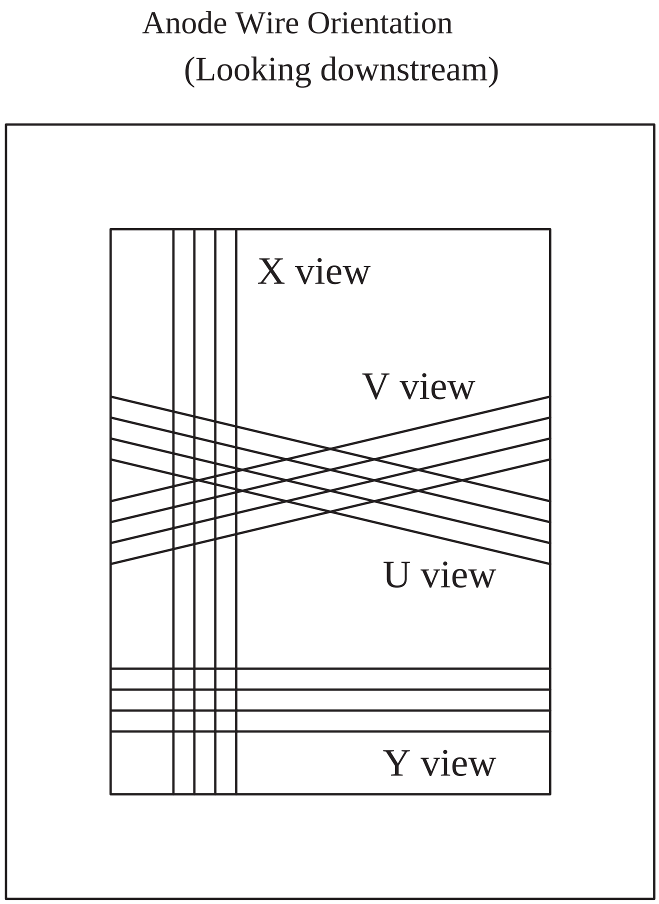

Figure 3.3: Orientation of the MWPC wire planes, showing the $\pm 11.3°$ angle of the U and V planes with respect to the Y view.

the chambers is a mixture of 75% argon and 25% ethane bubbled through methyl alcohol. The arrangement of wires in a MWPC station is shown in Figure 3.3.

Two types of MWPC stations were used in the FOCUS spectrometer, Type I (P0 and P3) and Type II (P1, P2, P4).

Type I stations are located just downstream of each magnet and have an aperture of 76 cm $\times$ 127 cm to match the magnets aperture. The ground wires are 0.8 mil diameter gold-plated tungsten with a wire spacing of 80 mils. The gap between high voltage planes and the grounded wires is 0.47 in.

Type II stations have an aperture of 152 cm $\times$ 229 cm. The ground wires are 1.0 mil diameter gold-plated tungsten with a wire spacing of 120 mils. The gap between high voltage planes and the grounded wires is 0.48 in.

The details of the five chambers are summarized in Table 3.2.

Table 3.2: A summary of the properties of the five multiwire proportional chambers.

Wire Chamber	Wire spacing	Wires/plane				Size ($X \times Y$)	Position (cm from target)
		X	Y	U	V		
P0	0.080"	376	640	640	640	76×127 cm^2	403
P1	0.130"	480	704	768	768	152×229 cm^2	644
P2	0.130"	480	704	768	768	152×229 cm^2	879
P3	0.080"	376	640	640	640	76×127 cm^2	1,444
P4	0.130"	480	704	768	768	152×229 cm^2	2,286

3.4 Analysis Magnets

The momentum analysis of a charged particle tracked through the spectrometer is accomplished by two large dipole magnets. The first magnet (M1) located downstream of the SSD and before P0 (about 225 cm downstream the target) ran at a current of $\sim$ 1020 amps giving a tranverse momentum kick of 0.400 GeV/c. The second magnet (M2) located about 1240 cm downstream the target ran at a current of $\sim$ 2000 amps for a transverse momentum kick of 0.850 GeV/c. The magnets are oriented to bend particles in the vertical direction, with M1 and M2 bending in *opposite* directions. Each magnet is 1.7 m long, with an aperture of 76 cm horizontal (non-bend view or X-view) by 127 cm vertical (bend view or Y axis) and a mass of about 245,000 kg.

Because of the large background of e^+e^- pairs produced in the target; they need to be suppressed. The arrangement of magnets take advantage of the small opening angle of e^+e^- pairs. Electrons and positrons in M1 open up vertically, while the horizontal width is about the horizontal beam size. After M2, the particles are bent back towards the beam axis, focusing onto the Beam Gamma Monitor (Section 2.3.3), with some smearing due to energy loss of the particles from bremsstrahlung in the material of the spectrometer. A schematic of this bending is presented in Figure 3.4.

By comparison, hadronic events are more spread out in angle and generally have at least two particles outside the pair region at the downstream end of the spectrometer. This crucial difference between e^+e^- produced events and hadronic events is exploited by the trigger as discussed in Section 3.9.

3.5 Straw Tube Chambers

The straw tube chambers work similarly to the MWPC, but instead of the high voltage being supplied along a plane, the high voltage is maintained on a metal coated tube (straw) with a ground wire in the center. This arrangement makes it possible, for each

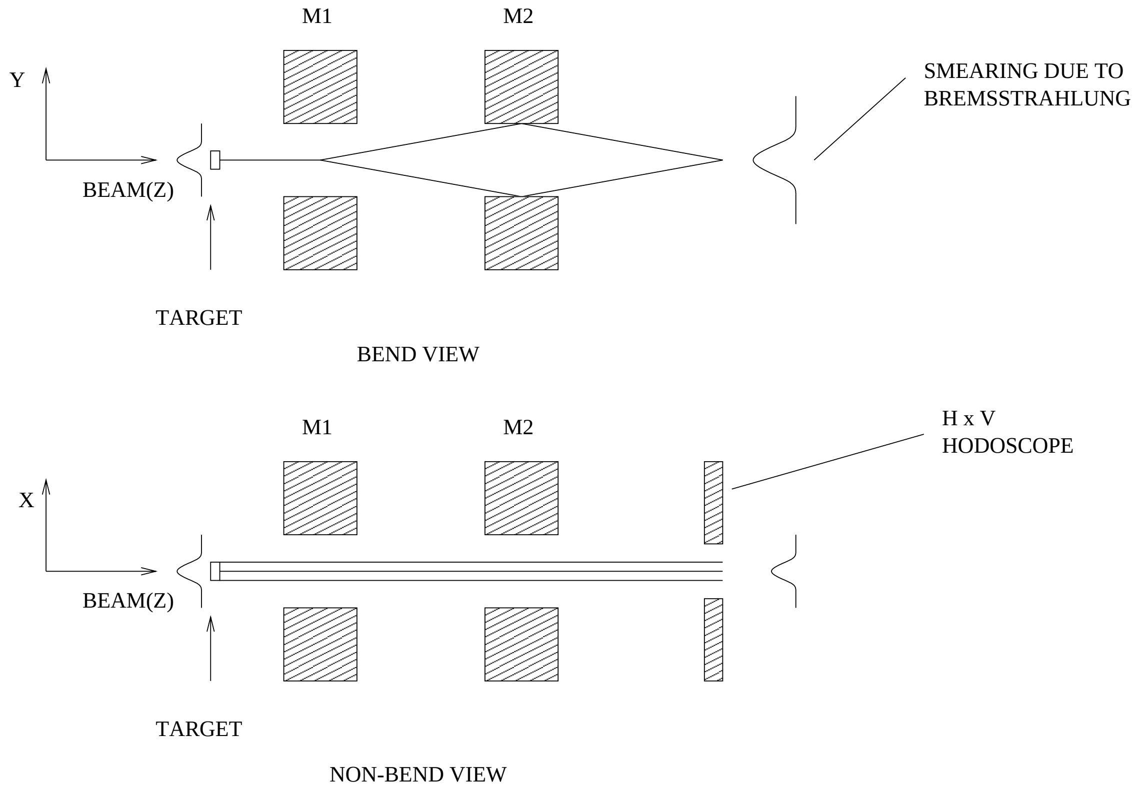

Figure 3.4: Schematic topology of the geometric distribution of e^+e^- event.

wire, to have its own electric field and be able to work in higher rate environments. It also provides more reliability since a single broken wire only impacts one channel.

The original purpose of the straw tubes was to handle the high rates in the pair region due to a concern that the MWPC would become "deadened" in this region. Three straw tube chambers were constructed to cover the pair region for each of the three upstream MWPC.

Three straw tube chambers were constructed. The first two, were in front of P0 and P1 and the last one was just behind P2; with their respective labels being ST0, ST1, and ST2. All chambers had 5 mm straw diameters. Each chamber has three views, one vertical and two aligned at $\pm 11.3°$ from vertical. The schematic of the straws is shown in Figure 3.5 and the properties are summarized in Table 3.3.

Table 3.3: A summary of the properties of the three straw tube chambers.

Straw Chamber	Straw length	Wires/view		Total Wires
		Vertical	Angled	
ST0	138 cm	3×10	3×38	258
ST1	241 cm	3×10	3×74	474
ST2	241 cm	3×10	3×74	474

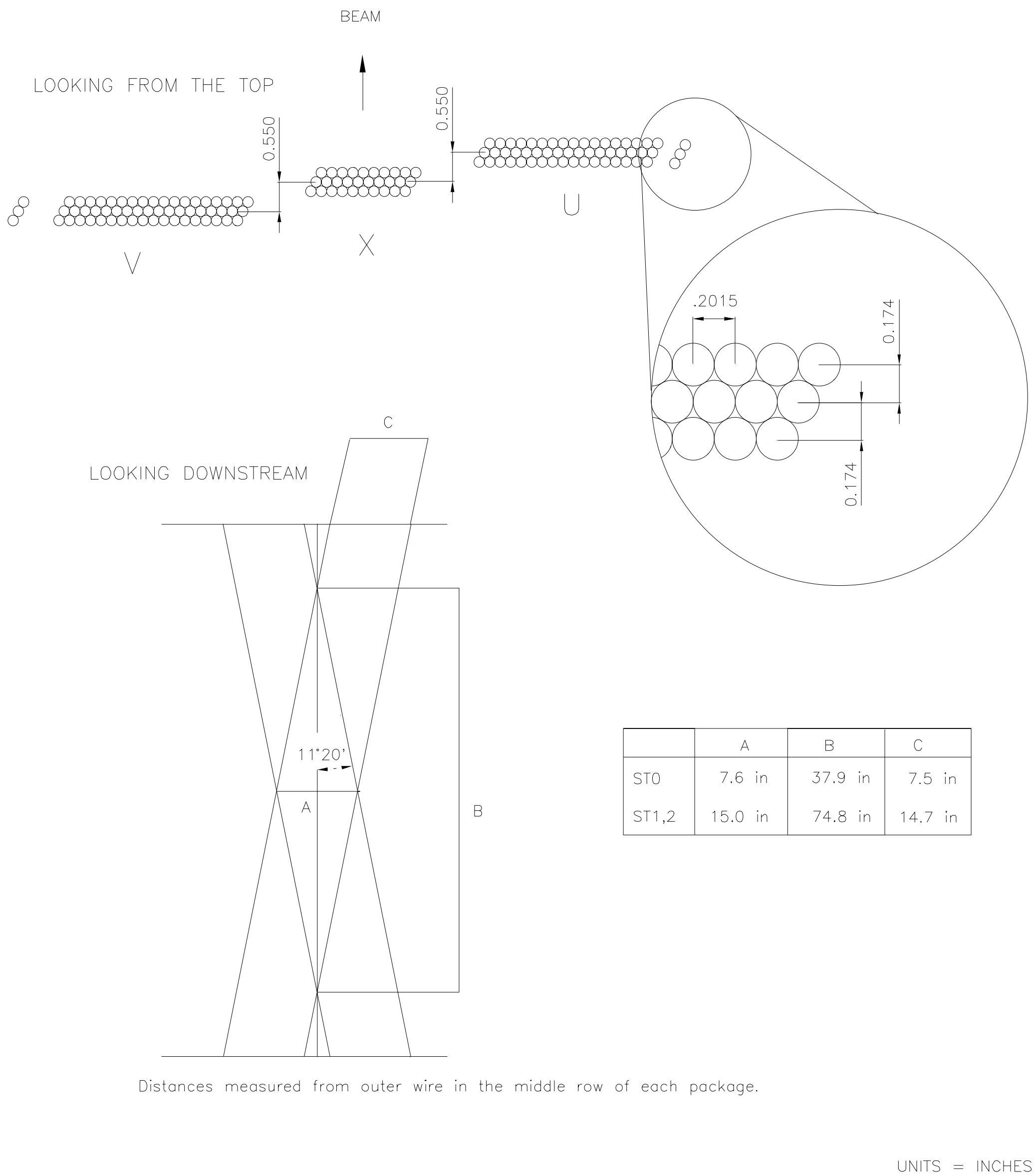

	A	B	C
ST0	7.6 in	37.9 in	7.5 in
ST1,2	15.0 in	74.8 in	14.7 in

Figure 3.5: Diagram, including measurements, showing the construction of ST0, ST1, and ST2.

During the running, it was discovered that MWPC system did not need to be deadened. Thus, tracking was done with MWPC system alone.

3.6 Čerenkov System

It is well known that when charged particles travel faster than the speed of light *in a medium*, they emit Čerenkov radiation. This means, light is emitted at an angle

$$\theta_c = \cos^{-1}(\frac{1}{n\beta}) \quad \text{if} \quad \beta > \frac{1}{n} \tag{3.1}$$

where n is the index of refraction of the material and β is the velocity of the charged particle in units of the speed of light; as shown in Figure 3.6.

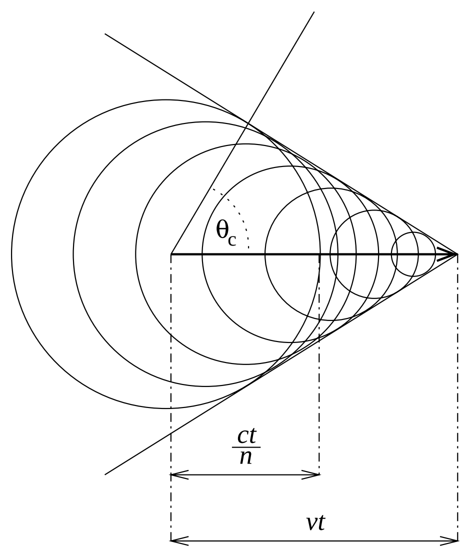

Figure 3.6: Origin of Čerenkov radiation. This figure shows the wavelets of fields (circles) emanating from a charged particle moving along the horizontal line. When the speed of the particle exceeds c/n, a "shock wave" builds along the angled lines, resulting in the propagation of electromagnetic energy (light) at the angle θ_c. (Figure adapted from Reference 32.)

The threshold velocity is defined as the velocity of the particle when it starts to radiate Čerenkov light ($\beta_{\text{thresh}} = \frac{1}{n}$). This implies different momentum thresholds for different particles. The momentum threshold depends only on the mass of the charged particle and the index of refraction of the material as given by

$$p = \frac{m\ c\ \beta}{\sqrt{1-\beta}} \ \rightarrow \ p_{\text{thresh}} = \frac{m\ c}{\sqrt{n^2-1}} \tag{3.2}$$

where p is momentum and c the speed of light.

The FOCUS spectrometer uses three threshold Čerenkov detectors. Given a track and its momentum, we to determine the four particle identification possibilities e, π, K, and p. To accomplish the particle identification, gases have been chosen to work in a wide momentum range in which pions, kaons, and protons can be distinguished from each other. The three Čerenkov detectors are labeled as C1, C2, and C3, and have the properties summarized in Table 3.4.

Table 3.4: Gases and threshold momenta of the three Čerenkov detectors.

Detector	Gas	Threshold (GeV/c)			No of Cells	Ave Number of Photoelectrons
		π	K	p		
C1	58% He/42% N_2	8.5	29.9	56.8	90	2.5-3.6
C2	N_2O	4.5	16.2	30.9	110	8-11
C3	He	17.0	61.0	116.2	100	9

A brief description of each Čerenkov detector is given below.

C1: This detector is the most upstream Čerenkov, located between P0 and P1. The gas is a mixture of 58% helium, 42% nitrogen, which gives a pion threshold of 8.5 GeV/c. The detector covers a transverse area of 80" (vertical) x 50" (horizontal) with 90 cells. The cells are divided in two portions, the outer portion which uses spherical mirrors and the inner portion which uses two planar mirrors oriented at $\pm 45°$ to the beam (50 cells). The cell information is obtained with photomultiplier tubes (PMT) readout by collecting the reflected light from either focusing (outer) in the PMTs or through Winston cones (inner), which reflect incident light into the apex of the cone. The cell geometry of C1 is shown in Figure 3.7a.

C2: This detector has similar design to C1; located between P1 and P2 and filled with nitrous oxide (N_2O) gas, which gives a pion threshold of 4.5 GeV/c. The dimensions of C2 are 100"(vertical) x 64"(horizontal) with 110 cells (56 in the outer region and 54 in the inner region). The light from the outer region is focused to the PMTs with spherical mirrors, while the light from the inner region is reflected toward the PMTs using 32 planar mirrors and with help of Winston cones. The cell structure of C2 from the beam's eye view is shown in Figure 3.7b.

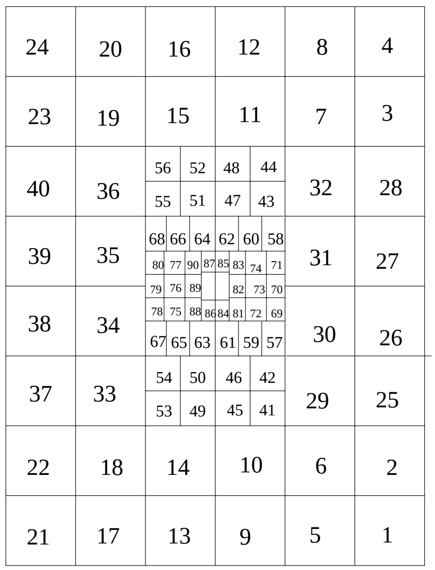

(a) C1. Cells 1–40 use spherical mirrors, 41–90 use planar mirrors.

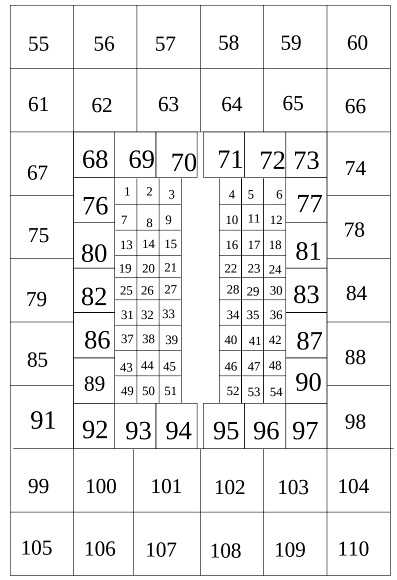

(b) C2. Cells 1–54 use planar mirrors, 55–110 use spherical mirrors.

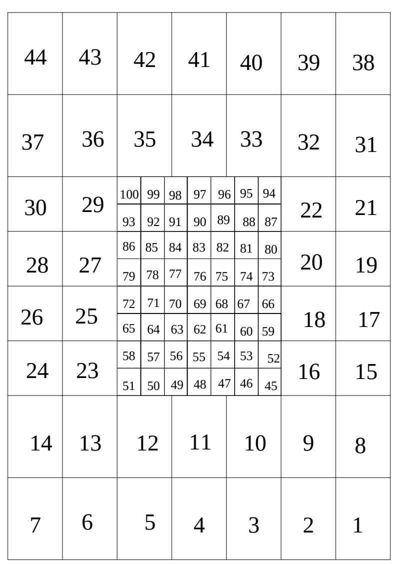

(c) C3. All cells use spherical mirrors.

Figure 3.7: The arrangement of the light gathering cells for the three Čerenkov counters, C1, C2, and C3.

C3: The Čerenkov detector C3 is the last and most downstream Čerenkov detector of FOCUS spectrometer and is located between P3 and P4. Its working area is 93.25"(vertical) x 60"(horizontal) and is filled with helium which gives a pion threshold of 17.0 GeV/c, and is divided in 100 cells. The light from each cell is focused with a spherical mirror onto a PMT. From the beam's eye view the cell arrangement of C3 is shown in Figure 3.7c.

Combining the information of the 3 Čerenkov detectors, it is possible to identify particles in the momentum ranges shown in Table 3.5.

Table 3.5: Particle identification momentum ranges for the Čerenkov system. Based on the Čerenkov threshold of each detector, the particle identification can be positive definite or ambiguous.

Definite Čerenkov ID range (GeV/c)				
	e	π	K	p
3-chamber	0.16–8.5	4.5–8.5	16.2–29.9	16.2–56.8
5-chamber	0.16–17.0	4.5–17.0	16.2–56.8	16.2–56.8 and 61.0–116.2

Ambiguous Čerenkov ID range (GeV/c)				
	e/π	$e/\pi/K$	K/p	π/K/p
3-chamber	8.5–29.9	29.9–56.8	4.5–16.2	0.16–4.5
5-chamber	17.0–61.0	61.0–116.2	4.5–16.2	0.16–4.5

3.7 Calorimetry

Calorimeters measure the energy of particles by destructive processes. In a calorimeter, particles interact with the material of the calorimeter and other particles are emitted. In electromagnetic interactions typical processes are bremsstrahlung ($e^- \rightarrow e^- + \gamma$) and pair conversion ($\gamma \rightarrow e^- + e^+$); while strong interactions produce hadron showers. In both cases the final number of charged particles is used to infer the energy deposited, since $n_{\text{particles}} \propto E_{\text{incident}}$.

Calorimeters are particularly important because neutral particles can be tracked in ionization devices.

The electromagnetic calorimeters were not used in this analysis. The hadronic calorimeter affects this analysis through the reconstruction of the decay $\Sigma^+ \rightarrow n\pi^+$ and due to its role in the triggering of the FOCUS spectrometer.

3.7.1 Outer Electromagnetic calorimeter

The Outer Electromagnetic calorimeter (OE) detects wide angle electromagnetic particles (γ and $e^{\pm}$) that pass outside the acceptance of M2. It is located just before M2. The OE is a sampling calorimeter with alternating layers of lead and plastic scintillator and consists of x, y, u, and v planes, (The u and v planes are oriented at $\pm 45°$ from horizontal) with an additional plane of 100 scintillator tiles. A full description can be found in Reference 33.

3.7.2 Inner Electromagnetic calorimeter

The Inner Electromagnetic calorimeter (IE) is located after P4 and is used to detect electromagnetic particles which pass through M2. The IE is composed of lead glass blocks. The long dimension of each block is oriented along the beam direction. The array is split in two sides with a gap in the central region to allow the passage of non-interacting photons and converted e^+e^- pairs. A full description can be found in Reference 34.

3.7.3 Hadron Calorimeter

The Hadron Calorimeter (HC) is located after the IE. The HC is constructed of alternating layers of steel and plastic scintillator tiles arranged in tower geometry. The dimensions of the HC are 2.08 m(horizontal)x 3.05 m(vertical) x 2.09 m (deep).

There are three transverse tile sizes small (20 cm square), medium (40 cm square) and large (50 cm square). The tile layers are arranged with the small tiles in the center and the larger tiles in the outer edges for a total of 66 tiles per layer. There are 28 layers of 4.4 cm thick steel (except the first two which are 6.4 and 5.1 cm thick respectively) which alternate with 28 layers of scintillator of 0.7 mm thick using fiber readout. The first nine layers are combined to form the towers in the first section, the next 15 layers form the second section, and the last 4 layers form the towers in the final section as shown in Figure 3.8. The scheme allows a small number of readout channels (192) and a measurement of the energy deposition as a function of depth in the three big sections. At the same time the fast response of the scintillator enables the HC to be part of the first level trigger (triggering hadronic final states). The HC is fully described in References 35 and 36.

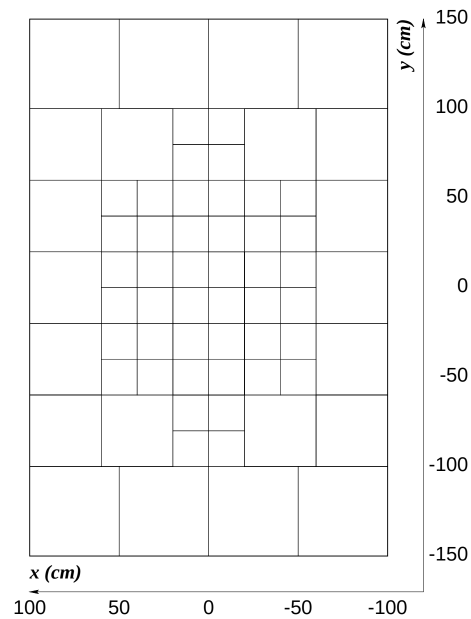

(a) Front view

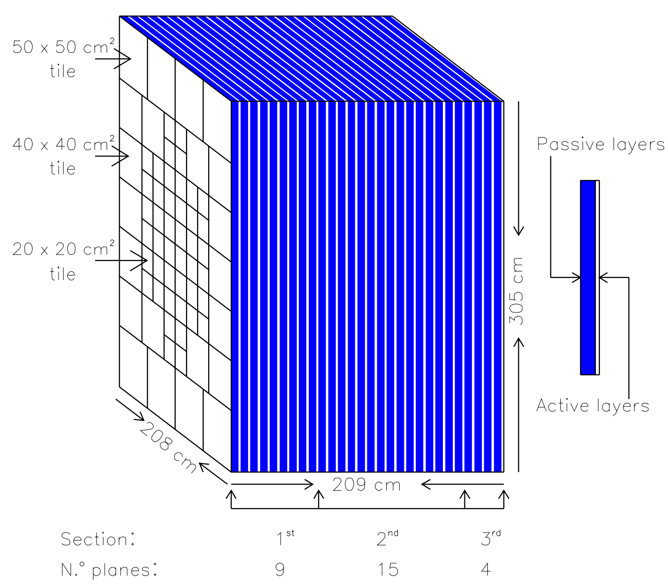

(b) Side view

Figure 3.8: Schematic views of the Hadron Calorimeter as seen by the beam and from the side.

3.8 Muon Detectors

The muon is the only charged particle which can penetrate a large amount of material because it doesn't lose much energy due to ionization and it doesn't interact strongly.

The FOCUS spectrometer has two muon systems. The inner muon system uses common scintillator detector elements, while the outer muon system uses resistive plate chambers to detect muons. A detailed description of these systems can be found in References 37 and 38. The muon detectors were not used in this analysis.

3.8.1 Outer Muon detector

The outer muon detector (OMU) is located behind the OE and outside the aperture of M2. Because of its location, the OE and the steel of M2 provide a filter to remove most of the hadronic contamination. The OMU detector uses Resistive Plate Chamber (RPCs) to identify wide angle muons. It is able to operate in large magnetic fields; which is important because there are substantial fringe fields in the region around M2.

There are 24 RPC modules which are arranged in 3 views x, y, and u (oriented at 45° respect to the horizontal). Each view is formed with 8 modules leaving an aperture (roughly matching the apertures of M2 and P3). The modules overlap slightly at the edges, as shown in Figure 3.9.

3.8.2 Inner Muon detector

The inner muon detector consists of three stations of scintillating hodoscopes labeled MH1, MH2, and MH3 and is located at the end of the spectrometer. In front of each station there is a wall of steel with thicknesses of 61 cm, 129 cm, and 68 cm respectively. Each station has two views. MH1 and MH2 have x and y views, while MH3 has u and v views oriented at $\pm 30°$ respect to the horizontal. A schematic view of the MH arrays are shown in Figure 3.10 and the numbers and sizes of counters are summarized in Table 3.6.

3.9 The Trigger

The electronic logic used to separate and select interesting events from uninteresting background is called the trigger. FOCUS typically had $\sim 100 \times 10^6$ (mostly elec-

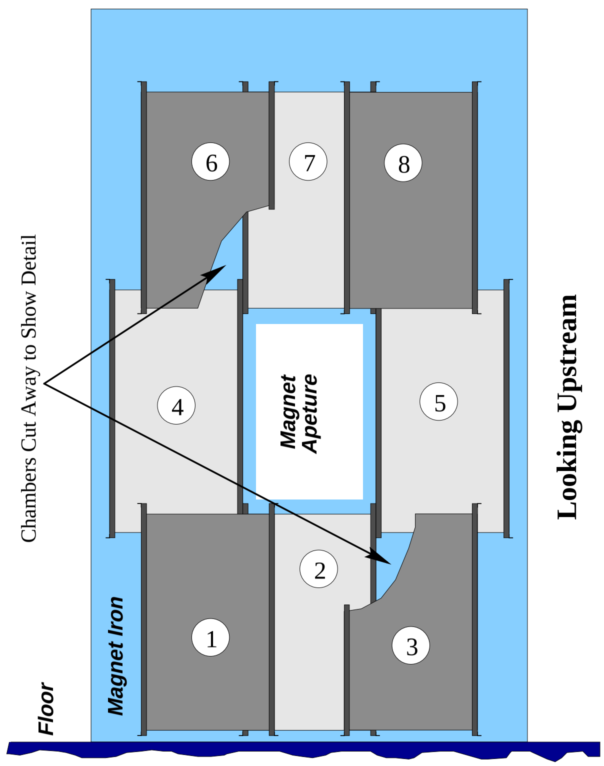

Figure 3.9: Schematic view OMU RPCs, showing one layer of 8 modules. There are three such layers.

Table 3.6: Summary of the MH array properties. X and Y apply to MH1 and MH2; U and V apply to MH3.

Station	Pitch	Number of counters		
		X/U	Y/V	Total
MH1	5 cm	84	126	210
MH2	8 cm	52	78	130
MH3	10 cm	54	54	108

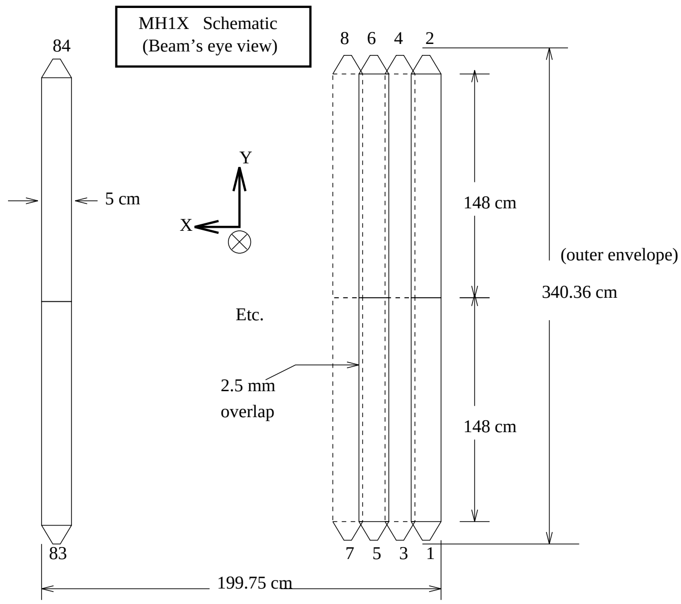

(a) MH1X. The arrangement of MH2X is similar.

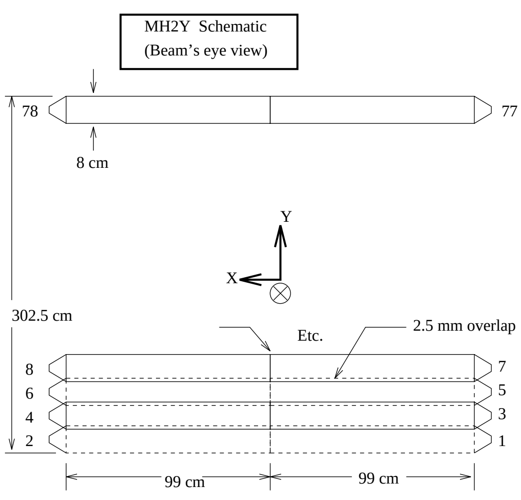

(b) MH2Y. The arrangement of MH1Y is similar.

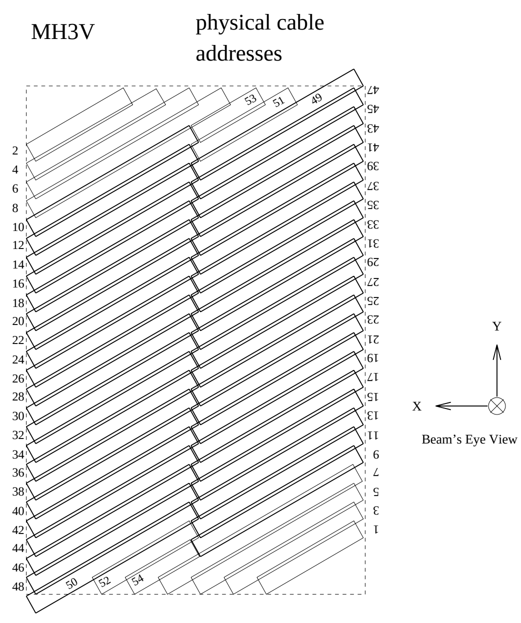

(c) MH3V. MH3U is identical except that the plane is rotated 180° around the Y view.

Figure 3.10: Views showing the counter arrangements of the Inner Muon Hodoscope arrays.

tromagnetic) interactions per spill and yet we only triggered on $\sim 30 \times 10^3$ (mostly hadronic) interactions per spill. To keep an event FOCUS uses a two level trigger. The first level trigger is called the "Master Gate" (MG). The MG decision is made within 200 ns of the beginning of the interaction. It takes 160 ns to transfer the information from the spectrometer, leaving about 40 ns in which to make this decision.

If the MG accepts the event, then the second level of the selection begins. This decision takes 1.2 μs and if the event passes the second level then the writing process to tape starts otherwise the electronics readout are cleared and reset. Resetting takes 1 μs.

3.9.1 First level trigger

The first level trigger checks for a interacting photon through the detection of charged particles coming from the target. To accomplish this task a number of scintillation counter triggers are used, combined with very fast logic circuits in addition to the detector triggers.

Some of the scintillator counters triggers used in the MG are:

TR1: Located between the last TSSD and the first SSD planes. Consists of a thin scintillator with a PMT readout which identifies if an interaction has occurred in the target. This counter is shown in the inset of Figure 3.1.

TR2: Located just downstream of the last SSD plane. Consists of four counters arranged in quadrants in which the four signals are discriminated and combined with a logical **OR**. A signal of this "counter" indicates a charged particle passed through the SSD and entered the aperture of M1. See inset of Figure 3.1.

H×V: Located between C3 and the IE. The H × V is an array of 36 counters as shown in Figure 3.11a. The array has a central gap to avoid detection of most e^+e^- pairs produced. The counter signals are combined to generate two output signals, $(\mathrm{H} \times \mathrm{V})_1$ and $(\mathrm{H} \times \mathrm{V})_2$ which indicate that at least one or two charged particles, respectively, have passed through the array.

OH: Located in front of the OE. The OH array has 24 counters arranged as shown in Figure 3.11b, with the aperture sized to match the M2 aperture and a gap in the center to avoid e^+e^- produced in the target. The OH_1 output signal is generated

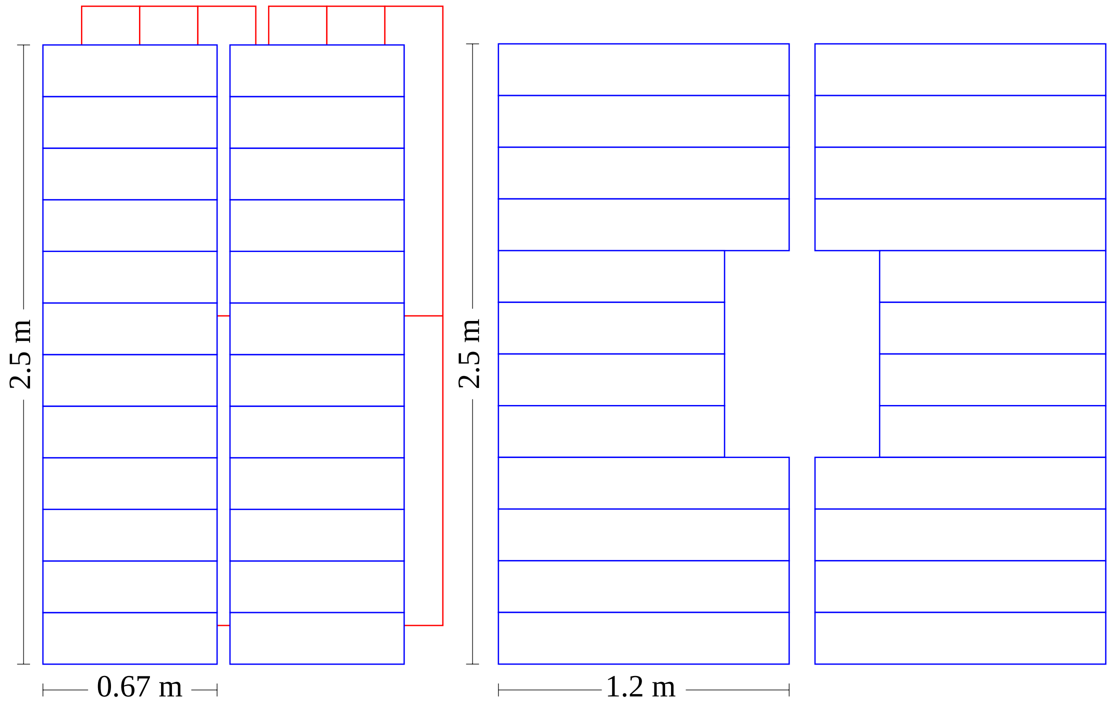

(a) H × V

(b) OH

Figure 3.11: The H × V and OH hodoscope arrays.

combining the signals in the OH array to indicate that at least one particle passed through this detector.

IM The counters used in the IM system are divided in three planes, the first two planes (IM1H and IM1V) located after MH2 and last plane located just before MH3. The counters are arranged as shown in figure Figure 3.12. The signal from the counters are combined to form the trigger of one or two muon signals with a consistency requirement of $(\mathrm{H} \times \mathrm{V})_1$ and $(\mathrm{H} \times \mathrm{V})_2$ signals and a veto of the muons not coming the experimental target.

AM & AMD: The muon veto signal is accomplished by the AM and AMD hodoscope arrays, which are two "walls" of scintillator upstream of the target surrounding the beam. A signal generated by the coincidence of the two arrays is an indication of charged particles coming to the spectrometer outside of the target region.

Other signals used in the MG are:

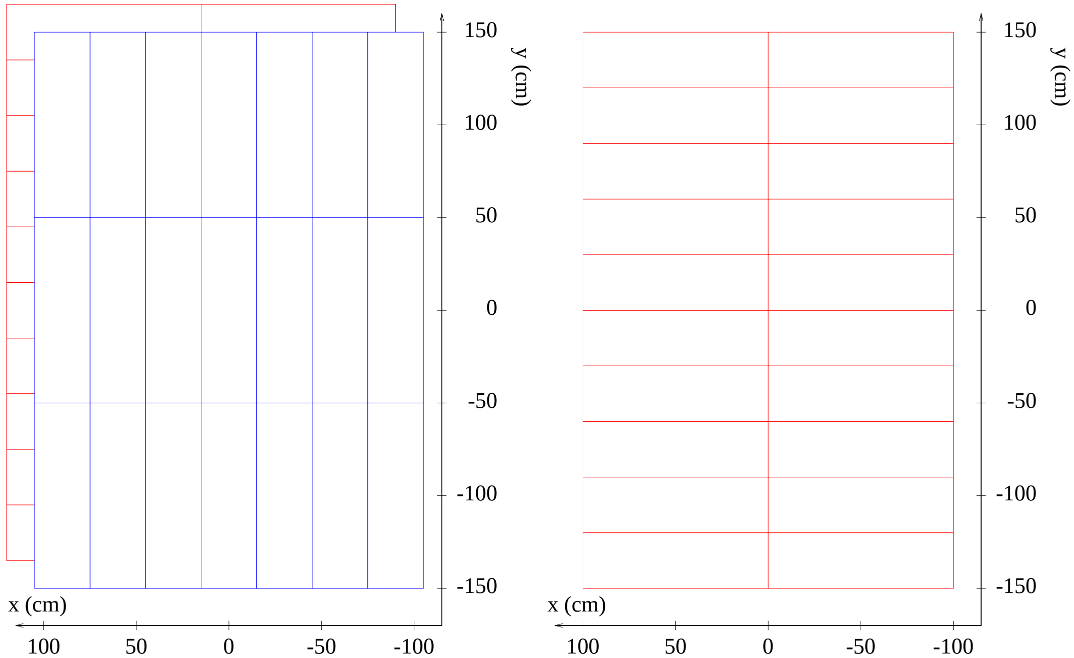

(a) IM1V and IM1H

(b) IM2H

Figure 3.12: The IM trigger counter arrays. a) shows the IM1V and IM1H arrays, b) shows the IM2H array. IM1H and IM2H are identically designed.

IE Based Triggers: The IE channels arranged in 9 groups are used as an input which is combined to form the different output signals. To select the decay $J/\psi \rightarrow e^+e^-$, the outputs are summed in six regions or sextants of the IE. The trigger requires 20GeV or more deposited energy in two non-adjacent sextants.

HC Energy Trigger The signals of PMT dynodes from the HC are summed, integrated and discriminated to form a hadronic energy trigger.

The OMU Trigger: From the 8 "towers" (the three views in each region) of the OMU detector, a signal is derived by requiring a hit in two of the three views. The OM_1 signal requires one tower and the OM_2 signal requires two non-adjacent towers.

In summary, the signals used to form Master Gates are:

TR1	Triggers on interactions in the target.
TR2	Triggers on particles downstream of SSD.
OH_1	At least one particle in the outer region.
$(\mathrm{H} \times \mathrm{V})_1$	At least one particle in the inner region.
$(\mathrm{H} \times \mathrm{V})_2$	At least two particles in the inner region.
E_{HI}	Hadronic energy over a high threshold.
E_{LO}	Hadronic energy over a lower threshold.
E_{IE}	Electromagnetic energy over the threshold.
IE_2	At least two hits in the IE.
IM_1	At least one hit in the IM counters.
IM_2	At least two hits in the IM counters.
OM_1	At least one hit in the OM array.
OM_2	At least two hits in the OM array.

Most of the physics triggers require two particles either both in the inner region or one in the inner region and one in the outer with opposite sides. The 2-body requirement is expressed as

$$2\mathrm{B} \equiv (\mathrm{H} \times \mathrm{V})_2 + [(\mathrm{H} \times \mathrm{V})_1 \cdot \mathrm{OH}_1] \tag{3.3}$$

where the standard algebra logic is used i.e. '+' is a logical **OR**, '$\cdot$' is a logical **AND**, and '!' is a logical **NOT**. With the combination of the 2-body plus the calorimeter triggers, FOCUS contructed seven MG shown in Table 3.7.

Table 3.7: The FOCUS Master Gates. Master Gates denoted (PS) are prescaled and are used for calibration.

Trigger	Definition	Physics signal
MG1	$\mathrm{TR1}\cdot\mathrm{TR2}\cdot2\mathrm{B}\cdot E_{\mathrm{HI}}$	Hadronic trigger
MG2	$\mathrm{TR1}\cdot\mathrm{TR2}\cdot2\mathrm{B}\cdot\mathrm{IE}_2$	$J/\psi \to e^+e^-$
MG3	$\mathrm{TR1}\cdot\mathrm{TR2}\cdot[\mathrm{IM}_1 + \mathrm{OM}_1] \cdot E_{\mathrm{LO}}$	Semi-muonic decays
MG4	$\mathrm{TR1}\cdot\mathrm{TR2}\cdot2\mathrm{B}\cdot[\mathrm{IM}_2 + \mathrm{OM}_2 + \mathrm{IM}_1 \cdot \mathrm{OM}_1]$	$J/\psi \to \mu^+\mu^-$
MG5	$\mathrm{TR1}\cdot\mathrm{TR2}$	e^+e^- pairs (PS)
MG6	$\mathrm{TR1}\cdot\mathrm{TR2}\cdot2\mathrm{B}$	Two-body events (PS)
MG7	$\mathrm{TR1}\cdot\mathrm{TR2}\cdot[\mathrm{IM}_1 + \mathrm{OM}_1]$	One-muon events (PS)

3.9.2 Second level trigger

Some information took "too long" to be in the MG, but was ready at the second level trigger; such as:

MULTn	Enough hits for at least n track(s) in PWC system.
AM·AMD	No halo muons.
IM(E+W)	Excludes hits in both halves of IM triggers.
$E_{\text{IE-2}}$	Better electromagnetic energy sum.

is used together with the MG to form the second trigger as listed in Table 3.8. Note that not all of the Master Gates generated (i.e., MG3 and MG7) were used for final triggering.

Table 3.8: A typical second level trigger set for FOCUS. The actual triggers changed occasionally, especially the di-muon triggers.

Trigger	Definition	Physics signal
TRIG1	MG1·$E_{\text{IE-2}}$·MULT4	Hadronic trigger
TRIG2	MG2·(H × V)$_2$ ·E_{IE}	$J/\psi \to e^+e^-$
TRIG4	MG4·IM$_2$ · (H × V)$_2$·!(AM·AMD)	J/ψ, inner only
TRIG5	MG5	Prescaled MG5
TRIG6	MG6	Prescaled MG6
TRIG8	MG1	Prescaled MG1
TRIG9	MG4·OH·OM$_2$·MULT2·!(AM·AMD)	J/ψ, outer only
TRIG11	MG4·IM$_1$·OM$_1$·MULT1·(H × V)$_1$ · IM(E+W)	J/ψ, inner/outer

3.10 Data Acquisition System

After an "interesting" interaction is triggered, the task of digitizing the analog signal from each detector to be recorded is acomplished by the Data AcQuisition system (DAQ). The FOCUS DAQ dealt with a number of different input data formats and merged all this data into one stream, and then put the output on 8 mm magnetic tapes. Figure 3.13 shows an overview of this process.

The FOCUS DAQ performance was outstanding during the run, logging 30–40,000 events per 20 second spill with a typical event size of ∼4kB. The livetime (the fraction of the time the DAQ spent waiting for the next event) was typically 85–90% with a readout time of about 35 μs. See Reference 39 for a complete description of the individual DAQ elements and a description of the whole system.

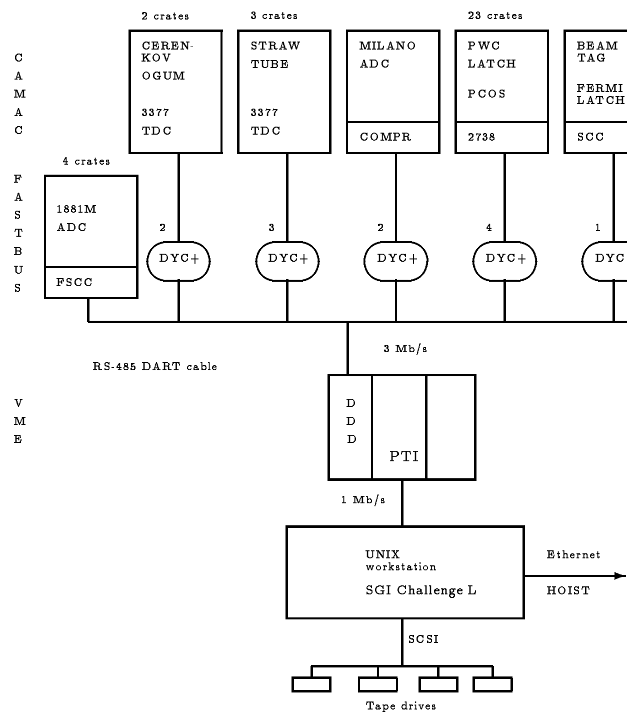

Figure 3.13: Structural overview of the DAQ, showing how the multiple sources are merged into one data stream and written to tape.

Chapter 4

Data Reconstruction

In this chapter a summary of the reconstruction algorithms and data processing used in FOCUS is presented. The topics include tracking reconstruction, vertexing, momentum determination, and particle identification algorithms. The process begins with the raw data written by the DAQ and ends with small data sets usable by an individual experimenter.

4.1 Track Reconstruction

The raw information gathered in the SSD and MWPC are first used independent of each other in separate reconstruction packages. Each process begins by combining the information in each station (SSD or MWPC) with information from other stations to create clusters of hits in views. This technique is called projection finding and it is applied to both SSD and MWPC track reconstruction. Later the independent track projections in each system are "linked" if they are consistent with a single charged particle. Each step is discussed in this section.

4.1.1 SSD tracking

The SSD track finding algorithm is performed in three stages. First the information from fired strips are grouped into "strip hits" using the ADC information; thus it is possible to determine if one or two close traversing particles created a single strip hit by comparing the total ADC counts to the number expected for a single Minimum Ionizing Particle (MIP).

Second, as momentum information is not yet available multiple Coulomb scattering effects are not considered. Projections are found in each view with at least three strip hits and sharing of hits is permitted, Hits found in four hit projections can not be reused in three hit projections. The projections are fitted to a straight line, with the requirement of a χ^2 per degree of freedom (χ^2/DOF) > 3.0.

Third, the projections are combined to form tracks by intersecting three projections (one for each view) keeping the combinations with $\chi^2/\mathrm{DOF} < 8.0$. In the case of tracks with shared projections, they are arbitrated based on the lowest χ^2/DOF in a symmetric way with respect to the views.

The hits, not associated with any track, are used to search for wide angle tracks and for segments of highly scattered tracks. This type of track is required to have at least six strip hits.

Finally, the pulse height information from all hits is combined to determine whether the track is consistent with the passage of a singly charged track.

In E687, the spatial resolution of a track in the high resolution region of the SSD was

$$\sigma_x = 11.0\ \mu\mathrm{m}\sqrt{1 + \left(\frac{17.5\ \mathrm{GeV}/c}{p}\right)^2} \tag{4.1}$$

$$\sigma_y = 7.7\ \mu\mathrm{m}\sqrt{1 + \left(\frac{25.0\ \mathrm{GeV}/c}{p}\right)^2}, \tag{4.2}$$

while the resolution of a track in the low resolution region of the SSD was about twice as large. In FOCUS, this resolution is slightly better because a pulse height sharing algorithm is being used. The constant term is due to the granularity of detector, while the momentum dependent term is due to the multiple Coulomb scattering contribution. The better resolution in y compared to x is because all three silicon planes provide y information, whereas only two of the three views contain information in x.

4.1.2 MWPC tracking

The MWPC tracks are reconstructed in a similar way to the SSD tracks, using a projection finding algorithm. The algorithm begins by reconstructing tracks which originate in P0 (the most upstream chamber), with the extrapolation of the x (non-bend) component of the SSD track through the spectrometer. A search is made for MWPC hits which match this "seed" projection. Also projections in the y,u, and v views are formed, then all projections are combined to form tracks. Next unused hits in x are taken to form additional projections and then matched with unused y,u, and

v projections reconstructing more tracks. Tracks are constructed with at least three chambers with no more than a total of four missing hits and at most two missing hits in a single chamber.

The next step is to perform a least squares fit on all track candidates. The fit parameters are intercepts and slopes of the track in x-z and y-z planes. For tracks passing through M2, the change in y slope due to the bend in the magnet is an extra parameter. Tracks which leave hits in all five PWCs are called "tracks" while those which leave hits in only the first three chambers are called "stubs"; the extra parameter in "tracks" is used to assign an approximate momentum to this class of tracks. A χ^2/DOF is applied to each track.

After determining the momentum of "tracks", various magnetic corrections are applied to account for the fringe fields in M1 and M2 extending beyond the magnet poles, and off-field components of the magnetic field (B_y and B_z) fit. Then the corrections are applied by refitting the "track" including the additional magnet effects in a iteration process, where the momentum is adjusted after each iteration.

A recovery algorithm is used to reconstruct track topologies missed by the above criteria. It works by extending the SSD tracks into the MWPC system to predict the x hits in P0,P1, and P2. Unused hits in y, u and v are used to form space hits in each chamber. Tracks reconstructed in this way are allowed to extend into P0, P0-P1 or P0-P1-P2, with a minimum requirement of three hits per chamber, except in the case of tracks which extend into P0 only where all four hits are required. Later the new tracks are least square fitted in order to determine the MWPC track parameters. This class of tracks is primarily comprised of very low momentum tracks which pass through M1 and bend out before passing through other chambers.

A few percent of the time wire chambers have a very large number of hits. Usually these events are too complicated to extract reasonable physics and they dramatically slow down the reconstruction process. To reduce the reconstruction time, a limit of 30 tracks is imposed on track finding. The limit is reached in roughly 3.5% of all events.

4.1.3 Linking

Once tracks are separately reconstructed in SSD and MWPC systems, they need to be connected with each other. This is called "linking".

Linking is performed by extrapolating both SSD and PWC tracks to the center of M1. The intercept and slope of the two types of tracks are required to be consistent with each other in the x (non-bend) view with a loose cut requirement allowing multiple MWPC tracks linked to the same SSD track. This condition prevents accidental elimination of correct choices. A global least squares fit using all hits from both systems is performed on each candidate. Multiple links are arbitrated based on the χ^2/DOF from the fit. A maximum of two MWPC tracks linked to the same SSD track are kept. This is done because e^+e^- pairs produced from photon conversions at the target often reconstruct as a single SSD track because there is almost no opening angle. The tracks separate in M1, bending in opposite directions.

The MWPC tracks which don't link, are later used in Vee (K_s^0 and Λ^0), Kink (Σ^+,Σ^-,Ξ^-,Ω^-) and Hyperon (Ξ^- and Ω^-) reconstruction.

4.2 Momentum determination

For the case of "tracks", the momentum is determined by the deflection angle in the magnetic field in M2. Similarly in the case of "stubs", the momentum is determined if tracks are linked using M1. Including the effects of the magnetic field which extends beyond the magnet, an iteration process is applied. Particle trajectories which enter the magnet at an angle or which have a lower momentum will transverse more field and require an excellent understanding of the tracing for a charged particle in the magnetic field. For vee reconstruction (see Section 4.5) where depending on where the decay happens, we need to know the exact amount of magnetic correction to be applied.

The problem is to propagate a particle of momentum $\vec{p}$ from the initial position $\vec{r_0} = (x_0, y_0, z_0)$ to the final position $\vec{r} = (x, y, z)$. From the Lorentz force in absence of a electric field we know the total momentum p is conserved and the trajectory can be traced in terms of the slopes ($\vec{r'} = d\vec{r}/dz$) in the x-z and y-z plane of the laboratory as follows:

$$\frac{\vec{r'}}{\sqrt{x'^2 + y'^2 + 1}} = \frac{\vec{r'}}{\sqrt{x'^2_0 + y'^2_0 + 1}} + \frac{q}{p\ c}\int_{z_0}^{z} \vec{r'} \times \vec{B}\ dz \tag{4.3}$$

where q is the charge of the particle in units of the electron's charge, and c is the speed of light; in practice $q = \pm 1$ and $c = 1$. For the case of tracks reconstructed and linked before and after the magnets, the initial and final slopes are known, the magnetic field is known, therefore the integral can be computed, and the equation is solved for signed p. As a good approximation, magnetic corrections outside the magnet are ignored and the magnetic field is only in the x direction, which gives the kick in y; x', y' can be neglected compared to unity, then

$$p = \frac{K}{y' - y'_0}, \quad \text{where} \quad K = \int_{z_0}^{z} B_x\ dz \tag{4.4}$$

This value is used to apply magnetic corrections to the tracks close to the magnets, then in a iteration process the corrected slopes are used to compute the momentum until changes from one iteration into another are small.

In the case of unlinked "stubs" there is no tracking information before they enter M1. To obtain an approximate momentum measurement of these particles, the vertex closest to the x projection of the track is chosen to trace through the magnetic field of M1, if no vertices are reconstructed, the center of the target is chosen.

The approximate momentum resolution for tracks whose momenta are determined by either M1 or M2 are given by:

$$\frac{\sigma_p}{p} = 0.034 \times \frac{p}{100 \text{ GeV}/c}\sqrt{1+\left(\frac{17 \text{ GeV}/c}{p}\right)^2} \quad \text{for M1} \qquad (4.5)$$

$$\frac{\sigma_p}{p} = 0.014 \times \frac{p}{100 \text{ GeV}/c}\sqrt{1+\left(\frac{23 \text{ GeV}/c}{p}\right)^2} \quad \text{for M2} \qquad (4.6)$$

As in the case of the SSD resolution, the momentum resolution at low momentum is dominated by multiple Coulomb scattering represented by the second term in the square root, but at high momentum the resolution is limited by the position resolution in the MWPC system.

4.3 Čerenkov particle identification

Čerenkov identification is used to identify the particle type of each charged track where momentum information is available.

The algorithm used by FOCUS is referred by the acronym CITADL [40] for Čerenkov Identification of Tracks by an Algorithm using Digital Likelihood. This algorithm was motivated by the desire to produce a more flexible Čerenkov identification algorithm than that used in E687 [27]. Rather than making a hard decision, on whether or not a track was consistent with a given hypothesis, CITADL computes relative likelihoods that the track has a Čerenkov pattern similar to that for the $e^\pm$, $\pi^\pm$, $K^\pm$, and $p/\overline{p}$[1] hypothesis. For each of these four hypotheses the likelihood, is calculated by observing the on-off status of the cells within the Čerenkov cone of the particle with a cell's firing probability given by the Poisson probability (1 - exp(-μ)) where μ is the expected number of Čerenkov photons striking the cell under each particle hypothesis of a track

[1] The $\mu^\pm$ hypothesis is not considered separately from the $\pi^\pm$ since the momentum range over which the two hypotheses can be separated is limited.

with known momenta. An accidental firing rate is also included in this calculation to model spurious hits; this cell-by-cell correction factor depends on the beam intensity on an event-by-event basis. The accidental firing rates are typically less than 1% except for cells close to the uninteracting beam.

The product of the firing probabilities for all cells within the track's $\beta = 1$ Čerenkov cone in the three detectors is the probability for each hypothesis given a track. If a cell overlaps more than one track's Čerenkov cone, then it is excluded from the product. CITADL returns its identification in the form of χ^2-like variables for the different particle hypotheses (W_e, W_π, W_K, W_p). They are defined by $W_i = -2\sum logP_i$ where P_i is the probability for the observed outcome (on or off[2]) for that cell under each of the four particle hypotheses. For example we define $\Delta W_K = W_\pi - W_K$ ("kaonicity") for use in identifying kaons by requiring the "kaonicity" to pass a minimal cut. For example $\Delta W_K > 2$ means we are separating the kaons from pions by at least 2 units of log likelihood.

The advantage of this method in identifying particles is the discrimination between two hypotheses can be extended beyond the threshold momentum ranges. Using the likelihood approach, the Čerenkov cuts can be more carefully selected and tuned for a particular physics analysis since there is a continuous value to cut on rather than a simple on/off value for each particle hypothesis.

4.4 Basic Vertexing

As described in the previous section, the unlinked "stubs" require vertex information. To accomplish the task, a basic vertex algorithm is implemented in the early stages using only the SSD information. Also these vertices are used in the reconstruction of the different vee (see Section 4.5) categories and are meant to be only roughly correct. Later in the analysis all available tracking and momentum information is used in the vertexing method (see Section 5.1).

The basic vertex algorithm minimizes the distance of closest approach of the tracks in the transverse plane, by minimizing the $\chi^2(x, y, z)$ of the form:

$$\chi^2 = \sum_{i=1}^{n} \left(\frac{x - (x_i + x_i' z)}{\sigma_{x,i}} \right)^2 + \left(\frac{y - (y_i + y_i' z)}{\sigma_{y,i}} \right)^2 , \tag{4.7}$$

where (x, y, z) are the coordinates of the vertex; x_i, y_i, x_i', and y_i' are the SSD track parameters; and $\sigma_{x,i}$ and $\sigma_{y,i}$ are the errors on the SSD tracks. The index i sums over the tracks in the vertex.

[2]For this reason it is called a "digital" likelihood

The algorithm begins by assigning all the SSD tracks to a common vertex and computing a χ^2/DOF. The track with the largest contribution to the χ^2 is removed if the $\chi^2/\mathrm{DOF} > 3.0$. Each iteration the vertex is refit and the substraction process repeated until $\chi^2/\mathrm{DOF} < 3.0$. Later all tracks discarded from the vertex are individually tested to check if they match with the first vertex. Once the first vertex is completed, the procedure is repeated with the remaining set of tracks, until all tracks are assigned to just one vertex or remain unassigned.

For the vee reconstruction the most upstream vertex within the target is called the primary vertex. If primary vertex is not found, then the center of the target is used as the primary vertex.

4.5 Vees (Λ^0 and K_s^0) reconstruction

The neutral particles Λ^0 and K_s^0 usually are called vees because they are reconstructed using two charged tracks with opposite sign which makes a vertex as shown in Figure 4.1. FOCUS reconstructs these particles through the decay modes $K_s^0 \rightarrow \pi^+\pi^-$ (BR = 68.6%) and $\Lambda^0 \rightarrow p\pi^-$ (BR = 63.9 %).

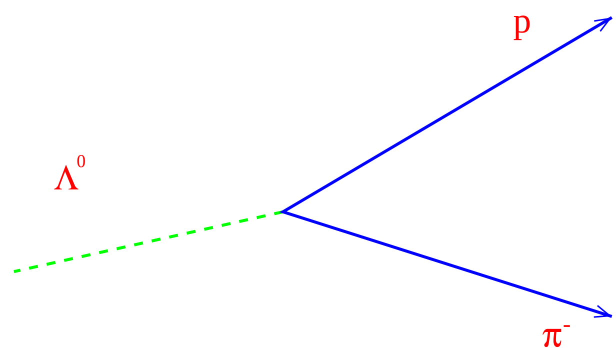

Figure 4.1: Illustration of the vee topology for the decay $\Lambda^0 \rightarrow p\pi^-$. The dotted line denotes the neutral, unseen particle, solid lines represent the two charged prongs. The decay $K_s^0 \rightarrow \pi^+\pi^-$ is identical except the prongs are both pions.

Vees are relatively long-lived particles compared to charmed particles, and typically, they travel several meters in the spectrometer before decaying. Because of the large region in z, there are many decay topologies, which in practice means different vee-finding algorithms. The algorithms have in common the search for a pair of oppositely charged tracks forming a vertex. The invariant mass of the pair is computed under two hypotheses, the pion mass is assigned to both tracks to test for a K_s^0 mass, and the proton mass is assigned to the higher momentum track and the pion mass to the lower momentum track to test for a Λ^0 mass. No particle identification is used at this

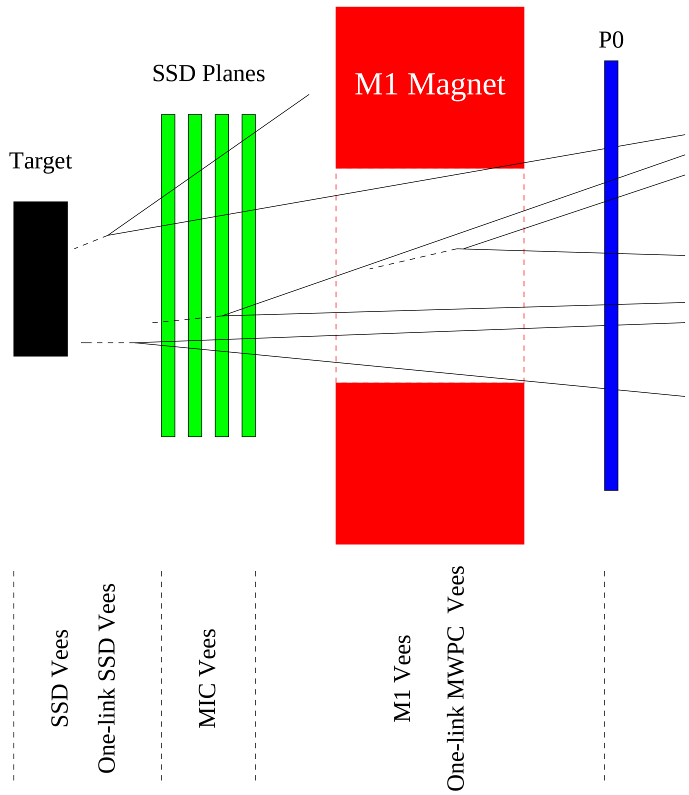

Figure 4.2: Spectrometer regions and Vee reconstruction algorithms. This diagram of the upstream portion of the spectrometer is simplified and not to scale.

stage, and the vee requirements are intentionally left loose to allow different degrees of signal to noise in individual analyses.

In FOCUS, vees are reconstructed in three regions: the target region, the SSD region and the region between the SSD and the first MWPC chamber (P0). Figure 4.2 shows the regions where different algorithms are used. Other algorithms were developed for the regions beyond P0, but were not used in FOCUS, because the high intensity beam led to increased noise in the chambers which made the rate of false vees high and the algorithm less efficient.

4.5.1 SSD vees

The SSD vees are reconstructed using linked SSD-MWPC tracks, originating from a common vertex. Because the tracks have momentum information, the vertex is formed with two SSD tracks in the same manner as charm decays are reconstructed. The new vertex is required to lie downstream of the primary vertex with a three sigma separation of two vertices. As the decays occur close to the primary vertex, this type of vees tends to be lower momentum and has excellent mass resolution because of the full SSD information.

4.5.2 M1 vees

The M1 vees are the most copious category, accounting for over 70% of all decays, and they consist of K_s^0 and Λ^0 which decay between the last SSD and the first MWPC station. They are reconstructed with pairs of unlinked MWPC tracks and are divided in three categories, Track-Track, Track-Stub, and Stub-Stub vees based on the track type.

From equation 4.3 the approximate solution for the predicted slopes as function of the original slopes and the magnetic field transverse for a particle is given by:

$$\begin{aligned} x' &= x'_0 \\ y' &= y'_0 + \frac{1+y'^2_0}{p}\sqrt{x'^2_0 + y'^2_0 + 1}\int_{z_0}^{z} B_x \, dz \end{aligned} \tag{4.8}$$

The algorithm starts by intersecting the pair candidates in the x-z plane, to find a rough position in z of the vertex. The z location is used as the starting point of a iteration process that traces the two prongs through the M1 field and determines the y location of the vee vertex. In the case of the Track-Stub, the location from tracing the Track is used to compute the momentum and charge of the Stub. For the case of Stub-Stub is necessary to use a further constraint that the vee vector originate from the primary vertex, in order to compute the momentum of each prong. In the iteration process a global fit is applied to each vee candidate. The global fit uses the full covariance matrices of the tracks, including multiple Coulomb scattering effects to provide a better estimate of the vee decay vertex and vee momentum.

The mass and vertex resolutions are not as good as for the SSD vees and are a very strong function of the angle the vee plane makes with the M1 field. The resultant mass distributions often have very non-Gaussian tails. To correct for this effect, vees are retained based on a normalized mass cut or on the difference between the reconstructed and nominal vee mass divided by the anticipated resolution. The normalized mass distribution is much closer to a true Gaussian distribution. The selection criteria for the K_s^0 M1 vees is that the absolute value of the normalized mass be less than 5. For the case of Λ^0 a simple mass cut is applied to allow for the possibility of Ξ^- and Ω^- reconstruction.

4.5.3 One-link SSD vees

This category requires an unlinked SSD track and a linked SSD track. The vee is required to decay before the second SSD station for which one of the decay prongs falls out of the M1 geometrical acceptance and therefore is not found in the MWPC system.

Both tracks are required to form a good vertex. The separation of the vee vertex and the primary is required to be at least 10 sigma separation. The primary vertex must also be upstream of the vee vertex. Also the vector formed by the primary-vee vertices must lie in the plane of the two decay prongs. This constraint makes it possible to compute the momentum of the unlinked track when the transverse momentum is balanced and removes the two-fold ambiguity in the kinematics. For the invariant mass of the Λ^0 hypothesis the linked track is required to have the proton mass.

4.5.4 MIC vees

MIC vees have the decay vertex between the second and last SSD station. The reconstruction algorithm starts by projecting unlinked MWPC tracks backward onto the SSD detector and by searching for unused hits in the last two stations. If one or more triplets of hits in each station are found, then the parameters of the track are recomputed using a global fit with SSD and MWPC hits combined. The new reconstructed tracks are then checked two at the time to see if the form a vertex and a cut on the distance of closest approach (DCA) is imposed. Candidate vees sharing one prong are arbitrated on the basis of a minimum DCA.

4.5.5 Single-linked MWPC vees

This category of vees is topologically identical to M1 vees, but are composed of one linked SSD-MWPC track and one unlinked MWPC track. The reconstruction algorithm is essentially the same as for M1 vees, with three categories: Track-Track, Track-Stub, and Stub- Stub. For K_s^0 reconstruction there was too much background in these categories and they were not used. However, for the Λ^0 these categories were very important particularly when the Λ^0 was a decay product of a Ξ^- or Ω^-.

4.5.6 Arbitration of vees

In case of high multiplicity events it is possible for a track to be part of more than one vee candidate. The vee candidates are arbitrated so that a single MWPC track is used just once in forming a vee. When a track is shared by more than one vee , the decision to keep a vee is made with the following criteria.

- Two SSD vees sharing a SSD track are arbitrated based on which vee has the smaller distance of closest approach at the decay vertex location.
- Two M1 Track-Track vees sharing a MWPC track are arbitrated based on which vee has the smaller DCA at the decay vertex location.
- Two M1 Track-Stub (Stub-Stub) vees sharing a MWPC track are arbitrated based on which vee has the smaller χ^2/DOF of the fit
- M1 Track-Track vees are always selected over M1 Track-Stub vees.
- M1 Track-Stub vees are always selected over M1 Stub-Stub vees.

Using approximately 0.5% of the total of the data, six histograms of the K_s^0 vees are presented in Figure 4.3 and nine histograms of the Λ^0 vees in Figure 4.4. In both cases the SSD vees have the best mass resolution, but with considerable background due to the decay being located close to the interaction region. The One-link SSD vees are less clean than the SSD vees due to the very low momentum. The MIC vees are the cleanest sample but the yield is comparatively low. The M1 vees account for the 70% of the total vees. For the Λ^0 decays it is useful to retain the Single-linked MWPC vees, since Ξ^-'s and Ω^-'s decay to Λ^0 and occasionally the proton of the Λ^0 decay is erroneously linked with the Ξ^- or Ω^- track segment in the SSD. At the skim level a soft particle identification is applied to the proton of the Λ^0 decay.

4.6 Kink (Σ^- and Σ^+) reconstruction

The "Kink" term refers to the topology where one charged particle decays to another charged particle and a neutral particle. The neutral particle is undetected in the tracking detectors.

A schematic of a kink decay is given in Figure 4.5. The parent particle with measured direction cosines, (α, β, γ) in the SSD system with a mass m_{Σ^-}, decays to particles π^- and n. Particle π^- is traced back to the parent decay where the measured direction cosines are (a, b, c) and its momentum is measured in M1 (p_1). Particle n is neutral and goes undetected in the spectrometer. Through kinematic constraints and by

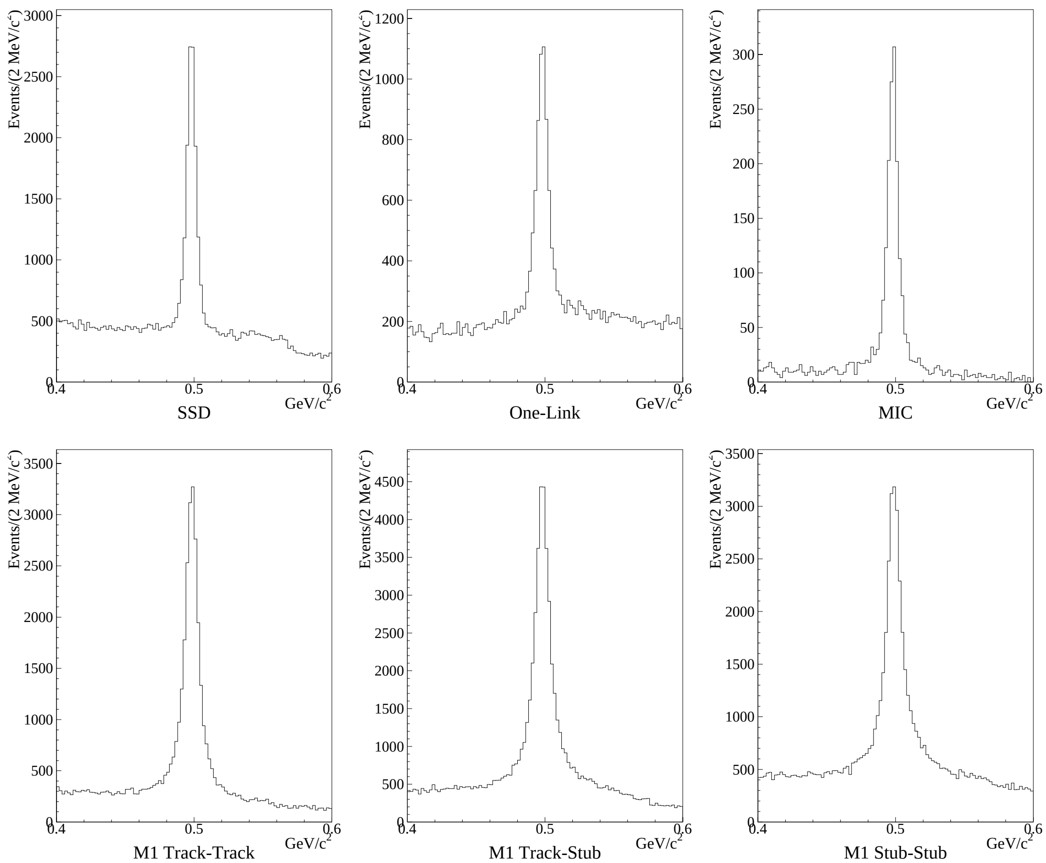

Figure 4.3: Histograms of a sample of six categories of K_s^0's which are used in the analysis. The dominant categories in charm decays are the (*M1 track-track*) and (*M1 track-stub*) Vees. The categories with the best resolution are *MIC*, *SSD*, and *One-link* Vees.

assuming the parent mass, the parent momentum (P) is calculated to within a twofold ambiguity.

The n mass is an invariant given by:

$$m_n^2 = E_n^2 - p_n^2 \tag{4.9}$$

but from the energy-momentum conservation ($E_n = E - E_1$ and $\vec{p_n} = \vec{P} - \vec{p_1}$) we substitute in equation 4.9 to obtain

$$(m_{\Sigma^-}^2 + m_{\pi^-}^2 - m_n^2) + 2Pp_1(\alpha a + \beta b + \gamma c) = 2EE_1 \tag{4.10}$$

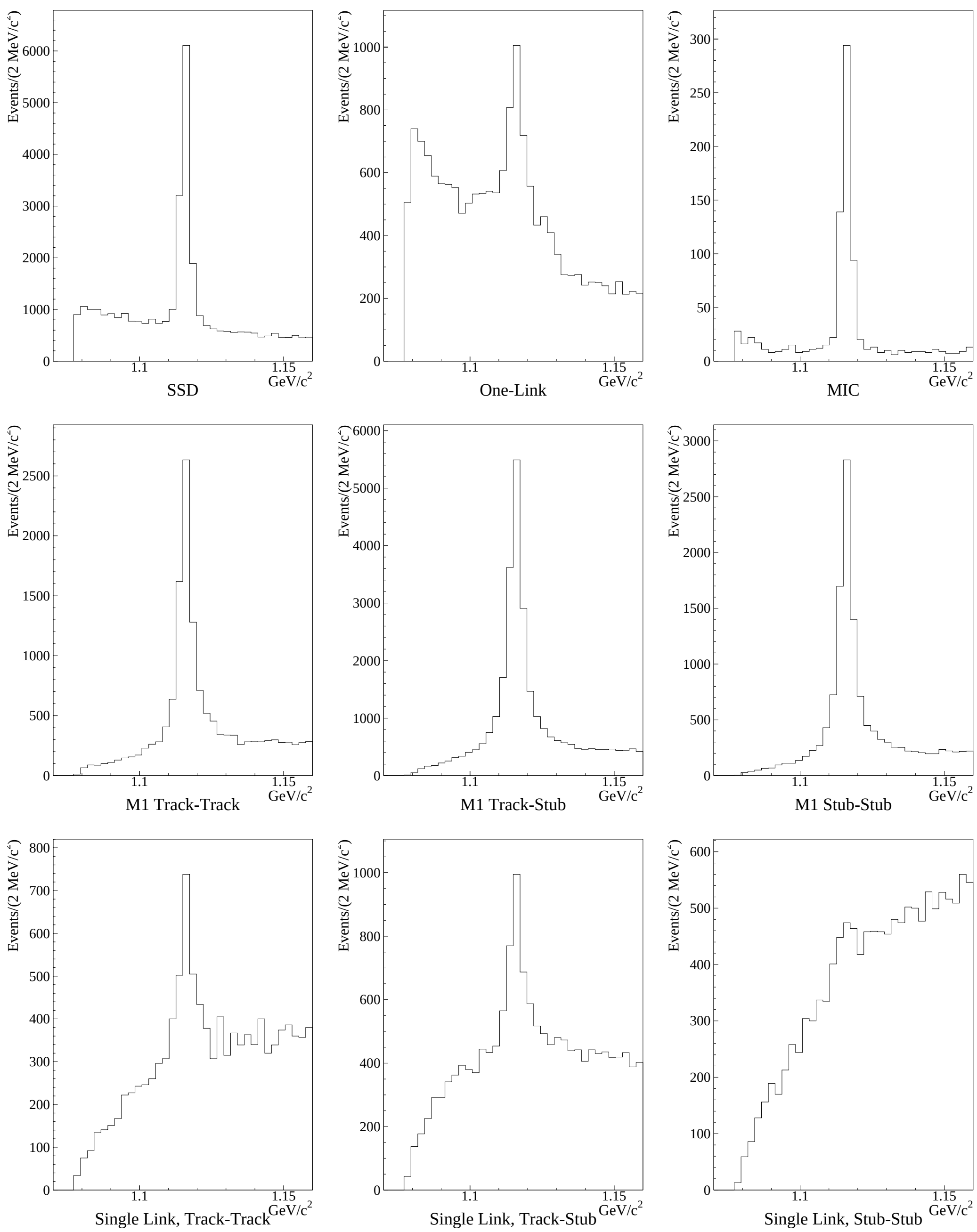

Figure 4.4: Histograms of a sample of nine categories of Λ^0's which are used in the analysis. The final row of Single-linked Λ^0's are not used in charm analyses involving direct charm decays to Λ^0's, but account for almost 15% of the Ξ^-'s and Ω^-'s decays.

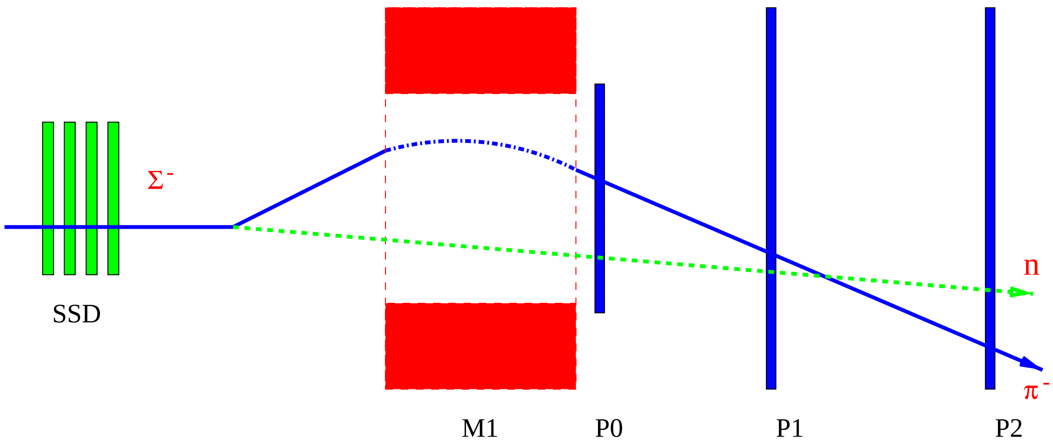

Figure 4.5: Sketch of a kink decay process for the decay Σ^-. The dotted line denotes the neutral, unseen particle.

Squaring this equation, substituting $E^2 = P^2 + m^2_{\Sigma^-}$, and solving for P, we find

$$P = \frac{MC \pm \sqrt{M^2C^2 - (1 - C^2)(m^2_{\Sigma^-} - M^2)}}{(1 - C^2)} \tag{4.11}$$

where $M = \frac{m^2_{\Sigma^-} + m^2_{\pi^-} - m^2_{n}}{2E_1}$, $C = \frac{p1(\alpha a + \beta b + \gamma c)}{E1}$, and P >0. Thus, we find the twofold ambiguity.

Initially the "kink" algorithm is used to reconstruct the three decays $\Sigma^+ \to p\pi^0$, $\Sigma^+ \to n\pi^+$, and $\Sigma^- \to n\pi^-$. It should be noted that the $\Sigma^+(suu)$ and the $\Sigma^-(sdd)$ are *not* charge conjugate partners and that the 8 MeV/c^2 difference in their masses is important to include in the algorithm. The Σ^+ decays weakly to $p\pi^0$ 51.6% of the time and to $n\pi^+$ 48.3%. The Σ^- decays to $n\pi^-$ essentially 100% of the time. Later the algorithm was used to reconstruct hyperons, Ξ^- s and Ω^- s, through the decays $\Xi^- \to \Lambda^0\pi^-$ and $\Omega^- \to \Lambda^0 K^-$ were the Λ^0 is missing, these decays will be further considered in Section 4.7.4.

Kinks are reconstructed by looping over unlinked SSD tracks (presumably the Σ) which point into the M1 aperture and by pairing them with every unlinked MWPC track that also point into the M1 aperture. MWPC tracks used in vees are not considered. A initial kink z vertex location is determined by intersecting the SSD and MWPC in the x-z plane. The z location is required to be downstream of the last SSD station and upstream of P0.

If the initial z vertex location is upstream of M1, then the SSD track does not suffer any deflection, and the vertex position is along the line of the SSD track. Using the SSD tracks parameters, the vertex location is computed at the initial z, and in a iteration process the z vertex location is improved using both views when the MWPC and SSD are intersected. In case of a 5-chamber track, its momentum is already determined from M2 and it is possible to trace through the field of M1 to the estimated kink vertex, otherwise the MWPC track is a 3-chamber track and its momentum is computed using the previous kink vertex location. The x and y distance between the projected MWPC track and the SSD track is compared and required to be less than 2.5 mm, this helps to eliminate spurious kink candidates. The parent momentum is computed by making a particular decay hypothesis and by solving the kinematic equations (equation 4.11), this process involves assuming the parent ($\Sigma^{\pm}$) and daughter masses (including the missing neutral daughter) and balancing the momentum transverse to the parent direction. The result is a twofold ambiguity in the parent momentum.

If the initial kink z position is within M1, the ambiguity can be broken and a unique solution is found. Only 5-chamber MWPC tracks are used because tracing through M1 field is possible due the known momentum. The x and y coordinates of the kink vertex are given by the traced position of the MWPC track to this z. The SSD track is then traced downstream through M1 to the kink vertex. The trace is iterated several times, using trial momenta, until a momentum is found which best traces the the SSD track to the kink vertex. The transverse momentum is balanced and the kinematic equation are solved. If there are two physical solutions for the parent momentum, then the one nearest to the momentum calculated by the iterative trace is used. In theory, one could avoid solving the Kink kinematic equations for decays in the magnetic field by simply using the microstrip trace momentum, however often very little magnetic field is traced through and the resolution on the microstrip track curvature (momentum) is not well defined. For these reasons the kinematic solutions were always used to determine the momentum.

In order to reject topological backgrounds, particle identification is made on the charged daughter or on the basis of the calorimetry information. The charged particle identification is made by re-running the Čerenkov code with the momentum determined from the kink reconstruction in order to obtain a new Čerenkov identification estimate (*i.e.* the momentum changes). For the $\Sigma^+ \to p\pi^0$ hypothesis the Čerenkov light pattern is required to be more consistent with a proton assumption than the pion assumption by at least four units of log likelihood ($\Delta W_P \equiv W_\pi - W_P > 4$). For the $\Sigma^+ \to n\pi^+$ and $\Sigma^- \to n\pi^-$ hypotheses the pion is required to not be consistent with being an electron, kaon, or proton and the neutron must impact the hadron calorimeter. The neutron must deposit sufficient energy, E, surrounding the point where the neutron is expected to strike the calorimeters and must satisfy $0.3 < \mathrm{E/p} < 2.0$, where p is the momentum of the neutron calculated from the kink kinematic equations.

4.7 Cascade (Ξ^- and Ω^-) reconstruction

With the "cascade" reconstruction algorithms, we are able to reconstruct the decays $\Xi^- \to \Lambda^0\pi^-$ and $\Omega^- \to \Lambda^0 K^-$. The Ξ^- decays to $\Lambda^0\pi^-$ essentially 100% of the time, while the Ω^- decays weakly to $\Lambda^0 K^-$ 67.8% of the times.

The Ξ^- and Ω^- decays are reconstructed via several techniques. Initially two topologies were considered. The first topology referred as "Type 1" consists of fully reconstruct Ξ^-'s and Ω^-'s decaying upstream of the SSD system. The second topology referred as "Type 2", where the decay occurs downstream the SSD system is reconstructed differently than the previous one. Later two more topologies were added, in both cases as in Type 2 the cascade decay occurs downstream of the SSD system, in one case the vee decays quickly and there is no resolution to separate the production and decay vertex of the vee then we use a technique referred to as "Multivees" where there are three unlinked MWPC tracks, in the other case is we use the kink algorithm to find $\Xi^-(\Omega^-) \to \Lambda^0\pi^-(K^-)$ where the Λ^0 is not reconstructed. The kink algorithm is needed to reconstruct the cascade either when one leg of the vee goes out of acceptance or when $\Lambda^0 \to n\pi^0$. Each of these techniques will be described below.

With the exception of the cascade kink reconstruction, all algorithms fully reconstruct the cascades. For those cases, a common set of requirements are used to select vees as Λ^0's. The vee daughter track with the highest momentum is considered the proton for the Λ^0 hypothesis and Čerenkov particle identification is applied to the proton using the momenta of the vee track as determined by the vee algorithm, requiring $\Delta W_p > 4$.

4.7.1 Upstream reconstructed cascades

The upstream cascades decays or Type 1 cascades are those which decay within the target or between the target and the SSD system. A schematic of a typical cascade decay in this category is presented in Figure 4.6.

The algorithm starts by pairing linked MWPC tracks with each Λ^0 vee which satisfy the Λ^0 hypothesis. Upstream decays are reconstructed by intersecting the Λ^0 vector and the MWPC track. When the vee has SSD information the vertex is well defined and we demand a confidence level of this vertex be greater than 1% and that the cascade be consistent with originating from a production vertex. When Λ^0 is a M1 vee (no SSD information) then the cascade vector and the SSD component of the linked track form a plane which is intersected by the plane formed with the production vertex and the linked track. The intersection of both planes gives the location of the cascade decay vertex, which is required to lie downstream the production vertex. At

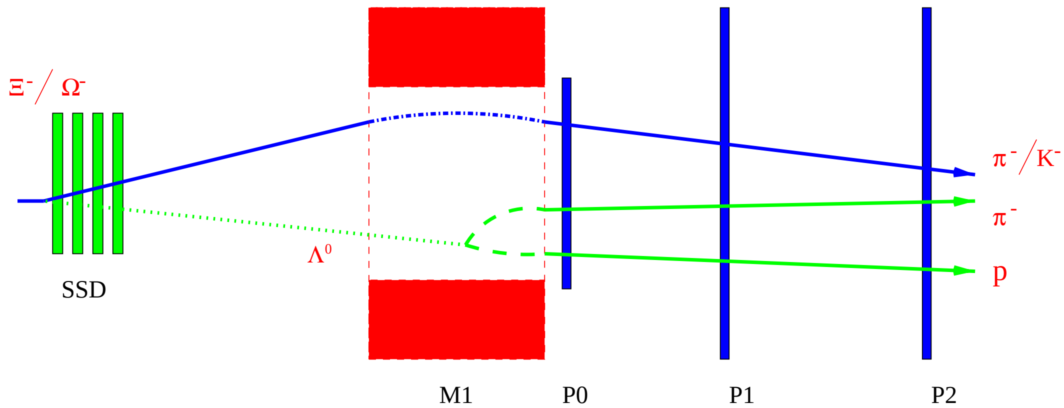

Figure 4.6: Schematic of a cascade decay upstream the SSD system.

the time of processing the data, one-link ssd vees were considered without the use of ssd information.

At the skim level a very loose cut was imposed in the *significance of separation* of the cascade vertex from its production vertex, defined as L/σ_L; where L is separation in both vertices and σ_L is the uncertainty on L. By increasing the cut on L/σ_L (i.e. $L/\sigma_L > 1, 2, 3,$ etc.) one obtains a cleaner sample. In Figure 4.7 and Figure 4.8 are shown plots of the Ξ^- and Ω^- reconstructed upstream of the SSD system for the different vees reconstruction. The black continuous histograms are the signal for the basic algorithm which requires $L/\sigma_L >0$. The red dotted histograms are the cleaner sample which requires $L/\sigma_L >5$.

Notice the peak around 1.29 GeV$/c^2$ for the $\Lambda^0\pi^-$ combinations where the Λ^0 is a SSD vee or one-link SSD. In both cases the peak comes from switching the pion from the Λ^0 with the pion from the Ξ^-. The peak is not present in $\Lambda^0 K^-$ combinations because the particle identification of $\Delta W_K > 2$ imposed on the Ω^- daughter.

Over 80% of the cascade signal is reconstructed using the M1 vees; the contribution of mic vees to the final cascade sample is tiny even the good signal on $\Lambda^0\pi^-$ (less than 1%.). SSD and one-link vees have a contribution to the Ξ^- sample only, but in SSD case the background is high and in the one-link case the contribution to the total is a few percent.

All Λ^0 combinations are used to form Ξ^- and Ω^-. The full data sample of FOCUS is shown in Figure 4.9. Most of the background under the Ω^- signal is due to pion particle misidentification from $\Xi^- \rightarrow \Lambda^0\pi^-$ decays. One should note also that Ω^- yield is about a factor 20 less than the Ξ^- yield.

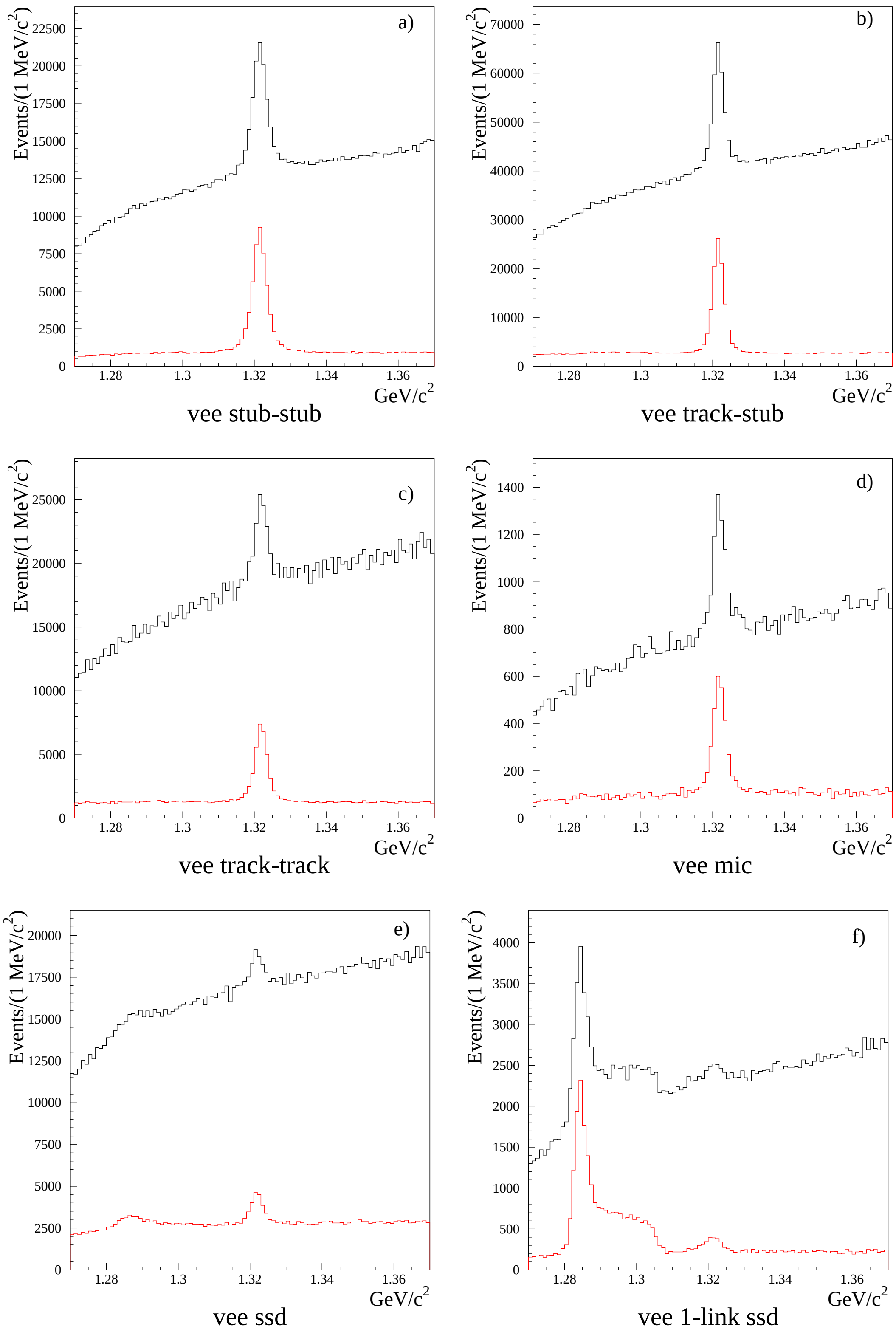

Figure 4.7: Invariant mass for the $\Lambda^0\pi^-$ combinations type 1 for different vee categories

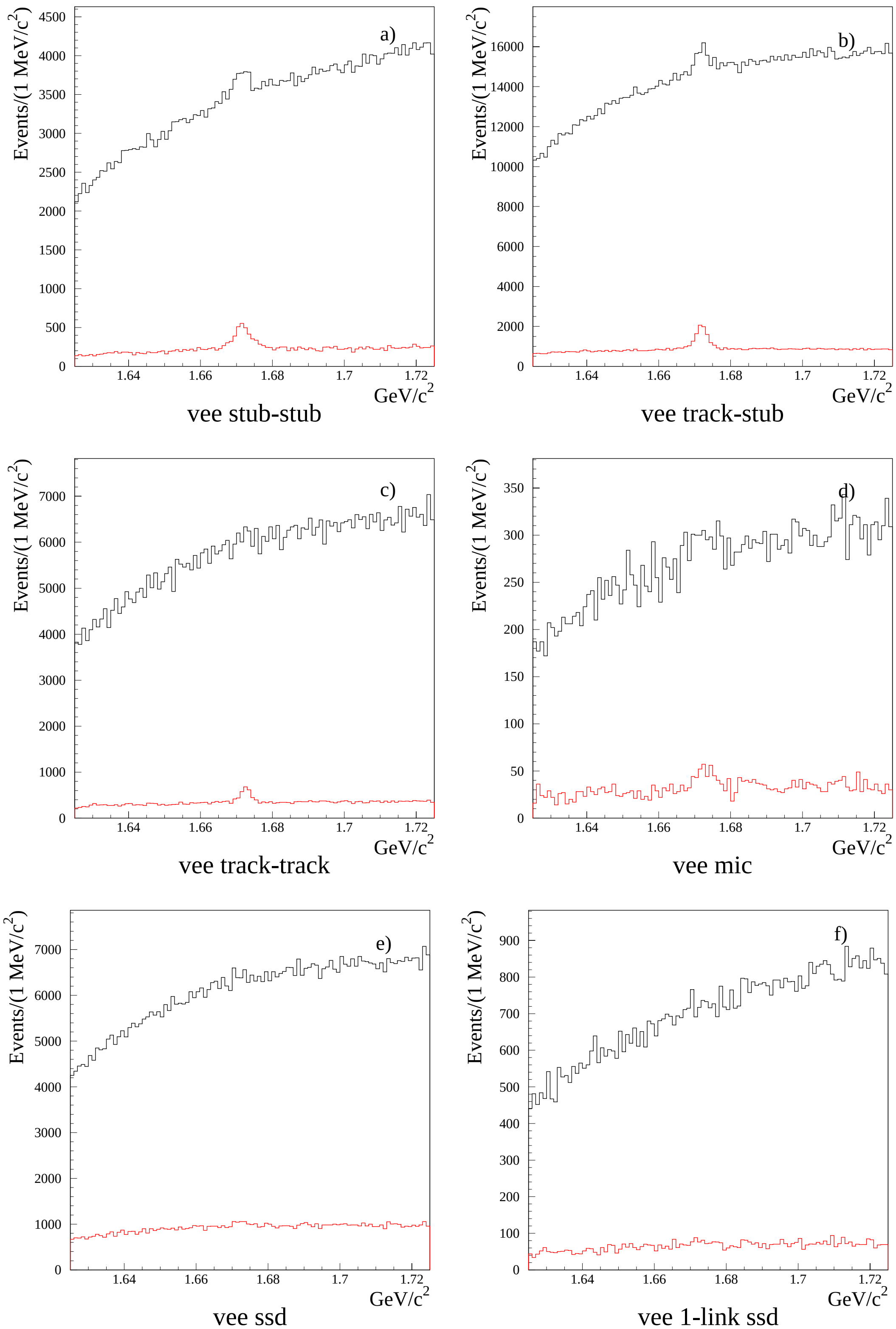

Figure 4.8: Invariant mass for the $\Lambda^0 K^-$ combinations type 1 for different vee categories

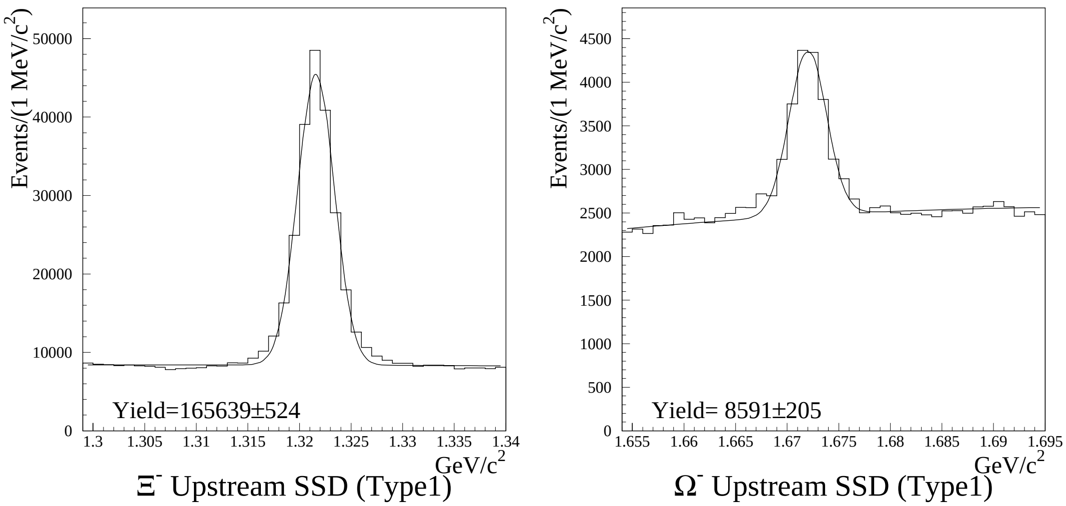

Figure 4.9: Invariant mass of $\Lambda^0\pi^-$ and $\Lambda^0 K^-$ from the full data set for the decays occurring upstream of the SSD

4.7.2 Downstream reconstructed cascades

The downstream cascades decays or Type 2 cascades are those which decay downstream of the last SSD plane and upstream of the first MWPC plane. A schematic of a typical Ξ^- decay in this category is presented in Figure 4.10.

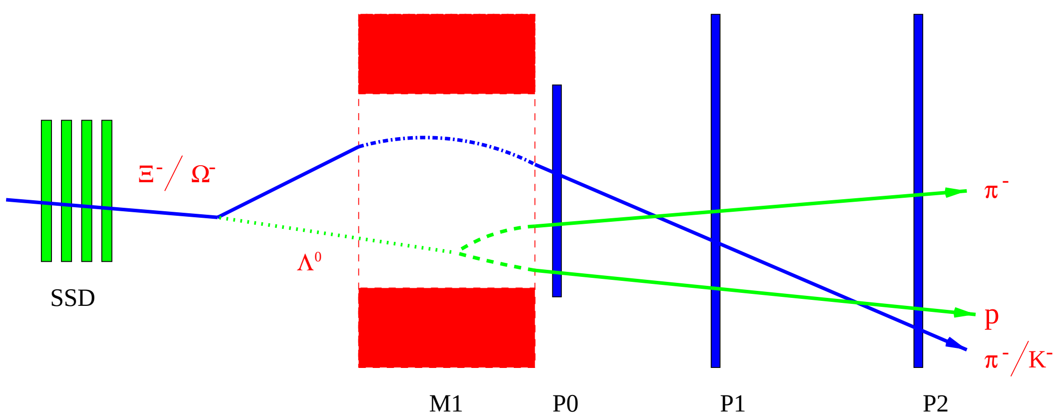

Figure 4.10: Schematic of a cascade decay downstream the SSD system.

The average decay distance of this category is more than one meter along the beam direction. A very important advantage to these decays is that the Ξ^-/Ω^- leaves a track in the SSD detector before decaying. This track can in turn be used for finding charmed particle baryon decay vertices.

The reconstruction algorithm begins by pairing each Λ^0 with every unlinked MWPC track in the event. An estimate is made for the vee-track vertex by computing the z intersection of the Λ^0 vector and the track in the non-bend view x-z plane. If this vertex is downstream of P0 or more than 50 cm upstream of the target, then the combination is rejected. An estimate for the x and y positions of the vertex is given by the x and y of the Λ^0 vector at the given z of the cascade vertex because the Λ^0 is neutral its path is not deflected by the field of M1. The unlinked track is next traced through the magnetic field of M1 to the position of the putative vertex. If the track is 3-chamber, then an iterative procedure is used whereby the track is assigned a different momentum for each iteration until a good trace is made to the given vertex. A better determination of the z position is made by computing the distance of closest approach between the Λ^0 vector and track. (This iteration is important because the track can pass through only one side of the magnet making fringe field corrections more important.)

Next, the SSD track of the candidate charged cascade is found. The sum of the momentum vectors of the Λ^0 and the track are used to form a cascade candidate. Unlinked SSD tracks are looped over and an attempt is made to match each one with the cascade candidate. If the Λ^0 under consideration is a single-linked MWPC vee then the SSD track of the linked prong of the vee is also considered as a candidate. Each candidate SSD track is traced downstream to the vee-track vertex; if the vertex is within the field of M1, then the magnetic trace procedure is used otherwise the SSD track is simply extrapolated to the vertex. Because the SSD track has much better position resolution than does the vee, a better vertex position can now be determined. The new z position is defined as the z where the SSD track and the MWPC track make their closest approach. If the z position is downstream of P0 or upstream of the target, the SSD track is rejected as a candidate.

To remove spurious matches in this selection, a cut is made on the candidate vertex. The candidate vertex is calculated in two ways: the point where the Λ^0 and the MWPC track make their closest approach, and the point where the SSD track and the MWPC track make their closest approach. A cut is made on the transverse distance (in the x-y plane) between these two putative vertices and is required to be less than 1.2 cm for all vee categories. The second quantity on which a cut is applied is the difference between the x and y slopes of the SSD track and the slopes given by the sum of the Λ^0 and the MWPC track momentum vectors. The basic algorithm require that the x and y slopes must agree to within 4 milliradians of the momentum vectors.

The cases where the cascade is reconstructed using a Λ^0 vee with SSD information are excluded in this category because the cascade decay is expected downstream the SSD system, due to the boost of the cascade. Figure 4.11 shows the Λ^0-π^- and Λ^0-K^- combinations excluded from the full data set.

In order to improve the signal-to-noise of type 2 cascades, a narrower window in the slope difference in x (DSX) and y (DSY) is required. To accomplish this, we first

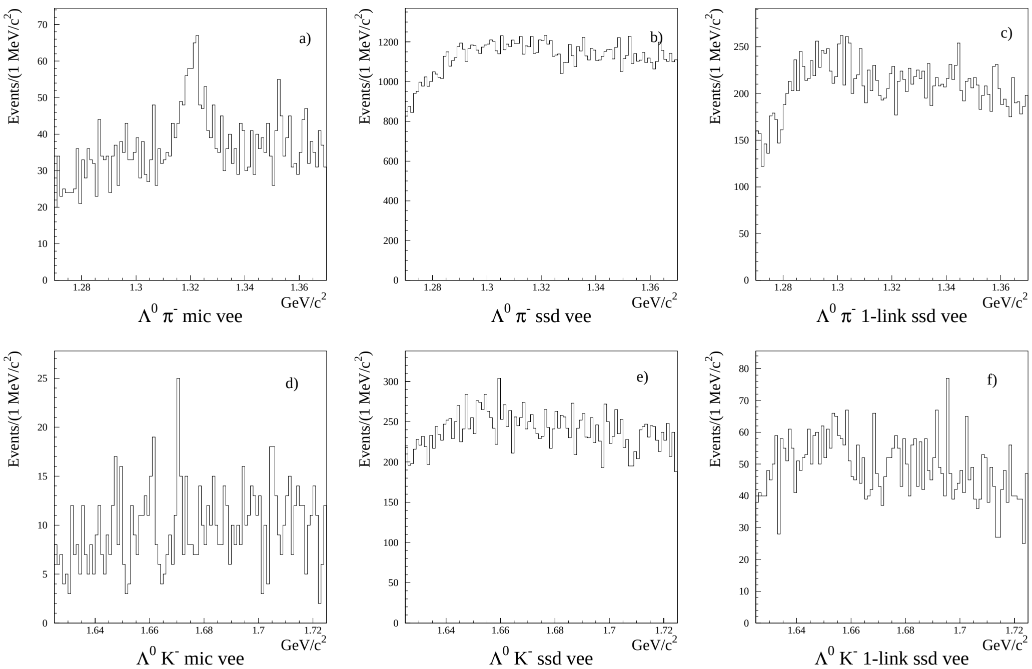

Figure 4.11: Excluded cascade combinations according to vee categories.

need to remember that vees are reconstructed with only a rough knowledge of their actual production vertex. For purposes of track finding the assumption is made that the tracks originate at the primary vertex as shown in Figure 4.12. In the case of cascades this assumption causes a slightly wrong vee slope which tends to be at a closer angle than the true one. This primary vertex dependence problem is because of the constraint used for M1 vees where at least one leg is stub or 3-chamber track.

To refit the vee, the production vertex is found using the cascade track (SSD track) and its pion daughter (MWPC track), then in a iterative process the vee parameter is recomputed from the given production vertex and then the vee is intersected with the MWPC track resulting in a new cascade decay vertex and a new cascade momentum. The new cascade momentum is used to trace the SSD track downstream to the vertex location to compute the new x and y slope and then DSX and DSY. If possible a 3-D intercept vertex is found using the vee, the MWPC track, and the SSD track.

Table 4.1 shows the requirements to keep a cascade candidate. For the Ω^- hypothesis a Čerenkov particle identification is required to reduce pion contamination in addition to the refit criteria. In Figure 4.13 and Figure 4.14 are shown the Ξ^- and Ω^- signals before and after applying the cuts in the angle difference in x and y for each vee category.

The invariant mass plot for downstream cascade decays for the Λ^0 π^- and Λ^0 K^- combinations are presented in Figure 4.15. In this region one finds that the Ω^- yield

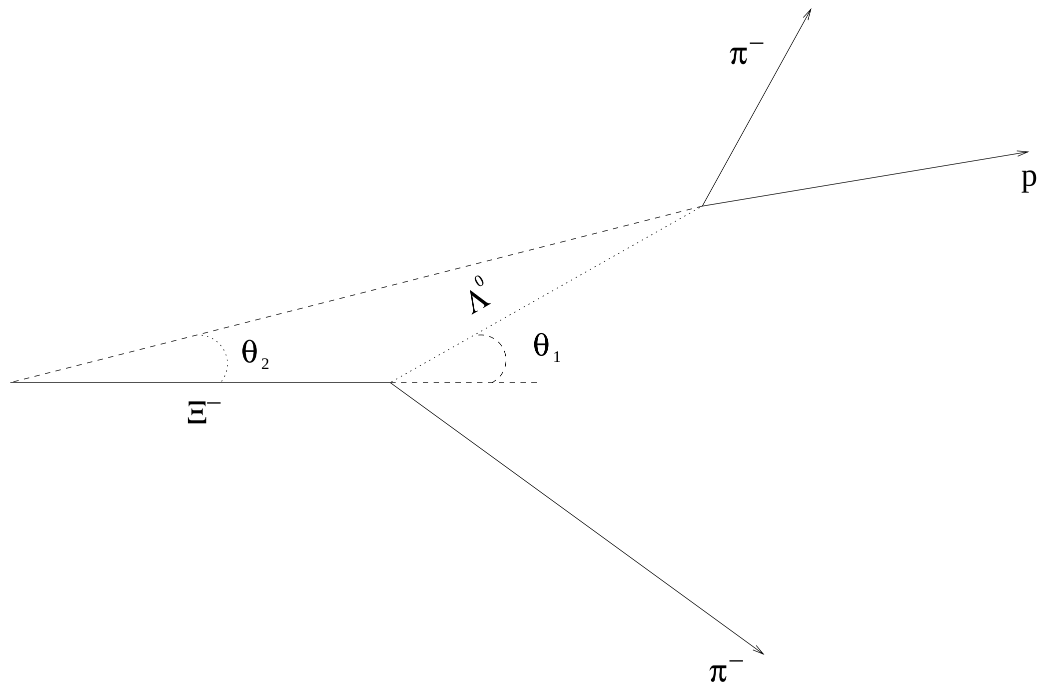

Figure 4.12: Sketch of a cascade decay to display the need of refit the vee where θ_2 is the vee direction reconstructed and θ_1 is the true direction.

Table 4.1: Cuts required for cascade candidates

refit	vee category	slope difference (<) in x	slope difference (<) in y
	Ξ^-		
success	all M1, single link trak-trak	no cut	no cut
success	single link trak-stub and stub-stub	1	2
fail	all M1	1	2
fail	single link trak-trak and trak-stub	1	1
	Ω^-		
success	M1 stub-stub	2	3
success	M1 trak-trak and trak-stub	2	2
success	single link trak-trak	1	2
success	single link trak-stub and stub-stub	0.5	1
fail	M1 trak-stub	0.5	1
fail	single link trak-stub	0.5	0.5

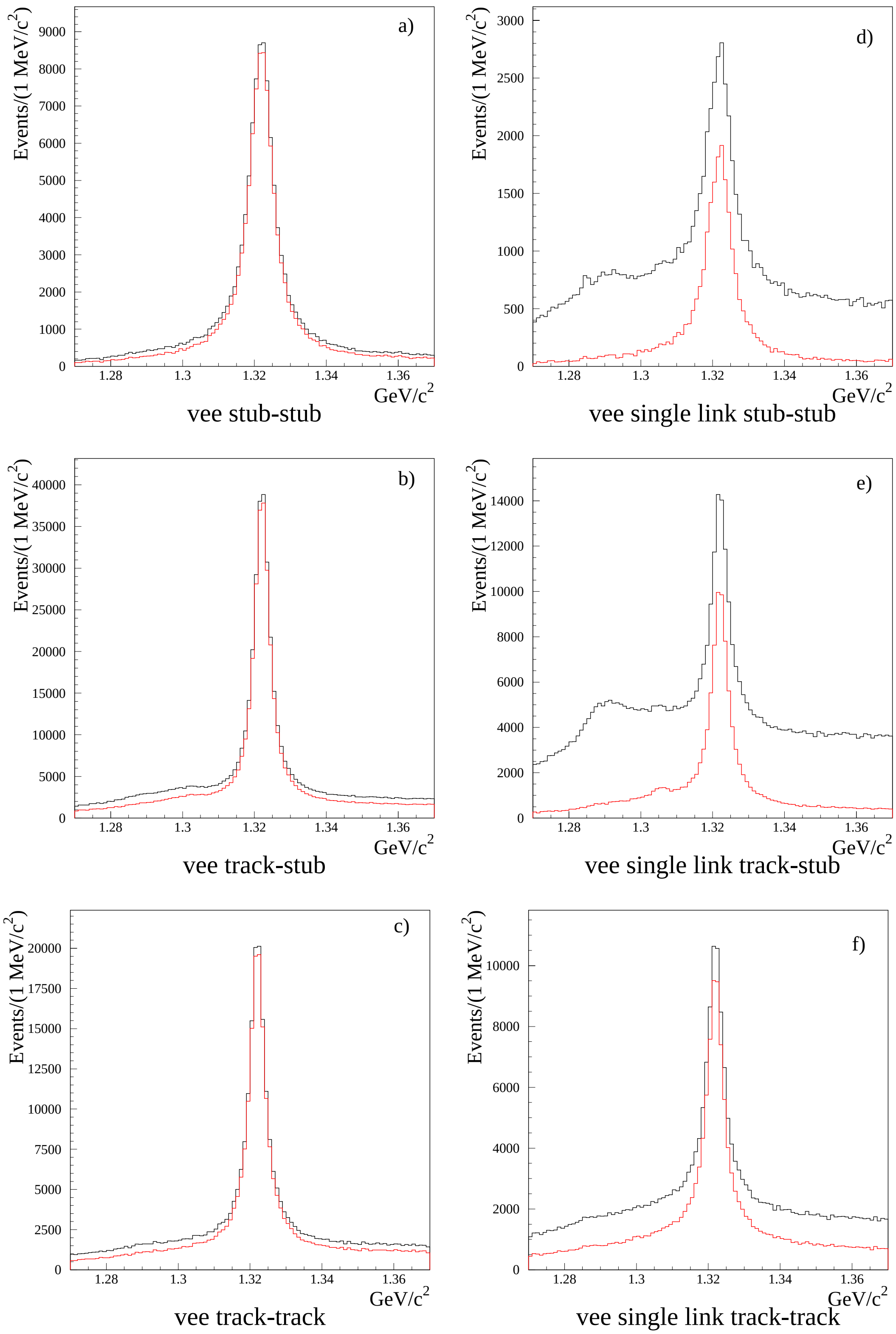

Figure 4.13: Invariant mass for the $\Lambda^0\pi^-$ combinations type 2 for different vee categories

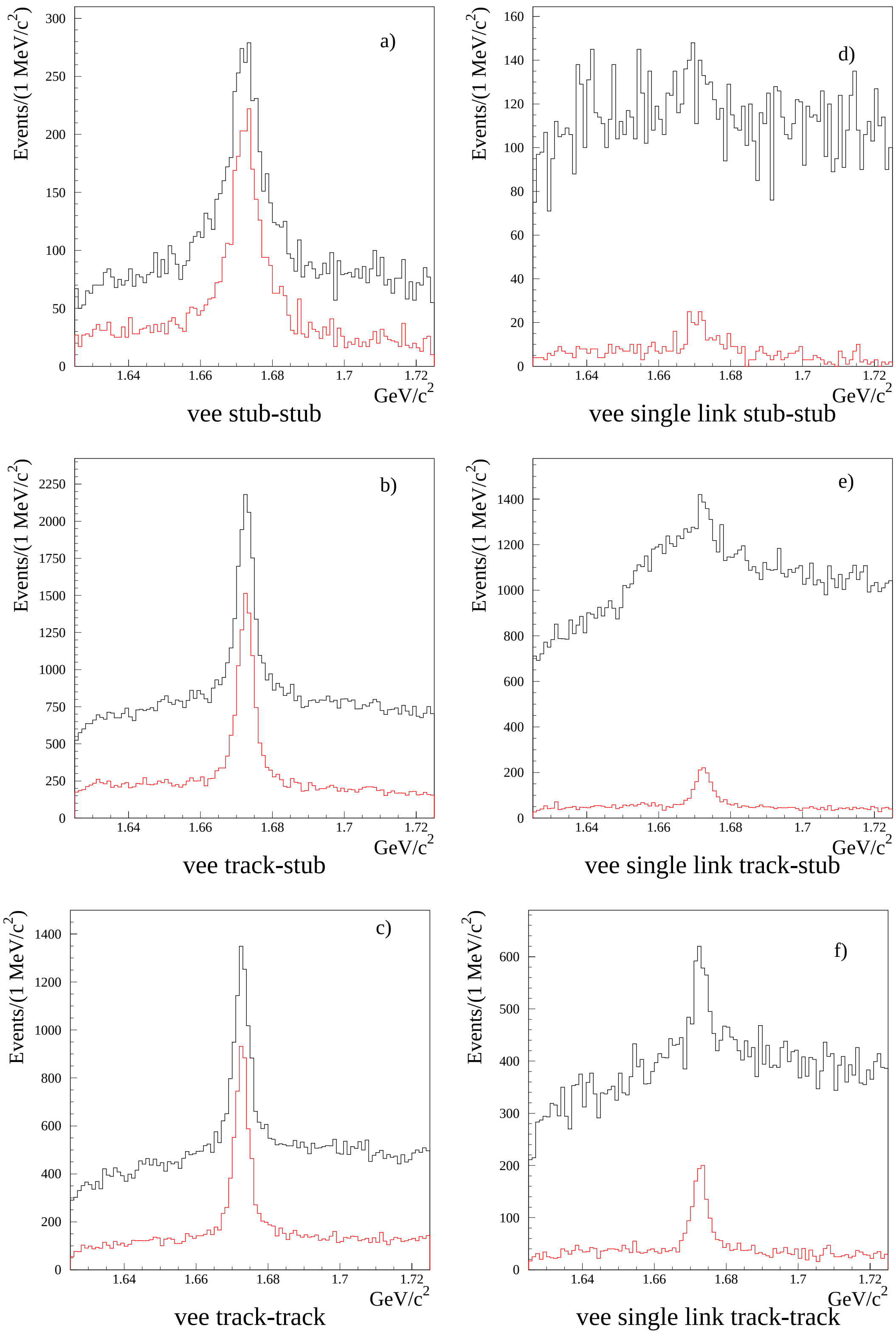

Figure 4.14: Invariant mass for the $\Lambda^0 K^-$ combinations type 2 for different vee categories

is a factor of 30 lower than the Ξ^- yield. The ratio of the Ξ^- yield to the Ξ^- yield is reduced downstream of the SSD detector due to the shorter Ω^- lifetime relative to the Ξ^-.

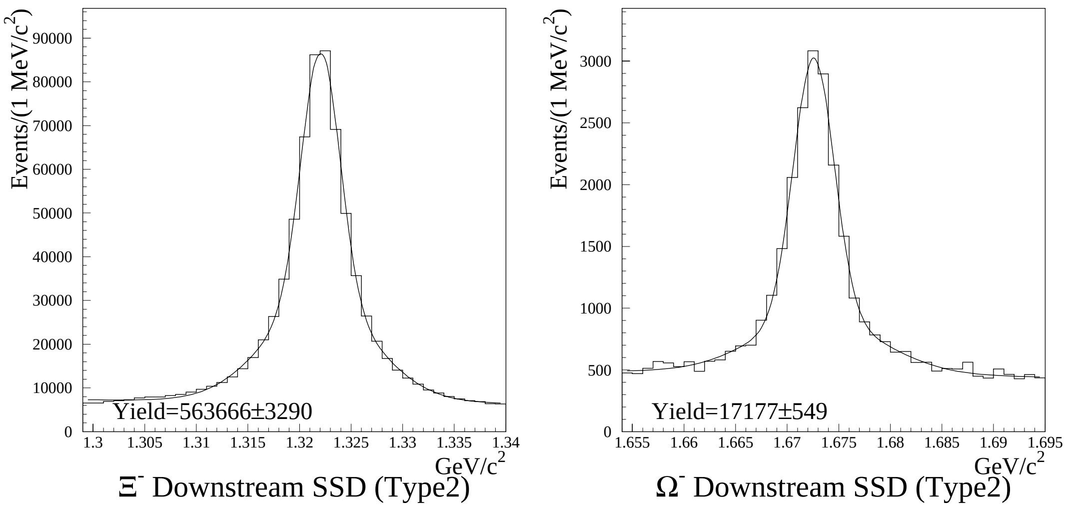

Figure 4.15: Invariant mass of $\Lambda^0\pi^-$ and $\Lambda^0 K^-$ with the full data set for the decays downstream of the SSD

4.7.3 Multivees reconstructed cascades

As in the case of downstream cascades or Type 2 cascades, multivees also reconstruct charged particles which decay downstream of the SSD system and upstream the first MWPC plane. A multivee is composed of three unlinked MWPC tracks and one unlinked SSD track. A schematic drawing of a multivee decay is presented in Figure 4.16. While the category was designed to select three prongs decays such as $K^- \to \pi^-\pi^-\pi^+$, it has proven to be useful in recovering Ξ^- and Ω^- decays where the Λ^0 decay vertex is close to the Ξ^- decay vertex. It also works well in reconstructing vees from cascade decays which open in the vertical plane of the magnet, where the efficiency is low for the standard vee algorithm.

The multivee algorithm starts by selecting three unlinked MWPC tracks which are intersected in the x-z plane and by selecting an unlinked SSD track requiring the closest distance approach at the x-z vertex as a match, so long as it is less than 2 cm separation. The algorithm is separated into decays which occur upstream of M1 and within M1.

If the decay vertex is upstream of the M1 magnet, then the SSD track is extrapolated in z and each of the 3-chamber track are traced to the SSD y vertex position. If there

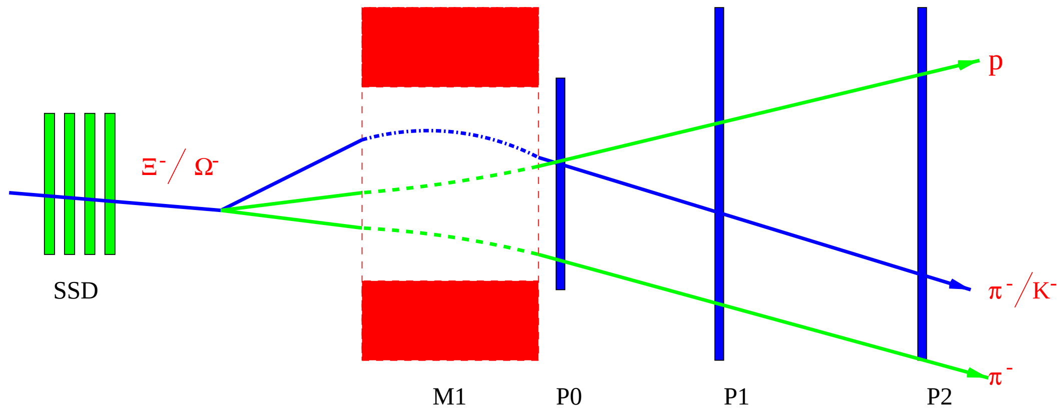

Figure 4.16: Schematic of a multivee reconstruction.

are 5-chamber tracks, then they are swum upstream and intersected with the SSD track to find a better vertex position.

If the decay occurs within the magnetic field, then there must be at least one 5-chamber track. The vertex of the three unlinked MWPC tracks is found in the x-z plane and the y location of the vertex is determined by swimming the 5-chamber tracks to the z location. If more than one 5-chamber track exists, then the z location is determined using the combined $x + y$ information. All remaining unlinked 3-chamber track are traced to the y-z vertex and their momentum is calculated.

Next, the sum of the three MWPC unlinked track momenta is found and assigned to the SSD track. This unlinked SSD track is now traced downstream to the z vertex. Successful candidates must be near the vertex of the three unlinked MWPC tracks by less than 0.5 cm and must agree in slope to within 2 milliradians in both the x and y views to the combined momentum vectors of the three tracks.

In Figure 4.17 the invariant mass distributions for $\pi^+\pi^+\pi^-$, $p\pi^-\pi^-$, and $pK^-\pi^-$ combinations are presented. While the charged kaon decay events are not used in our analysis packages, the Ξ^- decays and Ω^- decays are used.

4.7.4 Kinks reconstructed cascades

The algorithm for reconstructing the cascades decaying to a Λ^0 plus a pion or kaon as presented in Figure 4.18 is similar to the Σ decays discussed in Section 4.6. Unfortunately, there is no good technique to reduce the sample with additional constrains such as energy in the calorimeter or with Čerenkov cuts. For this reason we chose to only reconstruct events where the Ξ^- decay occurred within the magnetic field of M1. There are three advantages to using this subsample. First, the reconstructed pion or

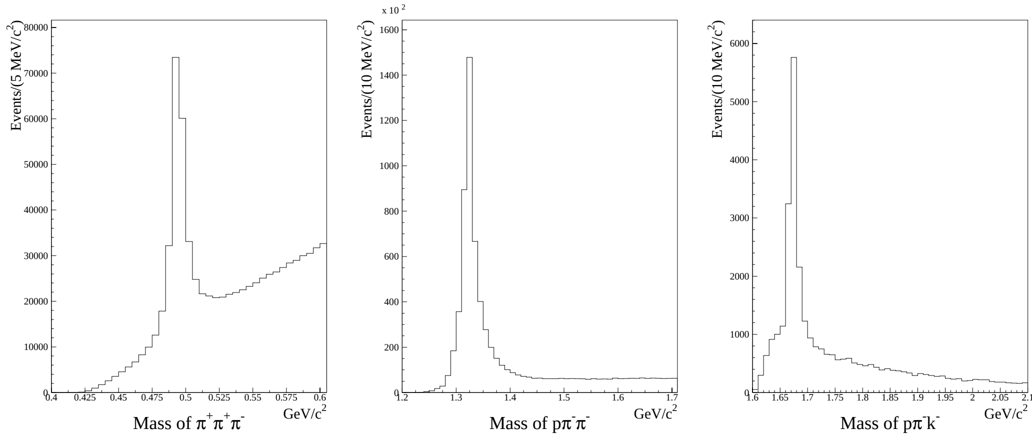

Figure 4.17: Invariant mass distributions for $\pi^+\pi^+\pi^-$, $p\pi^-\pi^-$, and $pK^-\pi^-$ combinations. Signals for $K^+ \rightarrow \pi^+\pi^+\pi^-$, $\Xi^- \rightarrow \Lambda^0\pi^-$ and $\Omega^- \rightarrow \Lambda^0 K^-$ where $\Lambda^0 \rightarrow p\pi^-$, are clearly evident.

kaon is a 5-chamber track and its momentum is well defined by its passage through M2. Second, there is no two-fold ambiguity in this category as the cascade also bends in the magnetic field. Third, the decays are well-separated from any material and the background from large multiple scatters is significantly reduced.

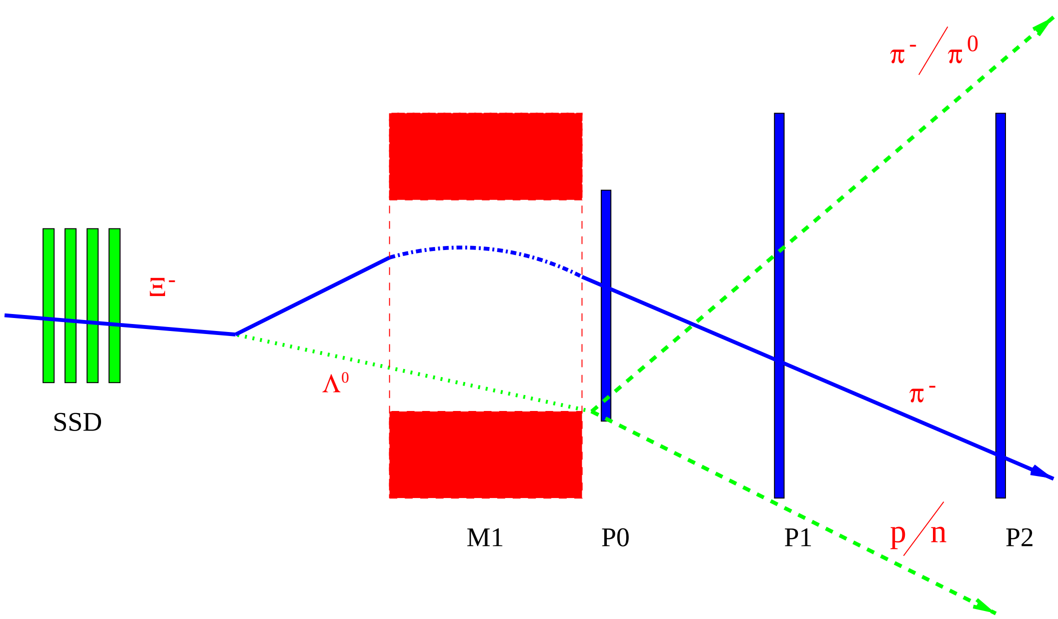

Figure 4.18: Schematic of a cascade kink reconstruction.

4.8 Muon identification

Muon identification is provided by the outer and inner muon detectors. Each five chamber track is extrapolated to the inner detector and each three chamber track to the outer detector.

4.8.1 Identification in the Inner Muon detector

Muons are identified in the MH system (described in Section 3.8.2) by the following requirements. First, the track is extrapolated into the MH system and a search of hits is made in a $3\sigma_{mcs}$ window, where σ_{mcs} is the width of multiple Coulomb scattering distribution (a Gaussian distribution is a good approximation). The candidate track is required to have hits in at least four of the six MH planes. If the requirement is satisfied, then the χ^2 is calculated. In case of multiple combinations of hits, we choose the set of hits which gives the lowest χ^2. The χ^2 calculation takes into account both the multiple Coulomb scattering of the muon within the calorimeters plus the steel of filters and the granularity of the scintillator paddles. The χ^2 distribution is a convolution of Gaussian (due to multiple Coulomb scattering) and a flat (due to granularity) distributions, but in practice we approximated to a linear combination of both distributions to be able to construct an approximate flat distribution of probabilities (CL). The set of chosen hits are tested in other tracks, and the largest confidence level of a second track is reported to be used later as an isolation cut. The muon identification algorithm is well described elsewhere [41–43].

Low momentum muons have a big search window in which hits from other muons could be erroneously taken, lowering the efficiency of identifying those muons. To recover these tracks, the requirement in the number of planes is relaxed from four to two planes for muons with momentum less than 10 GeV/c. If the CL is less than 1%, then the track is reanalyzed selecting the hits in a smaller window ($2\sigma_{mcs}$). If the CL is still too low, then the process is repeated using a window of $1\sigma_{mcs}$. This iteration process increases the efficiency for low momentum muons.

Above 10 GeV/c, the typical efficiency of the muon identification algorithm is above 98% with a proton misidentification rate as a muon being less than 0.1%. The pion misidentification rate is larger (about 1%), but this is due to in flight $\pi^+ \to \mu^+\nu_\mu$ decays in the spectrometer where the μ^+ flight direction closely matches the pion's. A comparison of the calculated momenta from M1 and M2 also rejects some of these in flight decays.

4.8.2 Identification in the Outer Muon detector

Muons are identified in the Outer Muon system (see Section 3.8.1) with a method similar to that used in the Inner Muon system. However, there is an added complication since the iron shield (M2) has an internal magnetic field which deflects muons. The OM identification routine accounts for this by tracing muons through the magnetic field in the M2 steel and by applying the multiple Coulomb scattering smearing (in both the OE and M2) to the traced position. This process is described in detail in Reference 44.

The OM reconstruction algorithm is efficient for muons down to $E \approx 4$ GeV, the range of muons in the OE and M2.

4.9 Electron identification

Although the Čerenkov system can provide some electron identification, the ability to separate electrons from pions is not available above 8.5 GeV for stubs and 17 GeV for tracks (see Table 3.4). Above these energies, calorimetry information is needed to separate electrons from hadrons and muons.

In both the IE and the OE, the identification method relies primarily that $E/p \approx 1.0$ for the track in question. In the IE, a cut of $0.8 < E/p < 1.2$ is typically used. For the OE, the window is a somewhat wider. Almost all the electromagnetic energy is contained in the calorimeters while much of the hadronic energy, even if an interaction occurs, passes through. (Muons leave about 1 GeV in these calorimeters.)

In the OE, electrons are further separated from hadrons by studying the shower evolution as a function of z (electromagnetic showers peak well within the detector). A discriminant analysis of the evolution is incorporated into the electron identification code.

The IE electron identification is improved by requiring that the Čerenkov identification algorithm confirms the assumption that the track is an electron.

4.10 Data Processing

The FOCUS raw data consists of about 6.5 billion photon interaction events on approximately 6000 8 mm tapes, with 4.5 Gb (gigabytes) of information per tape. The total data set size is roughly 25 Tb (terabytes). The data sample was reduced in three steps which include reconstruction and event selection processes. An overview of the entire FOCUS data reconstruction process is shown in Figure 4.19.

In the first step or "Pass1", each event was reconstructed and written to tape. The raw data written by the DAQ system were reconstructed and analyzed with the output being written on a one to one correspondence between input and output tapes. The complete process was done at Fermilab.

In the second step or "Skim1", some events were discarded and the events were split into six sets of output based on broad physics topics (see Table 4.2). About half of the events surviving the Pass1 process were written out by Skim1, with many of those events being written onto multiple outputs. The different outputs were also transferred to Fermilab over the internet for easy access by experimenters. Institutions in charge of Skim1 process were mainly the University of Colorado and Vanderbilt University, leaving the recovery task or reprocessing of failing tapes to Fermilab.

Table 4.2: Descriptions of skim1 output. There are about 30 different skims, grouped into six outputs per input based on physics topics and the type of information present.

Output	Physics Topics	Skim2 Institution
1	Semi-leptonic	Puerto Rico
2	Topological vertexing and K_s^0	Illinois
3	Calibration and rare decays	CBPF, Brazil
4	Baryons	Fermilab
5	Diffractive (light quark states)	California, Davis
6	Hadronic meson decays	California, Davis

In the final step of "Skim2" each of the previous sets of data were split further, based on more narrow physics topics. Because of the size of the Skim1 output data sets (200-500 tapes) are still too large to be used, each Skim1 output was split again into many streams. Events which did not pass more stringent cuts were discarded at this point.

From each Skim1 output or Super-stream, 5 to 12 streams were written, covering a variety of topics and calibration data samples. The relevant streams to the analysis presented in this thesis are presented in Table 4.3. Some of the streams were further reduced as described below and are independent of the analysis.

The cascade skim (Ξ^- and Ω^-) was reduced with the requirement of the detachment of the cascade decay as described in Section 4.7.1 for the upstream cascades, and vees are refit for the downstream cascade as described in Section 4.7.2. The reduced sample is highly efficient and the size of the output is reduced to two tapes or about 9 Gb.

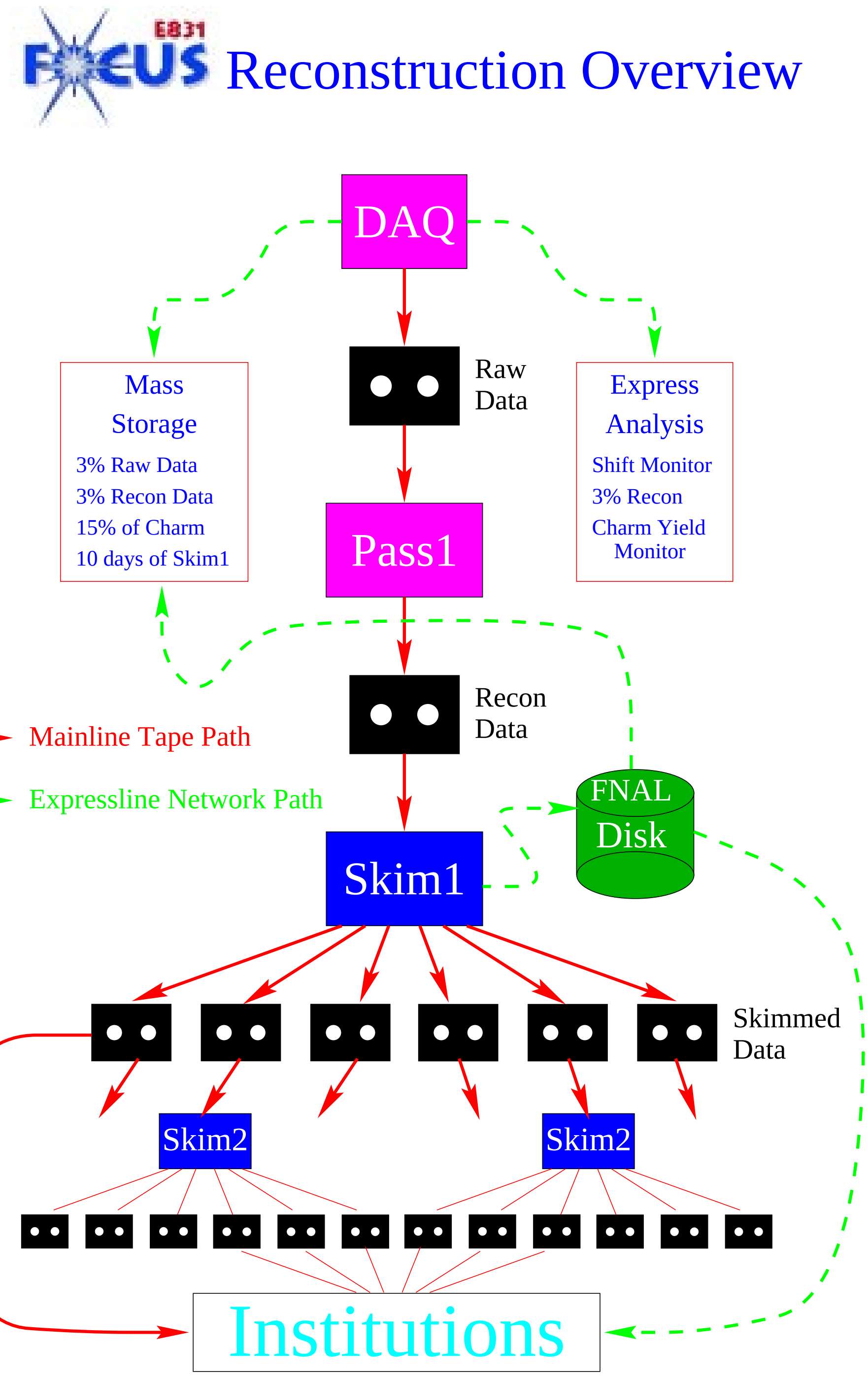

Figure 4.19: Overview of the FOCUS reconstruction process. The solid lines show the path of the data written to 8 mm tapes (the source for all final analyses). The dotted lines illustrate the distribution of large amounts of data via the Internet, which was used to help collaborators get data quickly for studies and preliminary analyses.

The Global Vertex skim is meant to be used as a normalization for Branching Ratios or as in this case to recover skims missing at Skim1. The reconstruction of the cascades as kinks was not considered originally as described in Section 4.7.4. By redoing the Global vertex skim and by running the kink algorithm for the case of $\Xi^- \rightarrow \Lambda^0\pi^-$ and $\Omega^- \rightarrow \Lambda^0 K^-$ when the Λ^0 is missing and the decay is within M1, we obtained the cascade kinks skim with an output of about 2.5 Gb.

The Multivee skim was reduced by requiring the three prongs were $p\pi^-\pi^-$ or $pK^-\pi^-$ where a $p\,\pi^-$ combination was consistent with a Λ^0. The skim output of the cascade multivee skim was about 2 Gb.

Table 4.3: Descriptions of several streams. These are only the streams used in this thesis. Many others exist for other types of physics.

Super Stream	Stream	Physics Topics	Number of tapes
4	FSDA	Λ^0	58
4	FSDB	kinks	77
4	FSDD	$\Lambda_c^+ \rightarrow pK^-\pi^+$	15
4	FSDJ	Multivees	09
4	FSDL	Ξ^- and Ω^-	17
2	FSG	Global Vertex	281

Chapter 5

Selection of Ξ_c^+ candidates

In this chapter we detail the methods used for selecting Ξ_c^+ candidates in the decay modes $\Xi_c^+ \to \Xi^-\pi^+\pi^+$, $\Xi_c^+ \to \Sigma^+K^-\pi^+$, $\Xi_c^+ \to pK^-\pi^+$, and $\Xi_c^+ \to \Lambda^0K^-\pi^+\pi^+$.

5.1 Vertexing

The fact that charmed particles travel only a short distance in the spectrometer before they decay requires great precision in reconstructing vertices. The microstrip detectors described in Section 3.2, make it possible to accomplish such task when we are able to distinguish two distinct vertices which correspond to the *primary* or production vertex and the *secondary* or decay vertex. By reconstructing and distinguishing the two vertices we can reduce non-charm background. A schematic of a $\Xi_c^+ \to \Xi^-\pi^-\pi^-$ decay and its vertices is shown in Figure 5.1.

The Ξ_c^+ candidate is reconstructed using a candidate driven vertexing algorithm [45]. A Ξ_c^+ candidate vertex is formed using the silicon track information of the decay of the daughters when available. If a valid (secondary) vertex is found, then a seed track is constructed using the momentum vector of the Ξ_c^+ candidate. The momentum vector must be intersected with at least two other tracks to form the primary vertex.

5.1.1 Vertex confidence levels

Each vertex that is formed has an associated confidence level. The minimal cut to declare a vertex valid is that the confidence level be greater than 1%. This is because the tracks will not intersect exactly as is shown in Figure 5.1. We calculate

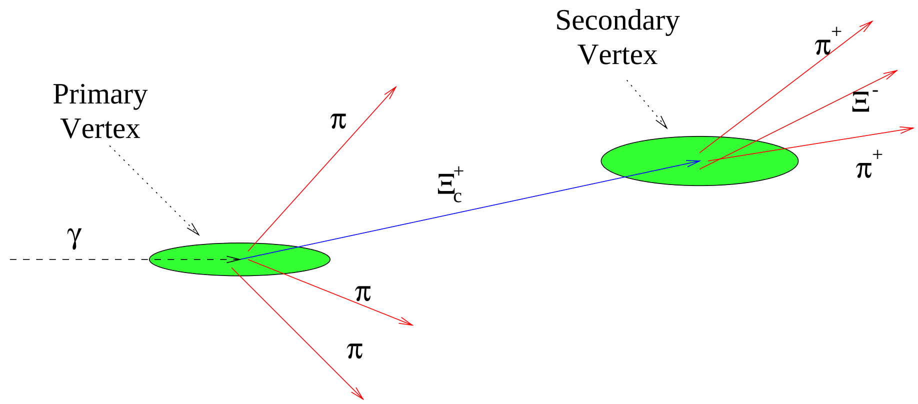

Figure 5.1: Schematic of a $\Xi_c^+ \rightarrow \Xi^-\pi^-\pi^-$ decay. The ellipses illustrate the centers and errors of the vertices. L, described in the text, is the distance between the centers of the two ellipses.

the probability that all candidate tracks are consistent with intersecting within the errors. In the case of a real vertex the probability distribution is expected to be flat distribution and hence, the requirement of 1% is 99% efficient. However a slightly larger cut is often useful in rejecting random combinatoric backgrounds. For this analysis the secondary vertex is required to have a confidence level (**CLS**) above a value optimized for each topology reconstructed, the primary vertex is required to have a confidence level (**CLP**) greater than 1%.

5.1.2 Detachment (L/σ_L)

A powerful cut to bring out a charm signal from the background is the detachment cut or significance of separation between the primary and secondary vertices. Short lived hadronic background and random combinations are effectively reduced. The detachment cut requires L/σ_L to be greater than some amount; where L is the distance between the two vertices determined in a global fit of both vertices (where the primary vertex position is recomputed by a fit excluding the seed track) and σ_L is the uncertainty in L. The quantity L/σ_L is a unbiased measure of the significance of separation of the primary and secondary vertices.

5.1.3 Primary in Target (TGM)

A real primary should come from the interaction of the photon with the target, so we require that the primary vertex to be located within 3 units of the uncertainty in the primary vertex position (TGM < 3). This cut is tightened to be positively inside the target (TGM < 0) for the cases where the Ξ^- or Σ^+ are partially reconstructed (kinks).

5.1.4 Secondary upstream TR1

Because TR1 is part of the level 1 trigger, a charm event decaying after TR1 needs another mechanism to trigger the event. To avoid complications with simulating opposite side charm, we reject events decaying after TR1 by requiring that the z of the secondary vertex be less than 2 cm.

5.1.5 Secondary isolation (ISO2)

In some cases the detachment cut is insufficient to bring out a clean signal and other tools are necessary to remove background. One of the tools is the isolation confidence level of the vertex or simply **ISO2**. Its value is determined by the largest confidence level that any other track (not part of the primary) originates from the secondary vertex.

5.1.6 Uncertainty in the proper time

The uncertainty in the proper time is defined as $\sigma_t = \sigma_L / \beta\ \gamma\ c$ where $\beta\ c$ is the particle velocity and γ is the Lorentz boost factor in the Ξ_c^+ lab frame. This cut is optimized for each decay mode.

5.2 Čerenkov Identification

As described in Section 4.3, the CITADL algorithm calculates negative log likelihoods for the electron, pion, kaon, and proton hypothesis for each track. By cutting on *differences* between the particle hypotheses, we determine the particle identification.

Pion identification: To identify pions, we use a cut called ΔW_π (pion consistency). This cut determines how likely the pion hypothesis is compared to the other hypotheses. The definition of ΔW_π is

$$\Delta W_\pi \equiv \min(W_e, W_K, W_p) - W_\pi \tag{5.1}$$

which allows for values in the range $(-\infty, \infty)$.This cut typically causes only small losses in the signal yield at a value of -6. This means that some other hypothesis is favored over the pion hypothesis, but not by a large amount. Because of the limited momentum range of positive pion identification, requiring $\Delta W_\pi > 0$ is inefficient. However, the purity of signals with such a strong cut is very high.

Kaon identification: Since most of the particles produced in target interactions are either electrons or pions, we cut on the difference between the kaon and pion hypothesis. The variable "kaonicity" (ΔW_K) defined previously in Section 4.3 as $W_\pi - W_K$ is generally enough to identify kaons by just requiring positive values for ΔW_K. For this analysis the value used is ΔW_K >2.

Proton identification: Typically in the absence of kaons a cut similar to the kaonicity is used We define "protonicity" (ΔW_p) as $W_\pi - W_p$. But when kaons are source of contamination a separation between protons and kaons is mandatory. In this case we use $W_K - W_p > 0$.

5.3 $\Xi_c^+ \to \Xi^-\pi^+\pi^+$ selection criteria

This particular decay mode has been reconstructed using four different reconstruction techniques for the Ξ^- (as described in Section 4.7). Common to all topologies is that the pion tracks must be reconstructed and that the candidate driven vertexer algorithm must successfully reconstruct a primary and a secondary vertex. Both pion tracks must be identified as pions with ΔW_π >-6. Below are the cuts used to select Ξ^- for each topology and additional cuts used in the reconstruction of Ξ_c^+ candidates depending of the Ξ^- topology.

5.3.1 Ξ^- Type1

In this topology the Ξ^- has no vertex information. A component of the background due to random combinations of the Ξ^- and the pions need to be reduced. We require that the Ξ^- must originate from the same vertex as the two pions and that the decay vertex should be in the plane which contains the Ξ^- pion daughter as shown in Figure 5.2. The intersection of the Ξ^- is constrained to come from the two pions' vertex and is forced to intersect its own pion daughter. This technique allow us to find a real Ξ^- vertex decay from the intersection of the Ξ^- with its pion daughter. The Ξ^- vertex decay can also be treated as a regular vertex, i.e. compute its confidence level and determine its detachment from any other vertex.

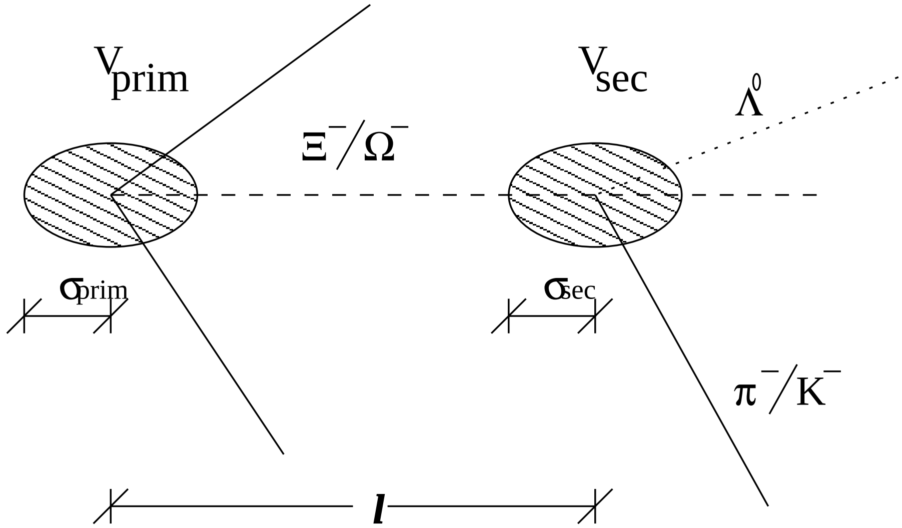

Figure 5.2: Schematic of a vertex reconstruction with Ξ^- upstream SSD. The cascade is pinned to the production vertex and with that constraint, it is forced to intersect with its pion daughter.

The Monte Carlo results presented in Figure 5.3 guide us in determining reasonable cut values. A confidence level of 1% for the Ξ^- vertex decay is good enough to reject most of the combinatorial background and the Ξ^-'s which do not come from the vertex formed with two pion tracks i.e. the Ξ_c^+ vertex decay. In the analysis, we preferred to use a tighter cut and used a 10% vertex confidence level. Next, the criteria used to select Type1 Ξ^- particles are presented. They are:

- Ξ^- candidates which already passed the skim cut (L/σ_L >5)
- Only M1 vees are used to reconstruct Ξ^- candidates.
- The vertex confidence level greater than 10% is required for the Ξ^- candidates.
- Particle identification for Ξ^- candidate pion daughter of $\Delta W_\pi > -3$
- The Ξ^- candidate is required to have an invariant mass within $\pm$ 4 MeV/c^2 of the reconstructed mass of 1.3216 GeV/c^2.

The Ξ^- candidates which passed the previous criteria and come from the Ξ_c^+ decay vertex will be referred as Type1 Ξ^-'s. The two pions from the Ξ_c^+ decay vertex are required to have a **CLS**>10%. The z component of both pion's momentum are required to be greater than 3 GeV/c^2. The $\Xi^-\pi^+\pi^+$ invariant mass for a range of L/σ_L cuts in addition to other selection criteria described above are shown in Figure 5.4.

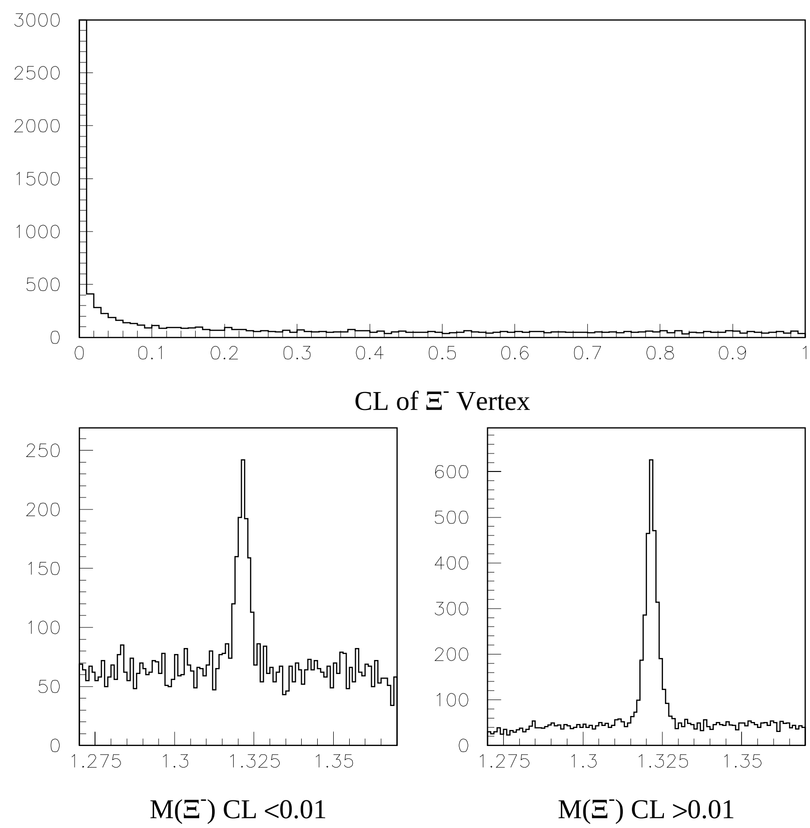

Figure 5.3: Monte Carlo histogram of the Ξ^- vertex decay confidence level. The Ξ^- has been pinned to the pions' vertex. In the bottom figures the $\Lambda^0\pi^-$ invariant mass distributions below and above 1% vertex confidence level are presented.

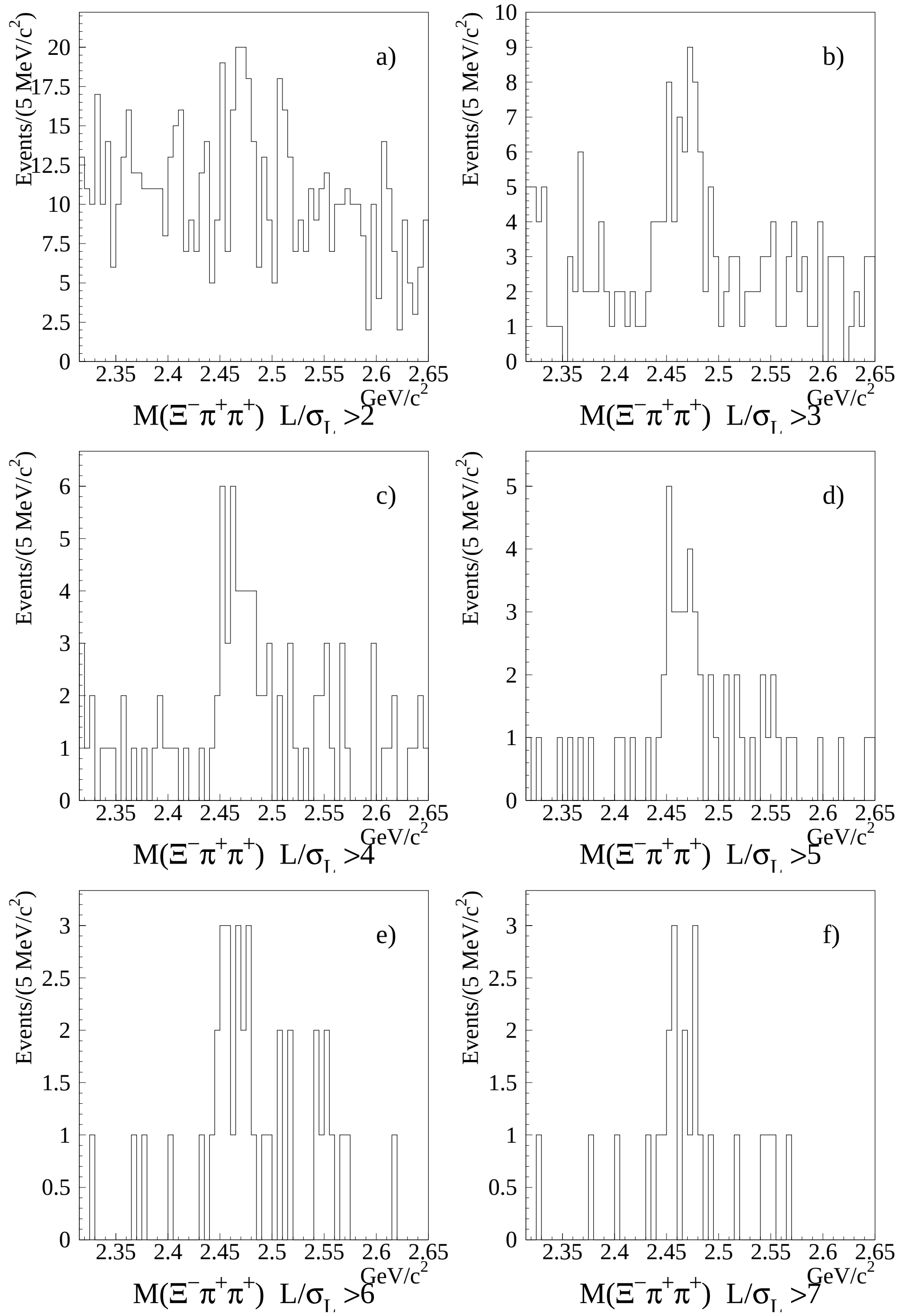

Figure 5.4: $\Xi^-\pi^+\pi^+$ invariant mass distributions using upstream SSD Ξ^- for L/σ_L from 2 to 7.

5.3.2 Ξ^- Type2

This topology in contrast to the Type1 Ξ^-'s has intercept information from the unlinked SSD track which belongs to the Ξ^-, but the mass resolution for the Ξ^- is slightly worse. About 70% of the total Ξ^- are reconstructed through this method. Once the downstream Ξ^- are selected by the skim, the only additional criteria to identify a Type2 Ξ^- is a mass cut within $\pm$ 20 MeV/c^2 of the well-known Ξ^- mass, 1.3216 GeV/c^2. For the $\Xi^-\pi^+\pi^+$ invariant mass only a **CLS** $> 2\%$ is required in addition to particle identification. The invariant mass for a range of L/σ_L cuts is shown in Figure 5.5.

5.3.3 Ξ^- Multivee

This topology is similar to the Type2 topology. The topology is used to recover events where the Λ^0 has not been reconstructed either because there is not a clear separation between the produced and decaying vee vertex or because the vee is not consistent with being produced in the target region. If a Ξ^- candidate is reconstructed as both Type2 and Multivee (MV), then we choose the Type2 topology to avoid duplication. The Ξ^- candidate is positively identified when:

- The MWPC track with the proton hypothesis must satisfy $\Delta W_p > 4$
- The invariant mass of at least one combination of the proton and the pion is consistent with the Λ^0 mass being in the range 1.105-1.125 GeV/c^2.
- The invariant mass of the $p\pi^-\pi^-$ is less than 1.37 GeV/c^2.

The Ξ^- candidates which pass the previous criteria will be referred as MV Ξ^-'s. The vertex formed from a MV Ξ^- and two other tracks with a **CLS**>2% are used to form the $\Xi^-\pi^+\pi^+$ invariant mass. In Figure 5.6 is shown the invariant mass for a range of L/σ_L cuts.

5.3.4 Ξ^- Kinks

As described in Section 4.7.4 the Ξ^- reconstruction through the kink algorithm is similar to Type2 Ξ^-. The Ξ^- are selected in the following manner:

- To reduce combinatorial background, we only use the cases where the decay is within the M1 magnetic volume by requiring z of the cascade decay to be

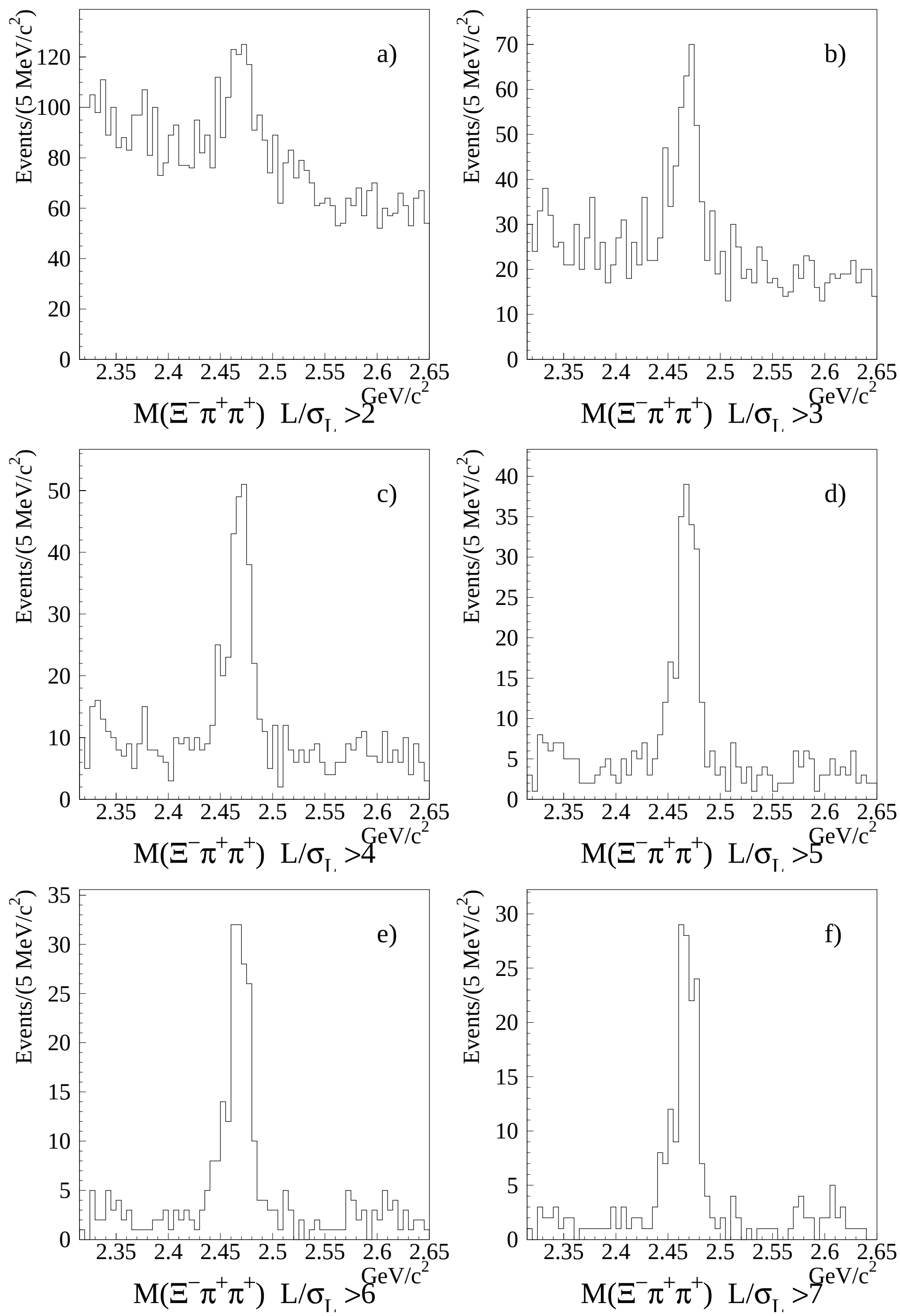

Figure 5.5: $\Xi^-\pi^+\pi^+$ invariant mass distributions using downstream SSD Ξ^- for L/σ_L from 2 to 7.

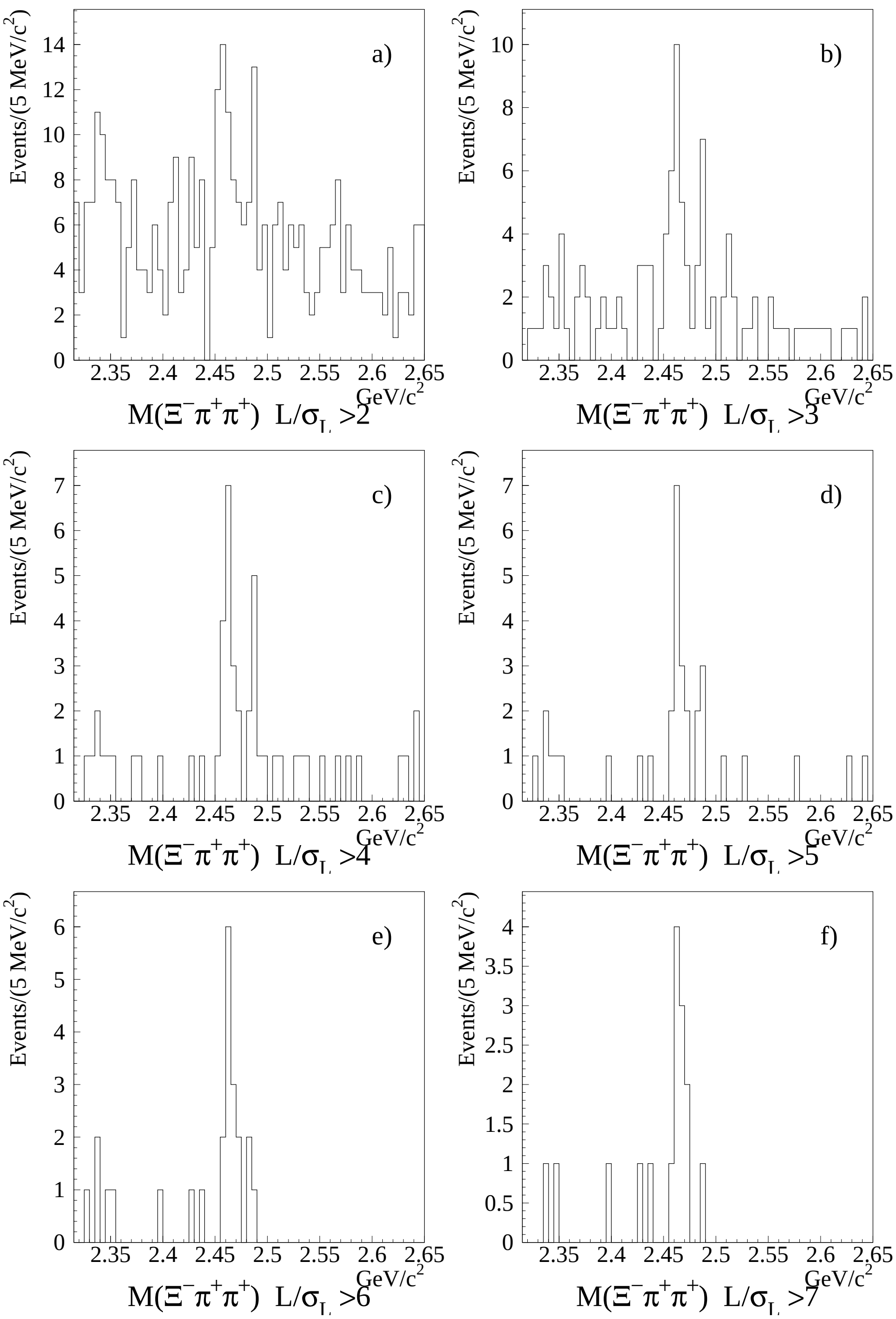

Figure 5.6: $\Xi^-\pi^+\pi^+$ invariant mass distributions using Multivee Ξ^- for L/σ_L from 2 to 7.

greater than -1050 cm (in the reference frame where the origin is at the center of M2).

- The z component of the momentum is limited to the range 35-100 GeV/c^2.
- Reject if a Ξ^- Type2 topology or MV topology is reconstructed to avoid duplication.

Because the Ξ^- is partially reconstructed we are not able to apply the Ξ^- invariant mass cuts as in previous reconstruction topologies, so to reduce the background contamination we require **ISO2**$< 0.01\%$ and $\sigma_t > 60$ fs in addition to the regular cuts **CLS**$> 2\%$ and particle identification. In Figure 5.7 we show the invariant mass distribution for a range of L/σ_L cuts.

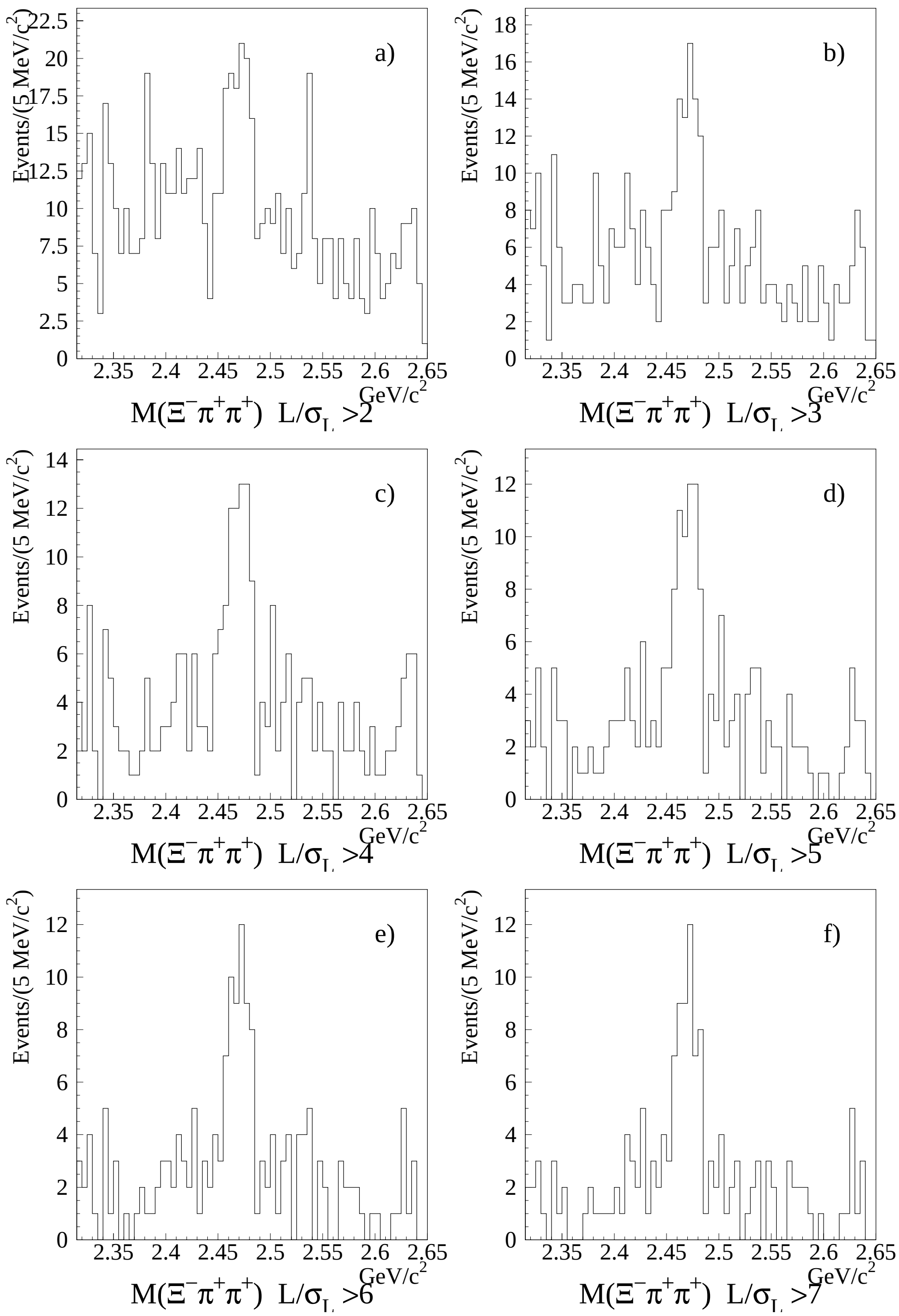

Figure 5.7: $\Xi^-\pi^+\pi^+$ invariant mass distributions using Kinks Ξ^- for L/σ_L from 2 to 7.

5.4 $\Xi_c^+ \to \Sigma^+ K^- \pi^+$ selection criteria

The following mode has been reconstructed using two decay modes for Σ^+ ($\Sigma^+ \to n\pi^+$ and $\Sigma^+ \to p\pi^0$). Both Σ^+ decay modes are reconstructed partially using the kink algorithm (Section 4.6). Kaons are identified requiring $\Delta W_K > 2$ and pions with the pion consistency $\Delta W_\pi >$ -6. We also use **CLS**> 2% and a $\sigma_t < 0.07$ ps. The selection of Σ^+ is described below and is optimized for this decay mode.

5.4.1 $\Xi_c^+ \to \Sigma^+(n\pi^+) K^- \pi^+$

Because pions are the most abundant hadron in the spectrometer, $\Sigma^+ \to n\pi^+$ is expected to have a contamination from random combinations of SSD Σ^+ tracks and MWPC tracks. There is an ambiguity in the Σ^+ momentum determination due to a twofold momentum ambiguity about 20% of the time. We also compared the ratio between π^+ momentum and Σ^+ momentum in data and Monte Carlo (MC) for single solutions. From this comparison we found the data shows a background which peaks at very low P_{π^+}/P_{Σ^+} and also at high P_{π^+}/P_{Σ^+}. To reduce this background we cut the P_{π^+}/P_{Σ^+} distribution to be limited to the range $0.06 < P_{\pi^+}/P_{\Sigma^+} < 0.33$. In Figure 5.8 we show the distributions in MC and Data and the effect of the cut in the invariant mass.

The ambiguity is treated as will be explained for $\Sigma^+ \to p\pi^0$ in next subsection. In Figure 5.9 is shown the invariant mass distribution for a range of L/σ_L cuts.

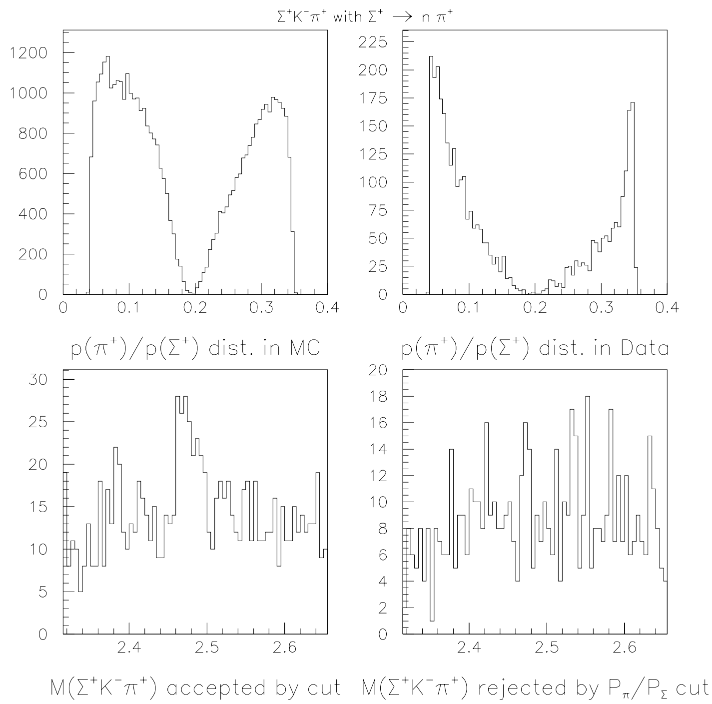

Figure 5.8: The p(π^+)/p(Σ^+) cut. In the top left plot is the MC distribution for p(π^+)/p(Σ^+). The top right is p(π^+)/p(Σ^+) distribution for data. The bottom plots show the effect of the cut $0.06 < P_{\pi^+}/P_{\Sigma^+} < 0.33$ in the invariant mass of the $\Sigma^+ K^- \pi^+$; on the left the events passing the cut and on the right the events rejected by the cut.

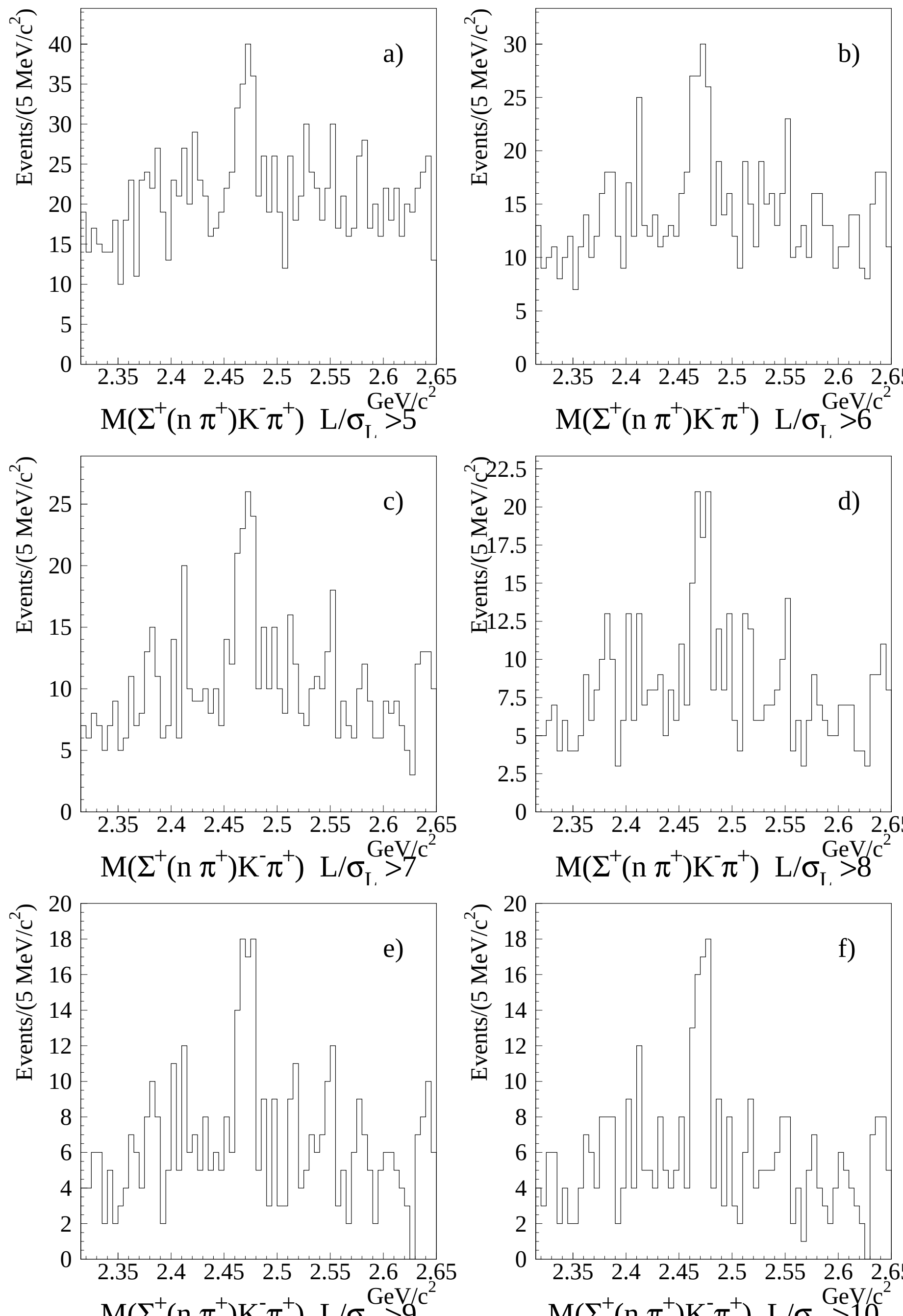

Figure 5.9: $\Sigma^+(n\ \pi^+)K^-\pi^+$ invariant mass distributions varying L/σ_L from 5 to 10.

5.4.2 $\Xi_c^+ \to \Sigma^+(p\pi^0)K^-\pi^+$

For this mode the reconstruction of the Σ^+ is expected to be clean because the proton from the Σ^+ decay can be cleanly identified by a Čerenkov cut of $\Delta W_p > 4$. In this mode the Σ^+ momentum ambiguity is about 80% (i.e. 80% double solution). This ambiguity produces a reflection of one solution into the other as shown in Figure 5.10 (from Monte Carlo) which leads to a contamination of the sidebands. To eliminate this contamination, we reject a solution candidate if the other $\Xi_c^+ \to \Sigma^+K^-\pi^+$ mass formed with the opposite solution is within $2.5\sigma_m$ of the nominal Ξ_c^+ mass. We refer this technique as a 'veto.' In Figure 5.11 we veto around the nominal mass of the first solution and we see that the projection of the second solution in the bottom plot has been cleaned up. Similarly, we use the same process when plotting the first solution while vetoing around the nominal mass of the second solution. The method guarantees that we count the real signal only once, but when the two solutions are close in mass may be lose an event because each is vetoed by the opposite solution. Those events are recovered by applying the veto method, only when the difference in the masses calculated using each solution is greater than 30 MeV/c^2 ($\Delta m > 30$ MeV/c^2). When the masses calculated using each solution is less than 30 MeV/c^2 ($\Delta m < 30$ MeV/c^2), then we select the higher momentum solution of Σ^+. In the latter case the invariant mass is free from reflection contamination in the sidebands from any of the solutions as shown in Figure 5.12. In Figure 5.13 is shown the invariant mass for a range of L/σ_L cuts.

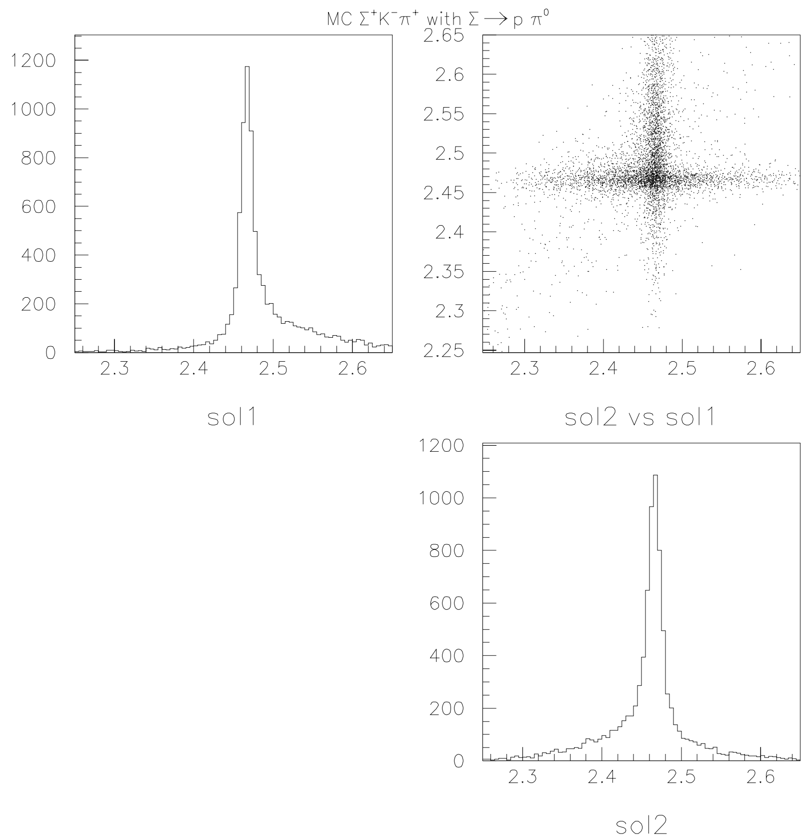

Figure 5.10: $\Sigma^+ K^- \pi^+$ invariant mass reconstruction Monte Carlo Scatter plot. The upper right is the scatter plot of solution 1 versus solution2. Also presented are the two projected mass plots. Note in the projections the contamination in the sidebands.

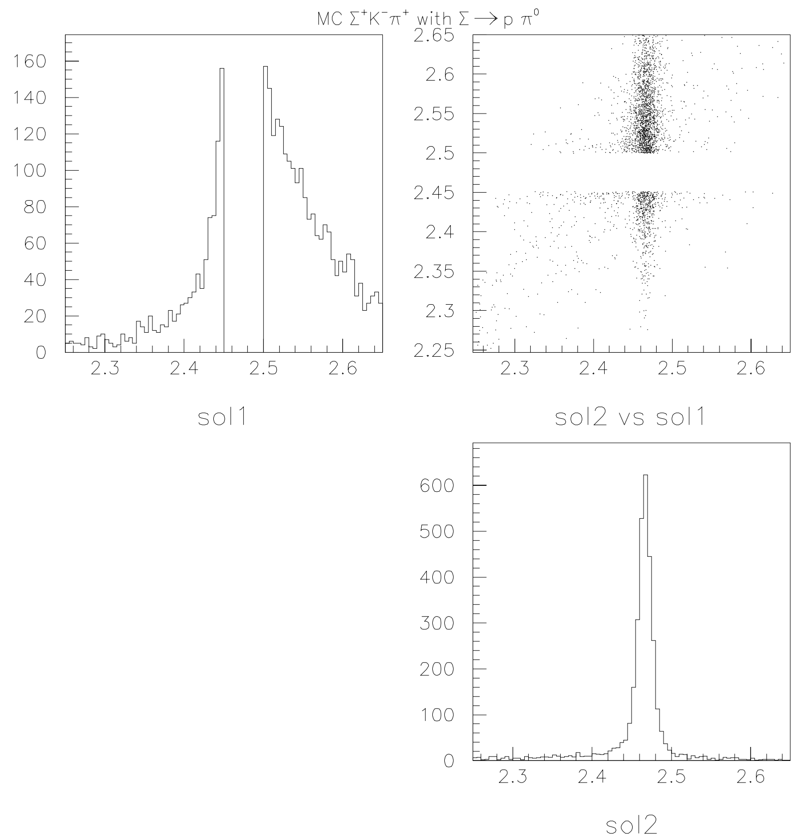

Figure 5.11: $\Sigma^+K^-\pi^+$ invariant mass reconstruction Monte Carlo Scatter plot with the applied veto in one solution. Note in the bottom plot the effect of the veto in the invariant mass of the opposite solution. The veto removes signal contamination in the sidebands from the reflection of the vetoed solution.

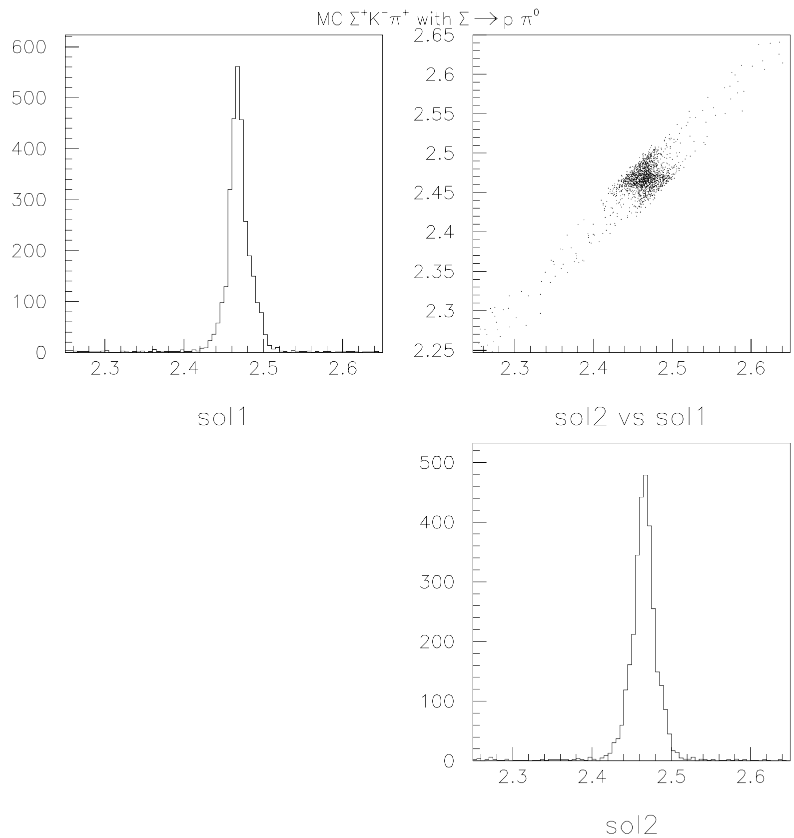

Figure 5.12: $\Sigma^+K^-\pi^+$ invariant mass reconstruction Monte Carlo scatter plot and mass projections with $\Delta m < 30$ MeV$/c^2$. Note in the top left and bottom plot the effect of $\Delta m < 30$ MeV$/c^2$ causes signal free of reflection contamination in sidebands in both solutions.

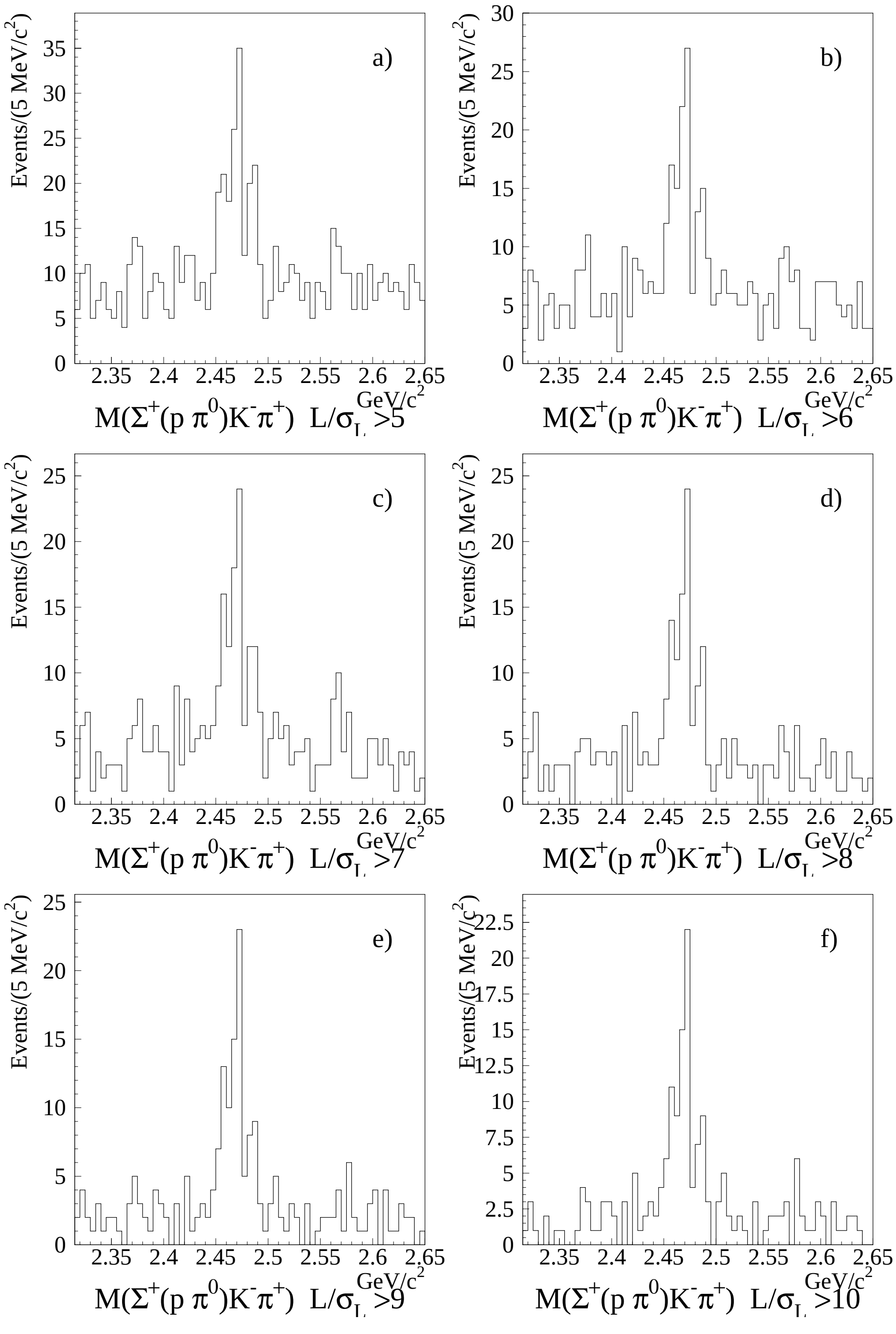

Figure 5.13: $\Sigma^+(p\ \pi^0)K^-\pi^+$ invariant mass distributions varying L/σ_L from 5 to 10.

5.5 $\Xi_c^+ \to pK^-\pi^+$ selection criteria

This mode is a Cabbibo suppressed decay which is reconstructed using three linked tracks with strong cuts in particle identification. We identify protons by requiring a significant separation with pions $\Delta W_p > 10$. We also require proton hypothesis is favored over the kaon hypothesis by two units of likelihood i.e. $W_K - W_p > 2$. For the kaon candidate, in addition to the usual requirement ($\Delta W_K > 2$), we demand $W_p - W_K > 0$. For the pion candidate we require $\Delta W_\pi >$ -6 and the momentum to be greater than 5 GeV/c. The secondary vertex must have a **CLS** > 15% and the signal is optimized requiring **ISO2** < 0.01% and $\sigma_t < 0.08$ ps. To reduce combinatorial background, the Ξ_c^+ candidate momentum is required to be less than 120 GeV/c. Long lifetime backgrounds from charmed mesons, where one particle is misidentified, are removed by making an invariant mass cut. Thus we eliminate contamination from the decays $D^+ \to K^-\pi^+\pi^+$, $D^+(D_s^+) \to K^-K^+\pi^+$ and $D^0 \to K^-K^+$. In Figure 5.14 is shown the invariant mass distributions for a range of L/σ_L cuts.

5.6 $\Xi_c^+ \to \Lambda^0 K^-\pi^+\pi^+$ selection criteria

In this mode we select Λ^0 candidates which decay downstream of the SSD detector (M1 vees). To reduce contamination from $K_s^0 \to \pi^+\pi^-$ decays, we require $\Delta W_p > 8$ for the proton in the Λ^0 decay. The particle identification cuts imposed are the default values $\Delta W_K > 2$ and $\Delta W_\pi >$ -6 for kaon and pion candidates respectively. The signal decay is optimized by requiring **CLS** > 15%, **ISO2** < 0.01%, and $\sigma_t < 0.10$ ps. In Figure 5.15 we present the invariant mass distribution for a range of L/σ_L cuts.

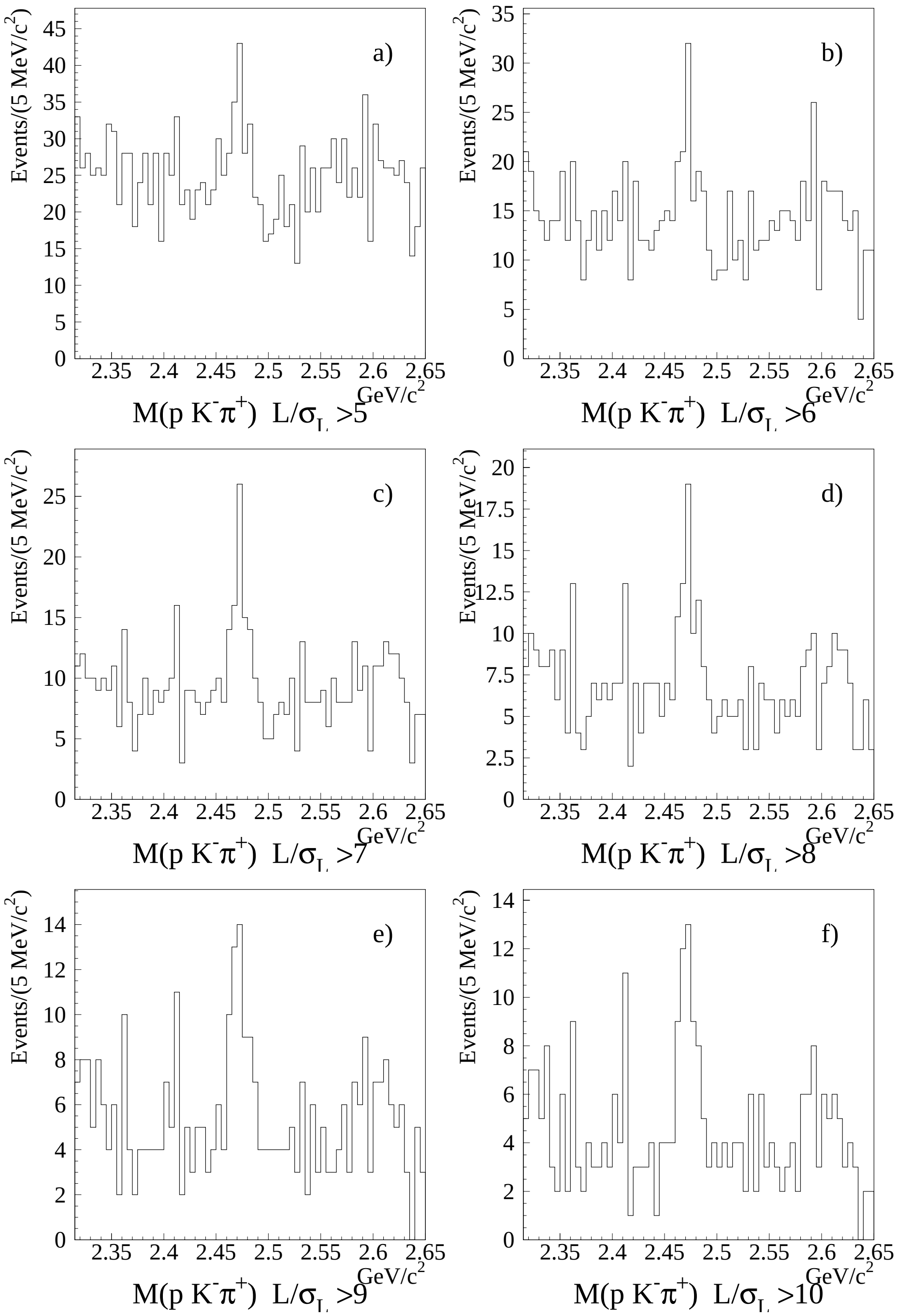

Figure 5.14: $pK^-\pi^+$ invariant mass distributions varying L/σ_L from 5 to 10.

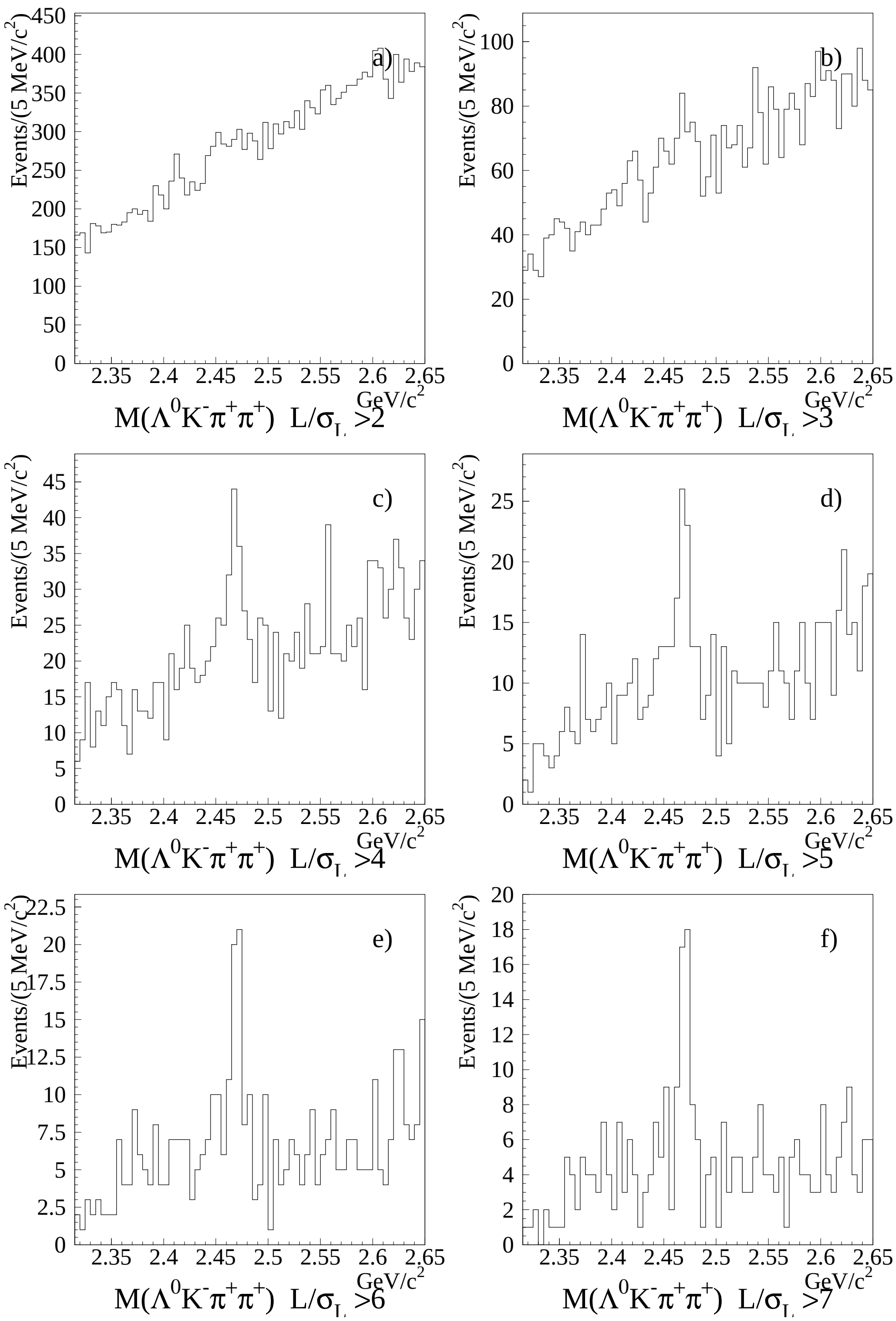

Figure 5.15: $\Lambda^0 K^- \pi^+ \pi^+$ invariant mass distributions varying L/σ_L from 2 to 7.

Chapter 6

Measurement of Ξ_c^+ lifetime

The good separation of the primary and secondary vertices makes it possible to measure the lifetime of charmed particles. The decay flight time, in the center of mass frame of the decaying particle, is related to the flight distance, L, by:

$$t = \frac{L}{c\beta\gamma}, \tag{6.1}$$

where c is the speed of light, γ is the Lorentz boost factor, and β is the velocity of the decaying particle in units of the speed of light. In practice $c\beta\gamma$ is measured using the relation $c\beta\gamma = p/m$, where p is the particle's momentum and m is its mass. The variable t is the *proper* time of the decay. The proper time of decaying particles has a exponential distribution of the form $e^{-t/\tau}$, where τ is the lifetime of the particle.

6.1 Lifetime technique

The technique used measure the Ξ_c^+ lifetime is a binned maximum likelihood fit [46]. We fit the reduced proper time (t') distribution, defined as

$$t' = \frac{L - N\sigma_L}{\gamma\beta c}, \tag{6.2}$$

where N is the vertex detachment cut. If the time resolution is independent of the reduced proper time, then t' is also an exponential distribution. The average σ_t as a function of the reduced proper time used according to Monte Carlo expectations for the $\Xi_c^+ \to \Xi^-\pi^+\pi^+$ decay is shown in Figure 6.1 a). The average σ_t expected is about 50 fs and the distribution is shown in Figure 6.1 b).

The lifetime technique begins by using the data of a given reconstructed topology to

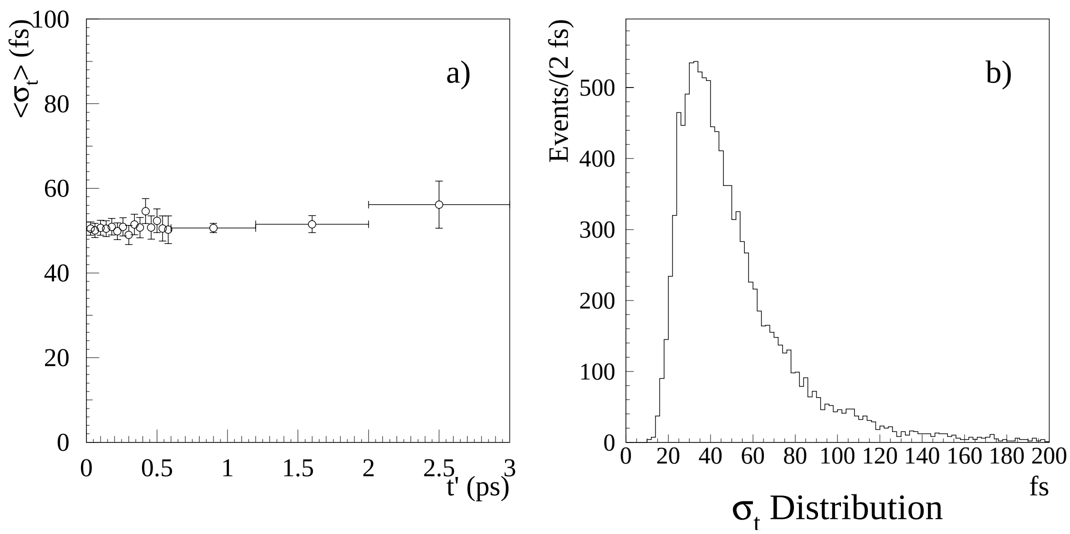

Figure 6.1: Expected properties for σ_t in the $\Xi_c^+ \to \Xi^-\pi^+\pi^+$ decay from Monte Carlo events. a)$< \sigma_t >$ vs t' shows no dependence of σ_t with the reduced proper time. b) σ_t distribution expected is about 50 fs average.

fill two histograms of reduced proper time, one from the signal region and one from the sidebands of the invariant mass. In this analysis we have four modes in eight reconstructed topologies, which gives a total of 16 histograms for t' (8 from signals and 8 from backgrounds). The events in the signal region of an invariant mass plot of charm candidates are formed by true events, i.e. from real Ξ_c^+, and background events in the signal region. Therefore, the histograms formed using events in the signal region contain a mixture of true signal and background. The sideband histograms contain only background events. The signal histograms contain events with invariant mass within two standard deviations of the nominal mass of the Ξ_c^+, and the background histograms contain events from invariant mass sidebands far enough from the signal; in this case we use events with invariant mass from 4 to 12 standard deviations away from the signal. The standard deviation of the signal (or mass resolution) is about 8 MeV/c^2 for the $\Xi_c^+ \to \Lambda^0 K^-\pi^+\pi^+$ decay channel and 10 MeV/c^2 for all other channels. For the background, the method assumes the same lifetime behavior in the signal region and in the sidebands, then the proper time distribution of true signal events is expected to be exponential and the expected proper time distribution of background events in the signal region is taken by the background histogram without a need of parameterization. A sketch of the process is shown in Figure 6.2

Also we need to take into account that the true exponential distribution of the reconstructed signal may suffer distortions induced due to triggering, geometrical acceptance, absorption, detector efficiencies, and analysis cuts like L/σ_L and **ISO2**. All of these effects are expressed in terms of the correction function $f(t')$. The correction function $f(t')$ is determined using a detailed Monte Carlo simulation of the experiment where the reduced proper time histogram of the Monte Carlo signal is

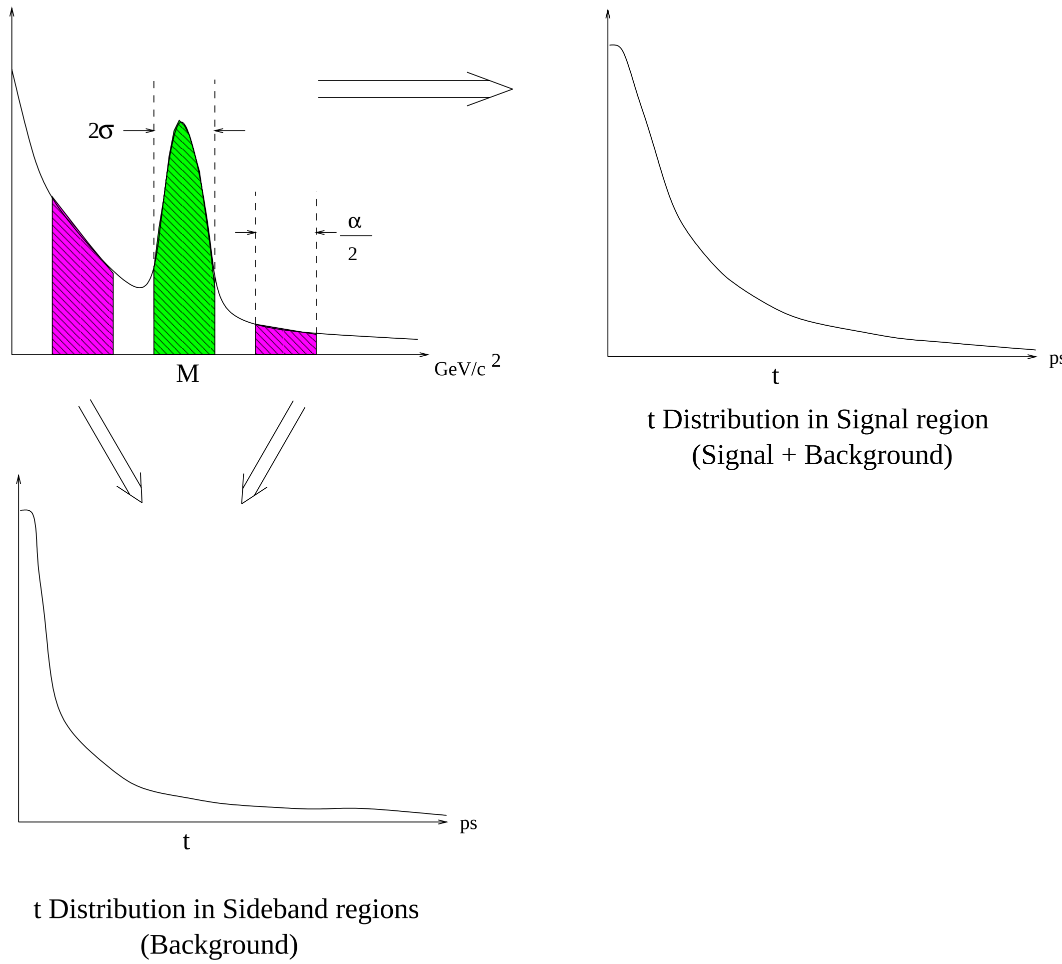

Figure 6.2: Sketch to demostrate how we fill the histograms used in the lifetime technique.

reconstructed applying the same analysis cuts. The correction function, $f(t')$, is obtained by dividing the Monte Carlo reduced proper time distribution by the Monte Carlo generated lifetime. The correction function used for each decay mode is shown in Figure 6.3.

With these considerations the predicted number of events in a reduced proper time bin is given by:

$$n_i = S\frac{f(t'_i)e^{-t'_i/\tau}}{\sum\limits_i f(t'_i)e^{-t'_i/\tau}} + B\frac{b_i}{\sum\limits_i b_i} \tag{6.3}$$

where S is the total number of signal events and B is the total number of background events in the signal region. The sum of S and B is the total number of events in the signal histograms and b_i describes the background reduced proper time evolution as estimated from sidebands. The likelihood used for a given reconstructed topology is

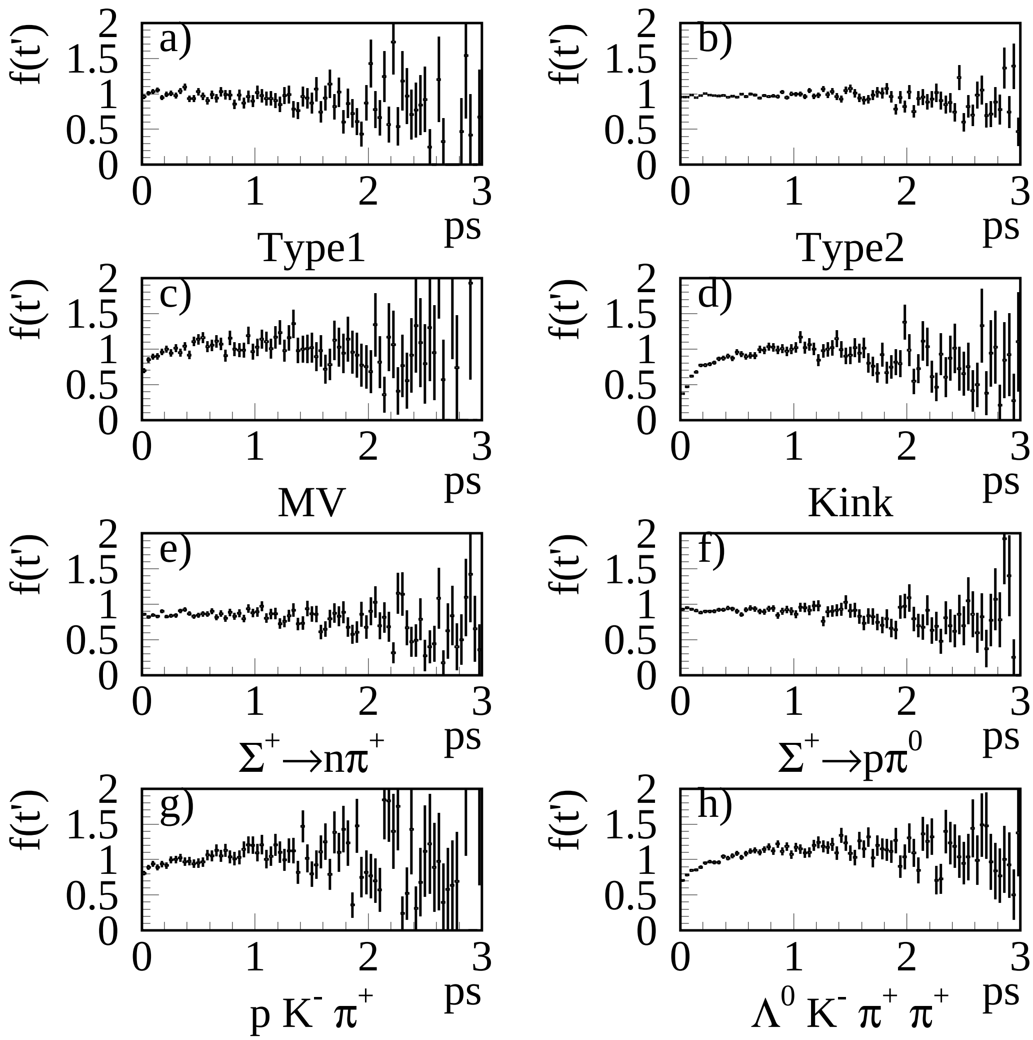

Figure 6.3: Lifetime correction functions for the different decay modes and topologies described earlier. a),b),c) and d) $\Xi_c^+ \to \Xi^-\pi^+\pi^+$ ($L/\sigma_L > 4$); e) and f) $\Xi_c^+ \to \Sigma^+K^-\pi^+$ ($L/\sigma_L > 7$); g) $\Xi_c^+ \to pK^-\pi^+$ ($L/\sigma_L > 7$); and h) $\Xi_c^+ \to \Lambda^0K^-\pi^+\pi^+$ ($L/\sigma_L > 4$).

given by

$$\mathcal{L} = (\prod_i \frac{n_i^{s_i} e^{-n_i}}{s_i!}) \times (\frac{(\alpha B)^{\sum\limits_i b_i} e^{-\alpha B}}{(\sum\limits_i b_i)!}) \tag{6.4}$$

where the first term is the product of the Poisson probabilities for each reduced proper time bin in the signal region where we observe s_i events when n_i are expected.

The second term is given by the Poisson probability of observing a total of $\sum b_i$ background events when α times B are expected while α accounts for the ratio of the total width of the sideband regions to the signal region. For this analysis we choose $\alpha = 4$ and the parameters of the fit are τ and B.

To combine all the topologies in a unique likelihood, we take the product of the independent likelihoods because each probability is independent of each other, and we require that the parameter τ is the same for all topologies because all are decay products of the same charm particle. For the background, this is different and we fix the total number of parameters in the fit to be nine, one for the lifetime τ and eight parameters for the backgrounds; one for each topology.

$$\begin{aligned} \mathcal{L}_{\Xi_c^+} = & \mathcal{L}^{\Xi^-\pi^+\pi^+}_{\mathrm{T}ype1} \times \mathcal{L}^{\Xi^-\pi^+\pi^+}_{\mathrm{T}ype2} \times \mathcal{L}^{\Xi^-\pi^+\pi^+}_{\mathrm{MV}} \times \mathcal{L}^{\Xi^-\pi^+\pi^+}_{\mathrm{K}ink} \\ & \times \mathcal{L}^{\Sigma^+K^-\pi^+}_{\Sigma^+(n\pi^+)} \times \mathcal{L}^{\Sigma^+K^-\pi^+}_{\Sigma^+(p\pi^0)} \times \mathcal{L}_{pK^-\pi^+} \times \mathcal{L}_{\Lambda^0K^-\pi^+\pi^+} \end{aligned} \tag{6.5}$$

The lifetime fit is accomplished using 75 reduced proper time bins for each topology which span the range from 0 to 3 picoseconds. The τ fit results are given in Figure 6.4 for a series of significance of detachment cuts. The lifetime computed using several L/σ_L cuts is stable and is consistent within the statistical uncertainties. At large L/σ_L cut, the measured lifetime is higher but consistent with L/σ_L cuts with higher statistical power.

Figure 6.5 shows the background subtracted, $f(t')$ corrected, reduced proper time distributions for first six L/σ_L cuts. The points represent the background subtracted, $f(t')$ corrected quantities, which are given by $(s_i - b_i/\alpha)/f(t'_i)$ and the vertical scale is arbitrary. The overlayed curve is a pure exponential $e^{-t/\tau}$ where τ is the fitted lifetime. All fits shows a good confidence level. In Figure 6.6 we show the corresponding invariant mass distribution for the combined sample. A clear signal is evident in all histograms.

For the quoted lifetime we select L/σ_L cut to be greater than 4 for the decay channels $\Xi_c^+ \to \Xi^-\pi^+\pi^+$ and $\Xi_c^+ \to \Lambda^0 K^-\pi^+\pi^+$ and L/σ_L greater than 7 for the decay channels $\Xi_c^+ \to \Sigma^+K^-\pi^+$ and $\Xi_c^+ \to pK^-\pi^+$. The criteria is a compromise of good statistical power of the signal is balanced with a reduced background. The signal yield from the invariant mass fit is 581.4 ± 31.9 events. The lifetime result from the likelihood method is:

$$\tau(\Xi_c^+) = 0.435 \pm 0.022 \text{ ps.} \tag{6.6}$$

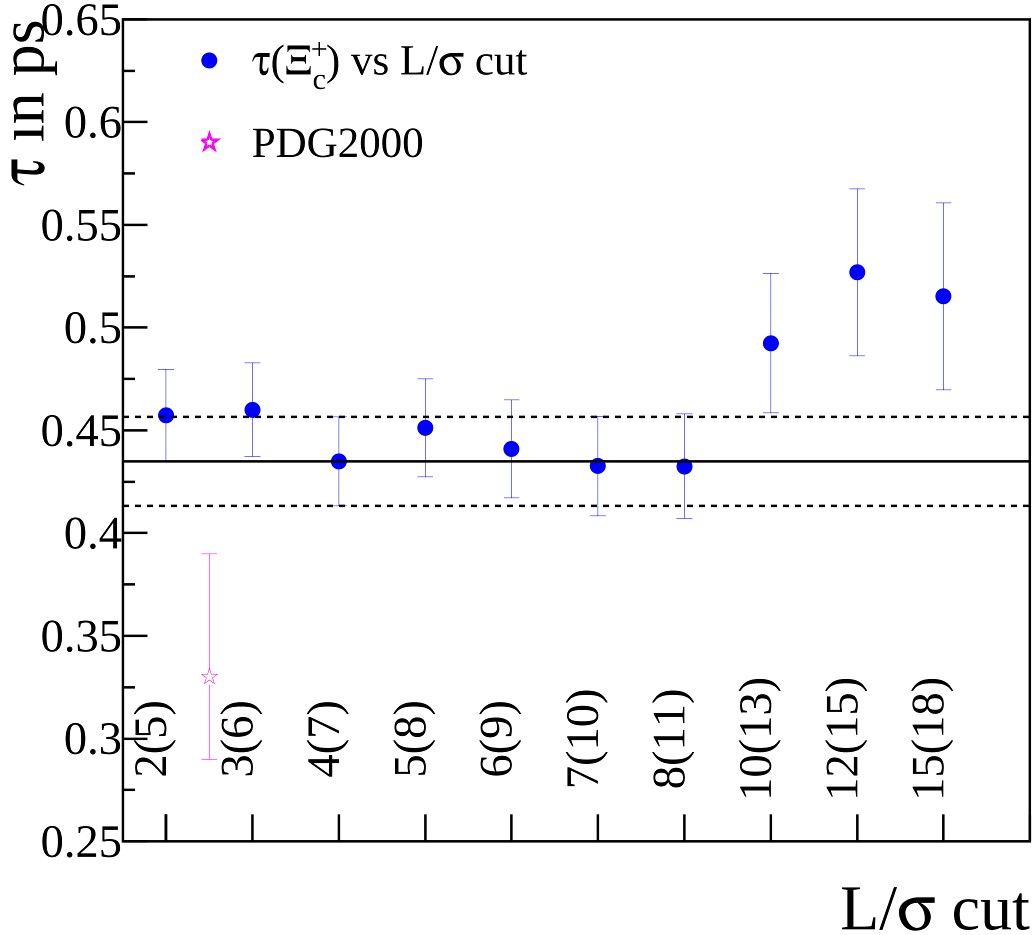

Figure 6.4: Lifetime measurements for a series of L/σ_L detachment cuts (numbers outside of parenthesis). Inside the parenthesis is the L/σ_L used for $\Sigma^+K^-\pi^+$ and $pK^-\pi^+$. The solid line represents the central value with the dotted lines showing the extent of the statistical uncertainty at $L/\sigma_L > 4(7)$.

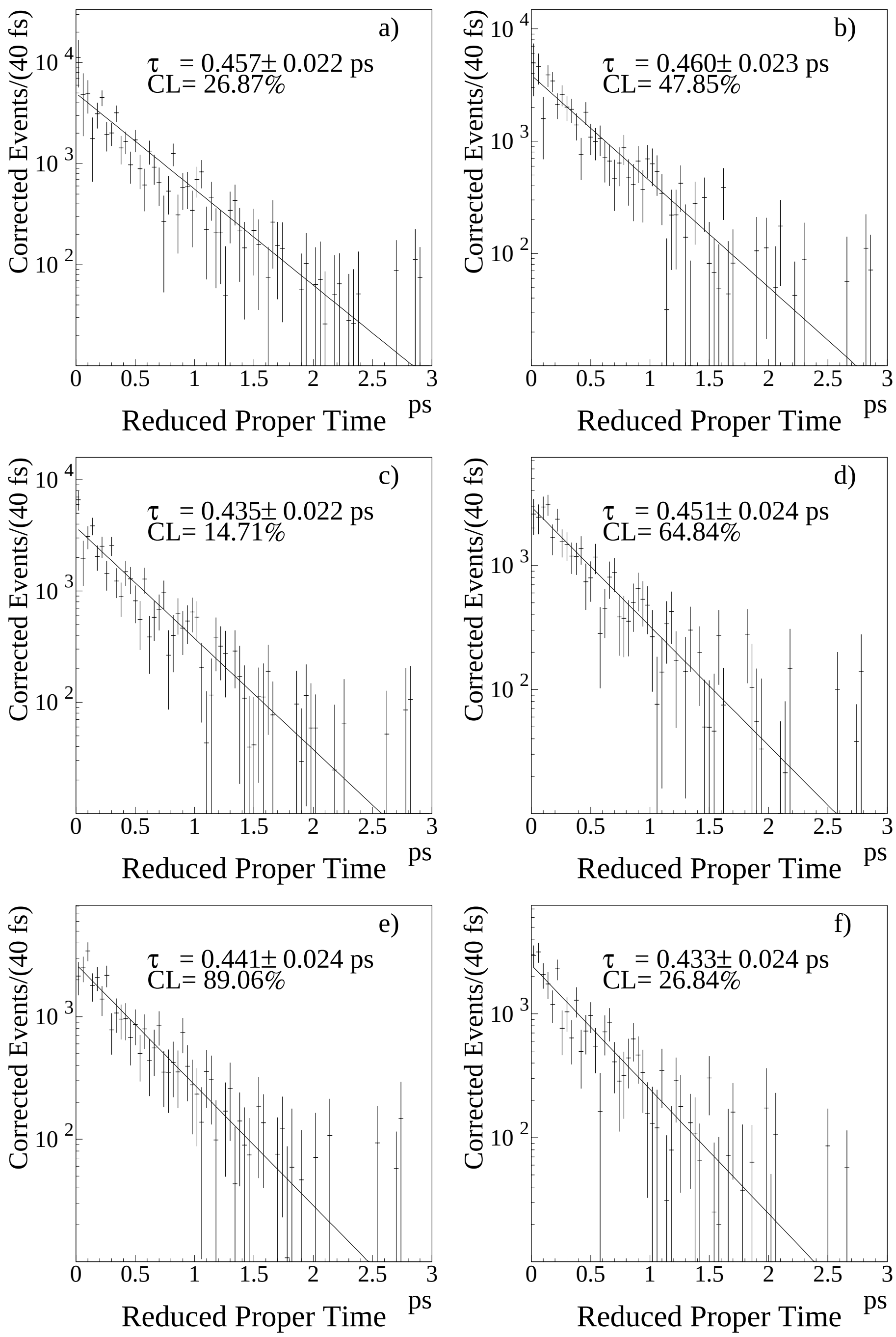

Figure 6.5: Background subtracted, Monte Carlo corrected t' distribution for L/σ_L cuts from 2(5) to 7(10) given in Figure 6.4.

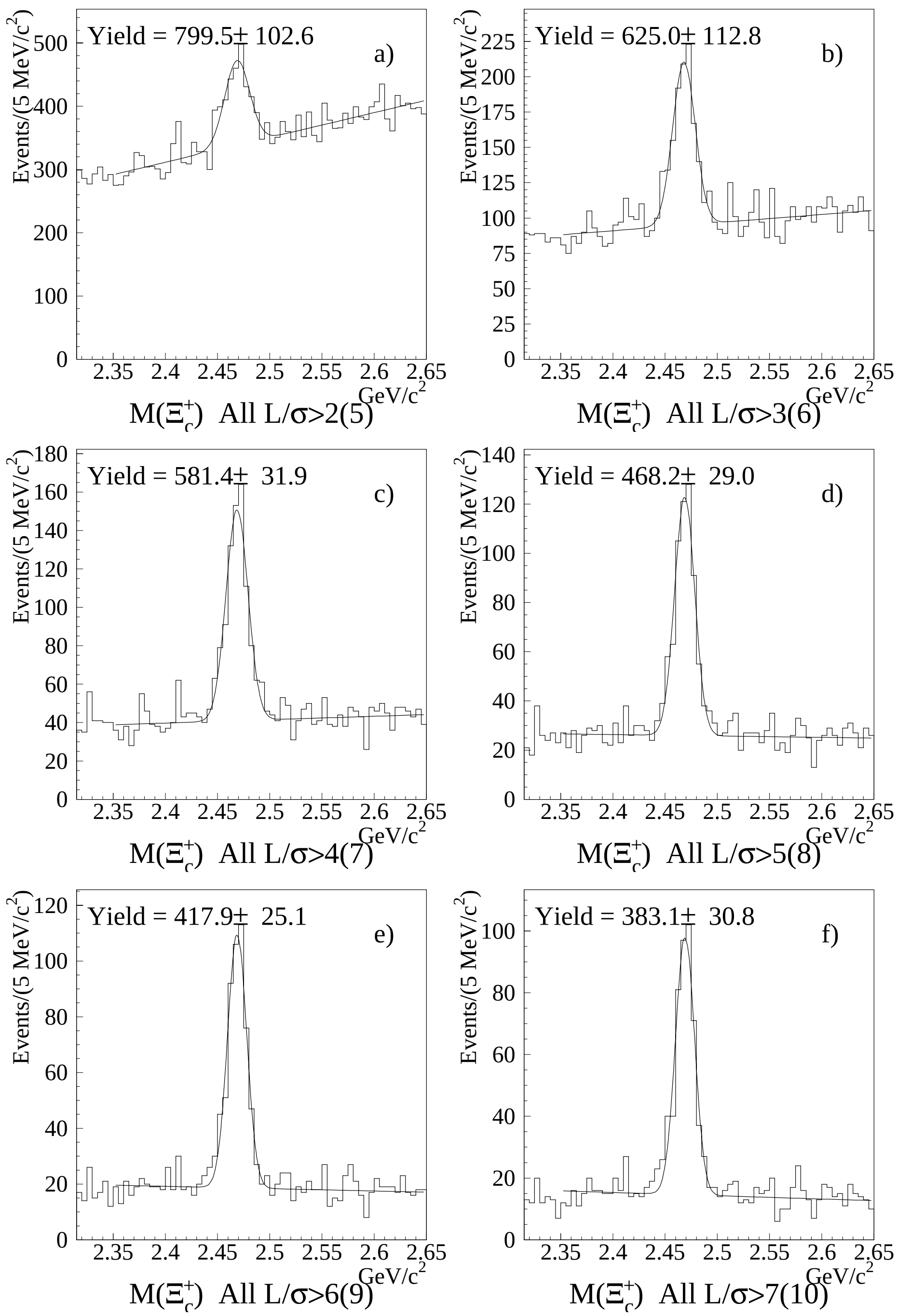

Figure 6.6: Invariant mass distributions for the combined sample for L/σ_L cuts from 2(5) to 7(10) given in Figure 6.4. (See Chapter 5 as some of the channels are much cleaner than the combined sample.)

6.2 Statistical uncertainty studies

To check the accuracy of the statistical uncertainty returned by the fit, we performed several checks.

First, we compared the quoted uncertainty with the asymmetrical values obtained by the change of the lifetime value which causes a decrease of one half in the log likelihood compared to the maximum. The reported value are -20.8 and $+22.4$ fs, in agreement with the quoted value.

A second test was a mini Monte Carlo analysis, in which we take each of the data histograms for signal and background and Poisson fluctuate each histogram bin around the original value. In this way an attempt is made to model the Poisson fluctuations of the background and the signal regions.

The new set of histograms, obtained through Poisson fluctuation, are used to measure the lifetime and its uncertainty, repeating this process five thousand times. The distribution of lifetime fits results of the mini Monte Carlo is close to a Gaussian distribution (expected because the asymmetric errors are close). The fit to a Gaussian distribution shown in Figure 6.7c) has a width of 23.2 fs. Similarly we did a Gaussian fit to the uncertainty distribution for the mini Monte Carlo fits as shown in Figure 6.7a) returning a mean of 21.5 fs.

For this study we can conclude that the binned maximum likelihood method successfully extracts the signal lifetime and the statistical uncertainty returned from the fit is correct.

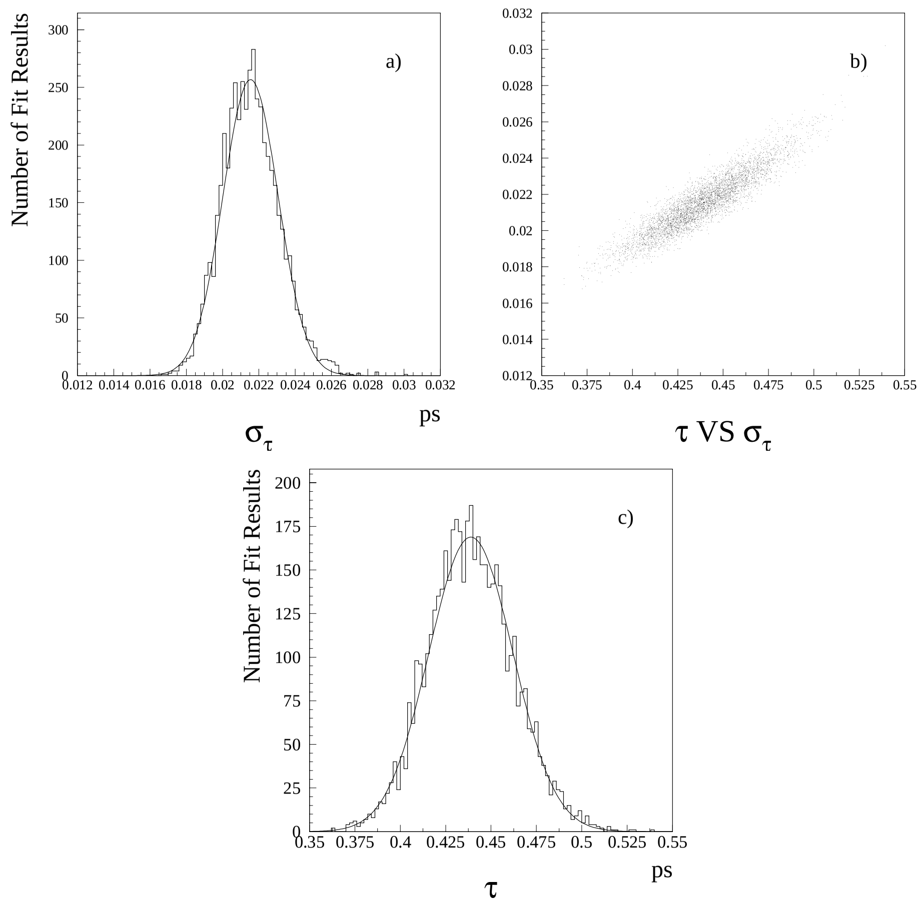

Figure 6.7: Lifetime and uncertainty fit results from 5000 fluctuation runs of the data histograms.

6.3 Systematic studies

We investigated several potential sources of systematic uncertainties which are discussed in separate sub-sections.

6.3.1 Split samples

Systematic effects were studied by computing the lifetime of data samples split by individual topologies and modes. The individual modes and topologies are independent data samples. A technique modeled after the *S-factor method* from the Particle Data Group [4] was used to separate true systematics variations from statistical fluctuations. The lifetime is evaluated for each of the statistically independent subsample and a *scaled variance* is calculated. In practice the scaled variance is given by:

$$\tilde{\sigma} = \sqrt{\frac{\langle x^2 \rangle - \langle x \rangle^2}{N-1}} \tag{6.7}$$

where $\langle x \rangle$ and $\langle x^2 \rangle$ are defined in terms of N independent subsample measurements $x_i \ \pm \sigma_i$ as:

$$\langle x \rangle \equiv \frac{\sum_{i=1}^{N} x_i/\sigma_i^2}{\sum_{i=1}^{N} 1/\sigma_i^2}, \qquad \langle x^2 \rangle \equiv \frac{\sum_{i=1}^{N} x_i^2/\sigma_i^2}{\sum_{i=1}^{N} 1/\sigma_i^2}. \tag{6.8}$$

The "split sample" variance is defined as the difference in quadrature between the reported statistical variance (statistical uncertainty of full sample) and the scaled variance, in case the scaled variance exceeds the statistical variance. The mathematical expresion is:

$$\sigma_{\text{split}} = \begin{cases} \sqrt{\tilde{\sigma}^2 - \sigma_{\text{stat}}^2} & \text{If } \tilde{\sigma} > \sigma_{\text{stat}}, \\ 0 & \text{If } \tilde{\sigma} < \sigma_{\text{stat}}. \end{cases} \tag{6.9}$$

The subsamples are taken for each reconstructed topology except for the cascade multivee (MV) which is taken together with downstream cascades (Type2) because of the small number of events (about 20) in $2\sigma_m$ mass (MV) window. Any possible systematics source for the MV subsample will be considered later. Figure 6.8 shows the result of the split sample systematic study. All variations are consistent within statistical uncertainties and there is no contribution to a systematic uncertainty.

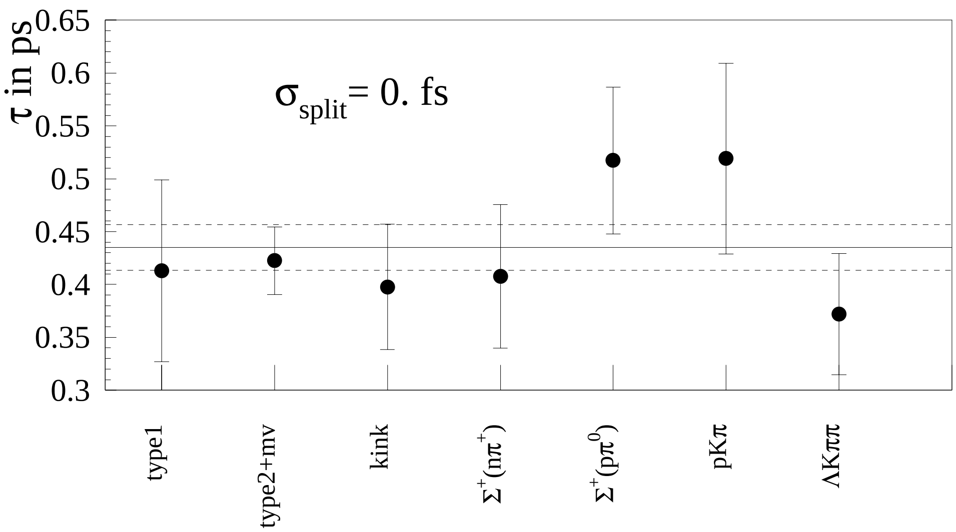

Figure 6.8: Split sample systematic study. The solid line represents the central value with the dotted lines showing the extent of the statistical uncertainty for the full sample.

6.3.2 Reduced Proper Time Resolution

We have investigated systematic effects due to the t' resolution by examining the variance in the fitted lifetime for different t' bin sizes (the bin size used were 30, 40 (default), 50, 60 and 70 fs), by reducing the fitting range from 3 to 2 ps, and by excluding the lowest t' bin from the fit. The systematic uncertainty due to t' resolution is estimated to be about 8 fs (7.5 fs).[1] Figure 6.9 shows the lifetime measurement for systematics studies on t' resolution.

6.3.3 Background Systematic

Systematic effects due to the background were investigated by varying the width of the sideband regions and by altering the background level by imposing a minimum separation between the primary and secondary vertices of 1.5 mm. The sideband regions used were two, three, and four (default) times the size of the signal region. The variance from these tests, added to the systematic uncertainty, is about 2 fs (2.3 fs). The first three points in Figure 6.10 show the lifetime measurement for systematics studies on background.

[1]The exclusion of the lowest t' bin from the fit did not have the proper normalization in the public result, in which we quote 4 fs.

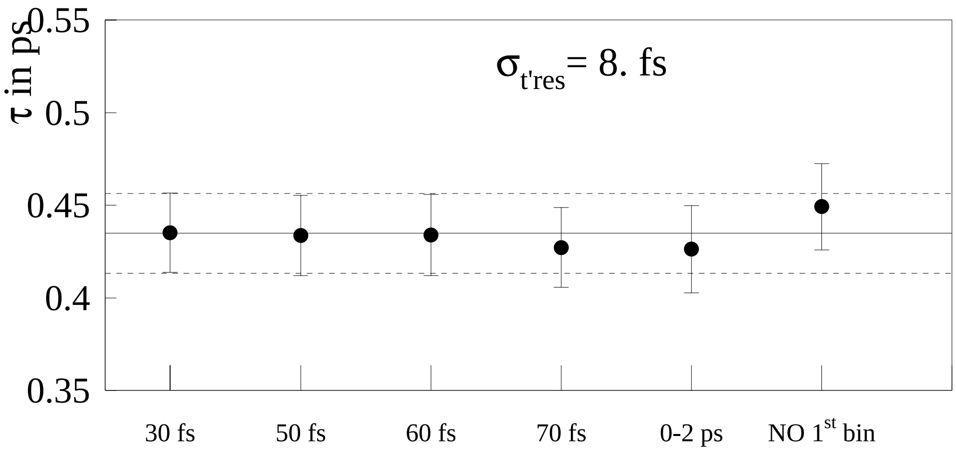

Figure 6.9: t' resolution systematic study. The solid line represents the central value for 40 fs bin size with the dotted lines showing the extent of the statistical uncertainty.

6.3.4 Fit variants

We tested different fit conditions; excluding MV type decays from the lifetime fit, taking the weighted average of the split samples, and using a combined fit of the mass shape and a reduced proper time of $\Xi_c^+ \to \Sigma^+ K^- \pi^+$ as an alternative method of treating the two solution ambiguity. The systematic due to the variation in fit conditions is taken to be the sample variance since we consider all of the measurements to be equally valid. The systematic uncertainty due to fit variants is estimated to be about 8 fs (7.6 fs). The last three points in Figure 6.10 show the lifetime measurements for systematic studies on fit variants.

6.3.5 Other Systematics

Other possible systematic contributions we checked were uncertainties in the measurement of particle momenta and the bias created by the treatment of the two solution ambiguity in the $\Sigma^+ K^- \pi^+$ mode.

The momentum magnitude of tracks has a small offset of about 1%, which is corrected for in the case of SSD linked tracks. For the case of an unlinked track as the Ξ^- or Σ^+ track this correction is more difficult to apply and can lead to a systematic shift in the reduced proper time. Our studies comparing corrected/uncorrected tracks show this shift to be 4 ± 2 fs. The final quoted value is adjusted by this amount and is a systematic uncertainty of 2 fs which we include in the final systematic uncertainty.

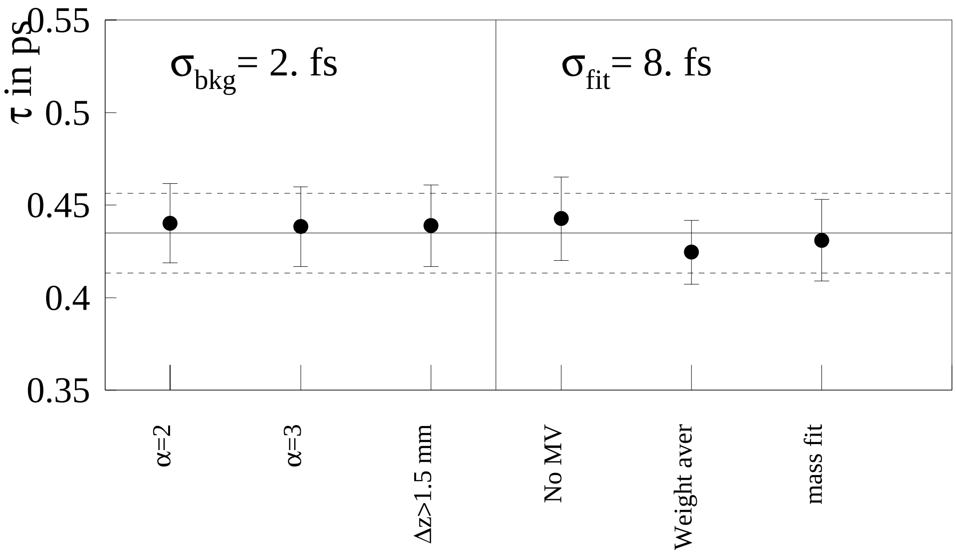

Figure 6.10: Background and fit variant systematic study. The solid line represents the central value for quoted value with the dotted lines showing the extent of the statistical uncertainty.

The treatment of the two solution ambiguity in the $\Sigma^+K^-\pi^+$ modes creates a small bump in a flat background distributions as illustrated in Figure 6.11. The combination of vetoing the opposite solution and the treatment of nearby solutions creates a false "signal" in the signal region proportional to the background level. This bump can create a small bias in the measured lifetime due to an overestimation in the signal yield. We studied this effect by varying the width of the diagonal (Δm cut), including removing the cut completely. This effect results in a shift of less than 1 fs on the total lifetime.

6.3.6 Final Result

The systematic uncertainty is summarized in Table 6.1.

Adding in quadrature all systematic contributions gives a total systematic uncertainty of 11 fs. We have measured the Ξ_c^+ lifetime using four decay modes which are reconstructed in eight different topologies with a combined sample of 532.4 ± 30.4 events.[2] We find the lifetime to be $0.439 \pm 0.022 \pm 0.011$ ps where the first error is statistical and the second is systematic.

[2]The quoted yield is from $\pm 2\sigma_m$ mass window used in the lifetime fit. The mass fit gives 581 events.

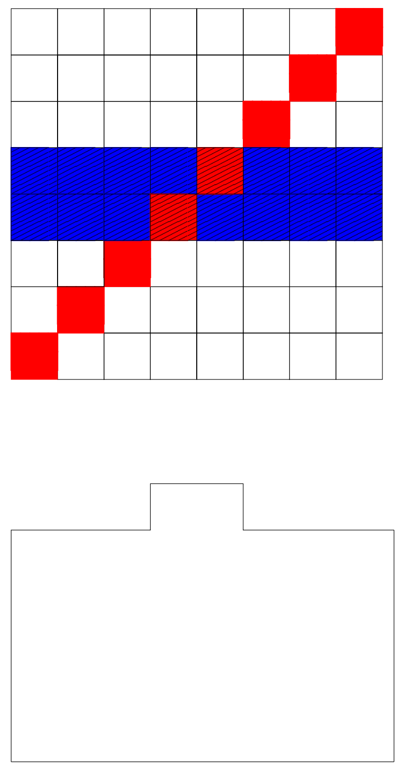

Figure 6.11: Sketch of background due to double solution treatment. The square pattern represents the scatter plot of the two mass solutions. The blue region (horizontal band) represents the excluded mass region from the opposite solution. The red region (diagonal band) represents the events where the two solutions are close and we treat them differently. The bottom plot is the projection of the white squares and represents the background distribution, after treat double solution events.

Table 6.1: Contributions to the systematic uncertainty.

Contribution	Uncertainty (fs)
Split sample	0
t' Resolution	$\pm 8(7.5)$
Background	$\pm 2(2.3)$
Fit variant	$\pm 8(7.6)$
Ξ_c^+ Momentum	± 2
two solution bias	± 1
Total	± 11

6.4 Preliminary measurement of the Ξ_c^0 lifetime

The Ξ_c^0 is the isospin partner of the Ξ_c^+. We present a preliminary lifetime measurement of the Ξ_c^0 using the Type2 Ξ^- only in the decay $\Xi_c^0 \to \Xi^-\pi^+$, since the reconstruction is similar to the $\Xi_c^+ \to \Xi^-\pi^+\pi^+$. Currently FOCUS is adding more decay modes and topologies before presenting a final result.

We use the same selection criteria as in Ξ_c^+ to select Type2 Ξ^- canditates, but excluding single link stub-stub vees. The Čerenkov identification on the pion of the Ξ_c^0 candidate daughter is tightened to $\Delta W_\pi > -1$. We impose a minimum momentum cut of 7 GeV/c, and a transverse momentum greater than 0.5 GeV/c on the pion. The secondary vertex must have a **CLS** $> 2\%$ and the signal is optimized by requiring $\sigma_t < 0.08$ ps. The Figure 6.12 displays the $f(t')$ correction function, invariant mass distribution, and t' distribution for $L/\sigma_L > 3$.

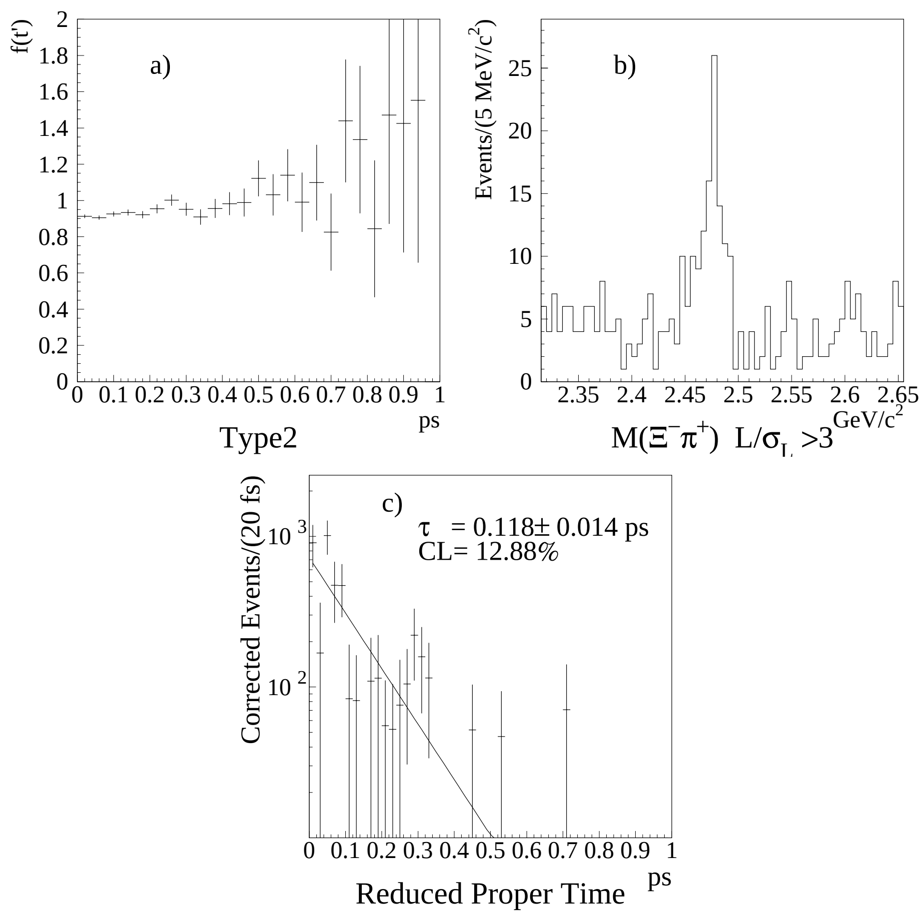

Figure 6.12: Lifetime correction function, invariant mass distribution, and Background subtracted, MC corrected t' distribution of $\Xi_c^0 \to \Xi^-\pi^+$. ($L/\sigma_L > 3$).

The preliminary measurement of the Ξ_c^0 lifetime uses a sample of 79 $\pm$ 11 events in a $\pm 2\sigma_m$ mass window. We find the lifetime to be 0.118 $\pm$ 0.014 ps. The lifetime value measured for the Ξ_c^0 is in agreement with the world average [4], but has better precision.

Chapter 7

Conclusion

In this chapter, the Ξ_c^+ lifetime is summarized and compared with measurements from other experiments.

7.1 Ξ_c^+ Lifetime measurements

There has been previous measurements of the Ξ_c^+ lifetime with the experimental uncertainty on the order of 20%. The measurement from this thesis has much smaller uncertainties than any previous measurement (about 5%). The comparison with other measurements is presented in Table 7.1 and Figure 7.1.

Table 7.1: Ξ_c^+ lifetime measurements

Experiment	Lifetime (ps)	Events	Year
WA62 [47]	$0.48^{+0.21+0.20}_{-0.15-0.15}$	53	1985
E400 [48]	$0.40^{+0.18}_{-0.12} \pm 0.10$	102	1987
ACCMOR (NA32) [49]	$0.20^{+0.11}_{-0.06}$	6	1989
E687 [50]	$0.41^{+0.11}_{-0.08} \pm 0.02$	30	1993
E687 [51]	$0.34^{+0.07}_{-0.05} \pm 0.02$	56	1998
PDG (average) [4]	$0.33^{+0.06}_{-0.04}$	–	2000
CLEO [52]	$0.503 \pm 0.047 \pm 0.018$	250	2001
This Measurement	$0.439 \pm 0.022 \pm 0.011$	532	2001

The experiments WA62, E400 and ACCMOR ran in the eighties. All three were fixed target experiments. The large uncertainties in those experiments are either due to poor vertex resolution (WA62 and E400) or low luminosity (ACCMOR). In the next decade (nineties) E687 measured the Ξ_c^+ lifetime with an improved detector compared to the previous decade. E687 first used only the decay mode $\Xi_c^+ \to \Xi^- \pi^+ \pi^+$, then added the decay mode $\Xi_c^+ \to \Sigma^+ K^- \pi^+$. The world average has been dominated by E687 result since 1998.

The value of FOCUS measurement in this thesis is larger than the current world average, but in agreement with previous measurements. Recently CLEO also reported a new measurement using the decay mode $\Xi_c^+ \to \Xi^- \pi^+ \pi^+$. The CLEO measurement is the first Ξ_c^+ lifetime in a e^+e^- environment.

7.2 Ξ_c^0 Lifetime measurements

There has been only a few measurements of the Ξ_c^0 lifetime. The comparison with other measurements is presented in Table 7.2 and Figure 7.1.

Table 7.2: Ξ_c^0 lifetime measurements

Experiment	Lifetime (ps)	Events	Year
ACCMOR (NA32) [53]	$0.082^{+0.059}_{-0.030}$	4	1990
E687 [54]	$0.101^{+0.025}_{-0.017} \pm 0.005$	42	1993
PDG (average) [4]	$0.098^{+0.023}_{-0.015}$	–	2000
This Preliminary Measurement	0.118 ± 0.014	79	2001

This measurement agrees with the current world average, but it has an improved uncertainty. FOCUS expects to improve this measurement as it did with the Ξ_c^+ lifetime, by adding more decay modes. In Figure 7.1 we present a comparison of experimental results for the Ξ_c^+ and Ξ_c^0 lifetime measurements. The new world averages are now determined by the FOCUS results.

7.3 Comparison of Result with Theory

As discussed in the introduction, the experimental lifetime hierarchy of charmed baryons is qualitatively in agreement with theory. A number of authors [55–58] predict that $\tau(\Xi_c^+)/\tau(\Lambda_c^+) >\sim 1.3$. Using the recent FOCUS result for Λ_c^+ lifetime [59] of $0.2046 \pm 0.0034 \pm 0.0025$ ps, a ratio of $\tau(\Xi_c^+)/\tau(\Lambda_c^+) = 2.15 \pm 0.13$ is obtained. Our well measured ratio is significantly different from predictions of order 1.3 and is supported with recent CLEO result of $\tau(\Xi_c^+)/\tau(\Lambda_c^+)_{CLEO} = 2.8 \pm 0.3$. On the other hand the ratio $\tau(\Xi_c^0)/\tau(\Lambda_c^+)$ agrees well between theory and experiment.

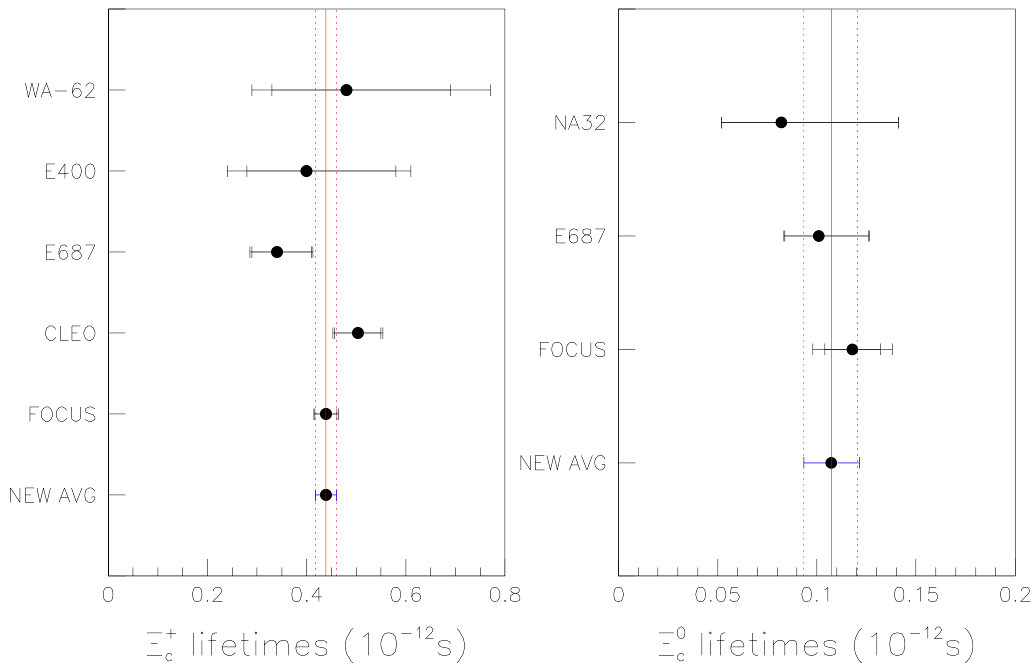

Figure 7.1: Comparison of lifetime measurements for Ξ_c^+ and Ξ_c^0. We excluded the ACCMOR measurement of the Ξ_c^+ lifetime, as well as, the first E687 measurement which is included in the latter E687 result. For the Ξ_c^0 we include an estimated systematic uncertainty of the same order as the statistical error.

With the lifetimes results we computed the ratio $\tau(\Xi_c^+)/\tau(\Xi_c^0)$ to be 3.72 ± 0.66 which agrees with the ratio estimated by CLEO [60] using semi-leptonic decays of $2.46 \pm 0.70^{+0.33}_{-0.23}$. A new measurement of the semi-leptonic decay rates needs to be made.

The precision of this measurement is a challenge for theoretical calculations using HQE. This measurement puts into question if HQE can correctly describe the lifetime of singly charmed baryons as the charmed baryon decays are far away from the asymptotic limit.[1] On the other hand, the measurement of the relative branching ratio of the Cabibbo suppressed decay $\Xi_c^+ \to pK^-\pi^+$ relative to Cabibbo favored decay $\Xi_c^+ \to \Xi^-\pi^+\pi^+$ [61]

$$\frac{B(\Xi_c^+ \to pK^-\pi^+)}{B(\Xi_c^+ \to \Xi^-\pi^+\pi^+)} = 0.234 \pm 0.047 \pm 0.022 \simeq \frac{\Gamma_{NL}^{spc} + \Gamma_{WS} - \Gamma_{NL}^{-}}{\Gamma_{NL}^{spc} + \Gamma_{NL}^{+} - \Gamma_{NL}^{-}} \tan{\theta_c}^2 \qquad (7.1)$$

[1]The asymptotic limit is when $m_C \to \infty$ and the lifetime of all hadrons composed by m_C are the same.

together with the lifetime results may indicate that the contribution of W Scattering (Γ_{WS}) is bigger than previously expected.

Together with the lifetimes predictions, HQE has theoretical predictions for the branching ratios for semi-leptonic decays of baryons. Two additional experimental measurements are warranted.

- A measurement of inclusive semi-leptonic decays would test the HQE predictions and provide information for the expected value of the operators that affect the singly charmed baryons. Bigi [62] has proposed to measure these values using the large data sample that BELLE and BABAR are going to collect (about 500 $fb^{-}1$ by 2005).

- A measurement of Cabibbo Favored and Cabibbo suppressed semi-leptonic decays of Ξ_c, like

$$\frac{B(\Xi_c^+ \to \Lambda^0 e^+ \nu_e)}{B(\Xi_c^+ \to \Xi^0 e^+ \nu_e)} \quad \text{or} \quad \frac{B(\Xi_c^0 \to \Sigma^- e^+ \nu_e)}{B(\Xi_c^0 \to \Xi^- e^+ \nu_e)}, \tag{7.2}$$

  would test s quark interference ($\tilde{\Gamma}_{SL}$) predictions in semi-leptonic decays.

Finally, Guberina [63] recently discussed a new approach in which a model independent analysis can be used to perform a ratio of lifetimes. His lifetime ratios are expressed as a function of several Cabibbo suppressed branching ratios.

It is valuable to determine the contributions to the lifetimes of the singly charmed baryons. If we can correctly predict the lifetimes of singly charmed baryons, then we may have confidence that we can calculate the lifetimes of the doubly and triply charmed baryons. The measurements reported in my thesis will serve as critical comparison for future theoretical calculations.

Bibliography

[1] M. Gell-Mann, Phys. Lett. **8**, 214 (1964).

[2] G. Zweig, *An SU_3 model for strong interaction symmetry and its breaking II* (1964), cERN-TH-412 (unpublished, later published in [3]).

[3] D. B. Lichtenberg and S. P. Rosen, eds., *Developments in the Quark Theory of Hadrons, Vol. 1. 1964–1978* (Hadronic Press, Inc., Nonantum, MA, 1980).

[4] D. E. Groom et al. (Particle Data Group), Eur. Phys. J. **C15**, 1 (2000).

[5] Y. Fukuda et al. (Super-Kamiokande), Phys. Rev. Lett. **81**, 1562 (1998), `hep-ex/9807003`.

[6] C. Caso et al., Eur. Phys. J. **C3**, 1 (1998).

[7] N. Cabibbo, Phys. Rev. Lett. **10**, 531 (1963).

[8] J. D. Bjorken and S. L. Glashow, Phys. Lett. **11**, 255 (1964).

[9] J. J. Aubert et al., Phys. Rev. Lett. **33**, 1404 (1974).

[10] J. E. Augustin et al., Phys. Rev. Lett. **33**, 1406 (1974).

[11] G. Goldhaber et al., Phys. Rev. Lett. **37**, 255 (1976).

[12] I. Peruzzi et al., Phys. Rev. Lett. **37**, 569 (1976).

[13] B. Knapp et al., Phys. Rev. Lett. **37**, 882 (1976).

[14] K. Niu, E. Mikumo, and Y. Maeda, Prog. Theor. Phys. **46**, 1644 (1971).

[15] K. Hoshino et al., Prog. Theor. Phys. **53**, 1859 (1975).

[16] S. W. Herb et al., Phys. Rev. Lett. **39**, 252 (1977).

[17] F. Abe et al. (CDF), Phys. Rev. **D50**, 2966 (1994).

[18] J. P. Alexander et al. (CLEO), Phys. Rev. Lett. **83**, 3390 (1999), `hep-ex/9906013`.

[19] R. Ammar et al. (CLEO), Phys. Rev. Lett. **86**, 1167 (2001), hep-ex/0007041.

[20] J. M. Link et al. (FOCUS) (2002a), hep-ex/0203037.

[21] B. Guberina, S. Nussinov, R. D. Peccei, and R. Ruckl, Phys. Lett. **B89**, 111 (1979).

[22] B. Guberina, R. Ruckl, and J. Trampetic, Z. Phys. **C33**, 297 (1986).

[23] G. Bellini, I. I. Y. Bigi, and P. J. Dornan, Phys. Rept. **289**, 1 (1997).

[24] B. Guberina and B. Melic, Eur. Phys. J. **C2**, 697 (1998a), hep-ph/9704445.

[25] L. M. Jones and H. W. Wyld, Phys. Rev. **D17**, 759 (1978).

[26] G. Alimonti et al., Nucl. Instrum. Meth. **A314**, 411 (1992).

[27] P. L. Frabetti et al. (E-687), Nucl. Instrum. Meth. **A320**, 519 (1992).

[28] FOCUS Collaboration, *Description and performance of the fermilab focus spectrometer* (1999), http://www-focus.fnal.gov/nim/focus-nim/nim.ps, In preparation for publication in *Nucl. Instrum. Meth.*

[29] P. L. Frabetti et al., Phys. Lett. **B407**, 79 (1997).

[30] J. Wilson and M. Purohit, *E831 at South Carolina (DOE review)*, http://scuch8.psc.sc.edu/hep/doe_rev.ps.

[31] G. Bellini et al., Nucl. Instrum. Meth. **A252**, 366 (1986).

[32] J. D. Jackson, *Classical Electrodynamics* (John Wiley & Sons, Inc., New York, 1975), 2nd ed.

[33] S. Bianco et al., *The upgraded outer EM calorimeter of FOCUS at Fermilab* (1999), hep-ex/9912066, to appear in the proceedings of *VIII International Conference on Calorimetry in HEP.*

[34] L. Cinquini, J. Cumalat, E. Erdos, B. O'Reilly, and E. Vaandering, *A description of the Inner Electromagnetic Calorimeter for FOCUS*, FOCUS memo, http://www-hep.colorado.edu/~e687/focus_doc/iecal.ps.

[35] G. Bonomi, in *Calorimetry in high energy physics. Proceedings, 7th International Conference, Tucson, USA, November 9-14, 1997*, edited by E. Cheu, T. Embry, J. Rutherfoord, and R. Wigmans (Singapore, Singapore: World Scientific, 1998), pp. 276–280.

[36] G. Boca et al., Nucl. Instrum. Meth. **A409**, 561 (1998).

[37] P. Liguori, P. Sheldon, P. Vitulo, M. Webster, and J. Wilson, *OM design and considerations* (1994), FOCUS memo, http://www-focus.fnal.gov/papers/outermu_1.ps.

[38] J. Wiss, A. Rahimi, and F. Cogswell, *Mounting the MH1 and MH2 arrays* (1996), FOCUS memo, `http://www-focus.fnal.gov/papers/mh_support.ps,http://www-focus.fnal.gov/papers/mh_sketch.ps`.

[39] A. Kreymer and F. Prelz, *DAQ architecture for E831* (1997), FOCUS memo, `http://www-focus.fnal.gov/papers/daq_main/daq_main/daq_main.html`.

[40] J. M. Link et al. (FOCUS) (2001a), `hep-ex/0108011`.

[41] J. Wiss, *Thoughts on muon identification algorithms for E831* (1994), FOCUS memo, `http://web.hep.uiuc.edu/e687/muon/mu_id_thoughts.ps`.

[42] C. Cawlfield, M. Ruesnink, and J. Wiss, *Muon identification χ^2 confidence levels* (1994), FOCUS memo, `http://web.hep.uiuc.edu/e687/muon/chisq.ps`.

[43] J. E. Ramírez-Vargas, Master's thesis, Universidad de Puerto Rico, Recinto Universitario de Mayagüez (1997).

[44] M. G. Hosack, *Confidence level for outer muons (2nd ed.)* (1998), FOCUS memo, `http://www-focus.fnal.gov/papers/omu_conf2.ps`.

[45] R. L. Culbertson, Ph.D. thesis, University of Illinois at Urbana-Champaign (1993).

[46] P. L. Frabetti et al. (E-687), Phys. Lett. **B263**, 584 (1991).

[47] S. F. Biagi et al., Phys. Lett. **B150**, 230 (1985).

[48] P. Coteus et al., Phys. Rev. Lett. **59**, 1530 (1987).

[49] S. Barlag et al. (ACCMOR), Phys. Lett. **B233**, 522 (1989).

[50] P. L. Frabetti et al. (Fermilab E687), Phys. Rev. Lett. **70**, 1381 (1993a).

[51] P. L. Frabetti et al. (The E687), Phys. Lett. **B427**, 211 (1998).

[52] A. H. Mahmood et al. (CLEO), Phys. Rev. **D65**, 031102 (2002), `hep-ex/0110058`.

[53] S. Barlag et al. (ACCMOR), Phys. Lett. **B236**, 495 (1990).

[54] P. L. Frabetti et al. (E687), Phys. Rev. Lett. **70**, 2058 (1993b).

[55] B. Guberina and B. Melic, Eur. Phys. J. **C2**, 697 (1998b), `hep-ph/9704445`.

[56] I. I. Y. Bigi (1996), talk given at Workshop on Heavy Quarks at Fixed Target (HQ 96), St. Goar, Germany, 3-6 Oct 1996 (UND-HEP-96-BIG06), `hep-ph/9612293`.

[57] B. Blok and M. A. Shifman (1991), talk given at 3rd Workshop on the Tau-Charm Factory, Marbella, Spain, 1-6 Jun 1993 (TPI-MINN-93-55-T, UMN-TH-1227-93, TECHNION-PH-93-41), `hep-ph/9311331`.

[58] H.-Y. Cheng, Phys. Rev. **D56**, 2783 (1997), hep-ph/9704260.

[59] J. M. Link et al. (FOCUS), Phys. Rev. Lett. **88**, 161801 (2002b), hep-ex/0202001.

[60] J. P. Alexander et al. (CLEO), Phys. Rev. Lett. **74**, 3113 (1995).

[61] J. M. Link et al. (FOCUS), Phys. Lett. **B512**, 277 (2001b), hep-ex/0102040.

[62] I. I. Bigi (2001), hep-ph/0111182.

[63] B. Guberina and H. Stefancic (2002), hep-ph/0202080.